Order Number 9401727

Characterization of advanced etching reactors using novel diagnostic tools

Patel, Vipulkumar K., Ph.D.

New Jersey Institute of Technology, 1993

U·M·I
300 N. Zeeb Rd.
Ann Arbor, MI 48106

CHARACTERIZATION OF ADVANCED ETCHING REACTORS USING NOVEL DIAGNOSTIC TOOLS

by
Vipulkumar Patel

A Dissertation
Submitted to the Faculty of
New Jersey Institute of Technology
in Partial Fulfillment of the Requirements for the Degree of
Doctor of Philosophy

Department of Electrical and Computer Engineering
May 1993

ABSTRACT

Characterization of Advanced Etching Reactors Using Novel Diagnostic Tools

By

Vipulkumar Patel

Plasma etching equipment used for sub-micron integrated circuit fabrication at present are exclusively based on 13.56 MHz, capacitively coupled, parallel-plate geometry. The underlying mechanisms of plasma processes in these reactors are not well understood and there is even less understanding of how the etch-tool parameters relate to the plasma discharge characteristics which actually determine the etch process. In this thesis, new diagnostic techniques were applied for the characterization and optimization of plasma etching processes in various reactor configurations.

Specifically, diode and triode configurations were studied extensively using tuned scanning Langmuir probes. Both radial and axial distributions of plasma density were measured for a range of process parameters. Extensive mapping of plasma region in these reactors have shown that the plasma density distribution is dramatically different for dissociative molecular etching gases as compared to inert gases. Furthermore, the density distribution was found to be strongly dependent on the electronegativity of the process gas. In the triode configuration, the relative phase between the RF voltage waveforms applied to the electrodes was found to determine both the magnitude and distribution of the plasma density. Typically, higher etch-rates and better etch-uniformity were obtained for out-of-phase excitation(180°) as compared with the in-phase excitation(0°) in the triode.

The understanding gained by these studies has lead to the development of a novel magnetic multipole based triode reactor configuration. This new reactor

configuration can be operated at low pressures and produces high-rate, low damage etching of submicron features with required profile control.

In addition, a new plasma etching diagnostic technique based on thermal imaging of wafer was developed. The technique has been found to be useful for *in situ* real-time monitoring of end-point and uniformity of etching as well as for inferring wafer temperature and heat transfer characteristics. Also, a simple end-point detection technique based on plasma impedance monitoring was developed which eliminates the need for optical access to the wafer/plasma.

APPROVAL PAGE

Characterization of Advanced Etching Reactors
Using Novel Diagnostic Tools

Vipulkumar Patel

Dr. Walter F. Kosonocky, Thesis Advisor (Date)
Distinguished Professor of Electrical Engineering and Holder of
Foundation Chair in Optoelectronics and Solid-State Circuits, NJIT

Dr. Bawa Singh, Committee Member (Date)
Member of Technical Staff, David Sarnoff Research Center

Dr. Durgamadhab Misra, Committee Member (Date)
Assistant Professor of Electrical Engineering, NJIT

Dr. Constantine Manikopoulos, Committee Member (Date)
Associate Professor of Electrical and Computer Engineering, NJIT

Dr. Nuggehalli Ravindra, Committee Member (Date)
Associate Professor of Physics, NJIT

Dr. Robert Marcus, Committee Member (Date)
Research Professor of Physics and Chemistry, NJIT

BIOGRAPHICAL SKETCH

Author: Vipulkumar Patel

Degree: Doctor of Philosophy in Electrical Engineering

Date: May 1993

Undergraduate and Graduate Education:

- Master of Science in Electrical Engineering
  New Jersey Institute of Technology, Newark, NJ, 1990

- Bachelor of Engineering in Electronics Engineering
  M. S. University, Baroda, India, 1987

Presentations:

V. Patel, M. Kaplinsky, W. F. Kosonocky, S. Ayyagari and B. Singh, "Heat Transfer Analysis of Silicon Wafers During Reactive Ion Etching," *39th American Vacuum Society National Symposium* , Chicago, IL(November-1992).

V. Patel, W. F. Kosonocky, B. Singh, H. C. Sun and N. McCaffrey, "End Point Monitoring of Patterned Wafers During Reactive Ion Etching using a High Resolution Infrared Camera," *39th American Vacuum Society National Symposium,* Chicago, IL(November-1992).

B. Singh, V. Patel, H.C. Sun and J. H. Thomas,III, "The Effect of RF Phase on the Plasma Density and Distribution for Electronegative Gases in a Triode Etching Reactor," *39th American Vacuum Society National Symposium,* Chicago, IL(November-1992).

H. C. Sun, V. Patel, B. Singh, E. Whittaker and J. H. Thomas,III, "Plasma Etching Diagnostics for Low Pressure Tools using High Sensitivity Diode Absorption Spectroscopy," *39th American Vacuum Society National Symposium,* Chicago, IL(November-1992).

B. Singh, V. Patel, J. H. Thomas,III, and O. R. Mesker, "Low Temperature Diamond Deposition by Electron Assisted Hot-Filament Chemical Vapor Deposition," *39th American Vacuum Society National Symposium,* Chicago, IL(November-1992).

E. A. Whittaker, H.C. Sun, V. Patel and B. Singh, "High Sensitivity Absorption Spectroscopy for Low Pressure Plasma Etching Diagnostics," *45th Gaseous Electronics Conference*, Boston, MA (October-1992).

B. Singh, V. Patel, H.C. Sun, E. A. Whittaker, R. Kerns and J. Maher, "Hollow Anode based High Efficiency RF Triode Reactor," *45th Gaseous Electronics Conference*, Boston, MA (October-1992).

V. Patel, M. Patel, S. Ayyagari, D. Misra, W. F. Kosonocky, B. Singh, M. Leahy and O. Mesker, "Application of Thermal Imaging for Monitoring Wafer Temperature and End-point Detection in Plasma Etching," *TECHCON'90*, San Jose, CA (October-1992).

V. Patel, H. C. Sun, B. Singh and B. Brycki, "Spatial Mapping of Plasma Density Distribution in Parallel-Plate Diode and Triode Etching Reactors," To be presented at *40th American Vacuum Society National Symposium,* Orlando, FL(November-1993).

H. C. Sun, B. Singh, V. Patel, H. Lee, B. Brycki and E. A. Whittaker, "Measurements of Species Concentration and Plasma Characterization for Oxide Etching Chemistry in Inductively Coupled Plasma Reactors," To be presented at *40th American Vacuum Society National Symposium,* Orlando, FL(November-1993).

Publications:

V. Patel, M. Patel, S. Ayyagari, D. Misra, W.F. Kosonocky and B. Singh, "Wafer Temperature Measurements and End-point Detection During plasma Etching by Thermal Imaging," *Applied Physics Letters*, **59**(11), pp. 1299-1301(1991).

V. Patel, W.F. Kosonocky, S. Ayyagari, M. Patel and B. Singh, "Application of Thermal Imaging Methodology for Plasma Etching Diagnosis," *Proceedings of SPIE's Technical Symposium on Process Module Metrology, Control and Clustering*, **1594**, pp. 204-208 (1991).

B. Singh, J. H. Thomas,III and V. Patel, "Magnetic Multipole Based Reactive Ion Etching Reactor," *Applied Physics Letters*, **60**(19), pp. 2335-2337 (1992).

V. Patel, J. H. Thomas,III and B. Singh, "Reactive Ion Etching End-point Determination by Plasma Impedance Monitoring," *Applied Physics Letters*, **61**(16), pp. 1912-1914 (1992).

H. C. Sun, V. Patel, B. Singh, E. Whittaker and J. H. Thomas,III, "Measurements of Neutral Species in Low Pressure C_2F_6 Discharges using Diode Laser Absorption Spectroscopy," *Journal of Vacuum Science and Technology,* (July-August, 1993).

H. C. Sun, E. A. Whittaker, Y. W. Bae, C. K. Ng, V. Patel, W. H. Tam, S. McGuire, B. Singh and B. Gallois, "Combined Wavelength and Frequency Modulation Spectroscopy: A Novel Diagnostic Tool for Material Processing," *Applied Optics*, **32**(6), pp. 885-893 (1993).

B. Singh, V. Patel, H. C. Sun, R. Kerns and J. Maher, "Hollow Anode Discharge Based High Efficiency RF Triode Reactor, Part 1: Basic Phenomenon; Part II: Diagnostics," To be submitted to the *Journal of Electrochemical Society*.

V. Patel, H. C. Sun, B. Singh and B. Brycki, "Polysilicon Etching in Magnetic Multipole Enhanced Triode Reactor," To be submitted to the *Journal of Vacuum Science and Technology*.

V. Patel, H. C. Sun, B. Singh and B. Brycki, "A Parametric Study of Low Pressure Diode Reactor using Scanning Langmuir Probes," To be submitted to the *Journal of Vacuum Science and Technology*.

V. Patel, H. C. Sun, B. Singh and B. Brycki, "Effect of RF Phase on Discharge Characteristics in a Triode Reactor," To be submitted to the *Journal of Vacuum Science and Technology*.

This thesis is dedicated to my wife Swati.

ACKNOWLEDGMENT

First and foremost, thanks to my advisors, Prof. Walter F. Kosonocky and Dr. Bawa Singh, who treated me like a mature independent researcher from the day I started. They have deeply influenced the way I live and work and I strongly desire to continue working with them in the future, even if I may not live close to New Jersey.

Prof. Kosonocky has supported my research in a grand style during my tenure as his student and has given me a kind of freedom one can only dream of. His extensive experience and expertise in the area of infrared sensors and thermal imaging helped me getting started on the SEMATECH funded project on *in situ* monitoring of wafers using an infrared camera during plasma etching. The David Sarnoff Research Center hosted collaborative efforts between the NJIT, the Stevens Institute of Technology and the Rutgers University under the NJ SEMATECH Center of Excellence in Plasma Etching. During the course of developing new applications of thermal imaging for plasma etching, it was required to learn about various aspects of plasma etching technology. Dr. Bawa Singh at Sarnoff provided experimental facility and guidance for doing research on plasma etching. The experimental work on reactor characterization in this thesis would not have been possible without his vision of magnetic multipole enhanced triode reactor and his expertise in plasma physics. The hospitality he has extended to me in his laboratory at the David Sarnoff Research Center is unforgettable.

Sarnoff was a great place to work on a thesis. I found the staff at Sarnoff very cooperative and extremely knowledgeable. For years to come, I will benefit from my experience of working with them. I will specially like to acknowledge contributions from Dr. John Thomas,III and Bogdan Brycki. Before joining 3M research laboratory, John was always available for discussion whenever I needed him. Also, without Bogdan's novel ideas on design and construction of experimental apparatus, the work would not have been finished in three years.

Special thanks are due to my friend and constant collaborator Dr. Steve Sun of the Stevens Institute of Technology, who happily devoted months of his time for jointly performing difficult experimental tasks and end-less discussions.

I would like to thank many fellow inmates at NJIT for providing help in numerous aspects. I am pleased to specially acknowledge the contributions from Jitesh Shah and Prof. Durga Misra on experimental help, Ayyagari Subramanyam, Michael Kaplinsky and Helen Martinov for theoretical heat transfer analysis and Nathaniel McCaffrey on the camera electronics.

My wife, Swati, to whom this thesis is dedicated, provided continuous care, love and understanding. Also, constant encouragement from my sister, Kokila, brother-in-law, Thakor, and my parents have given me the strength to finish the dissertation.

TABLE OF CONTENTS

Chapter **Page**

1 MOTIVATION AND RESEARCH OBJECTIVES 1
1.1 Motivation 1
1.2 Objectives of the Research 5
1.3 Thesis Content 6
2 REVIEW OF PLASMA PHYSICS AND CHEMISTRY APPLICABLE TO ETCHING REACTORS 8
2.1 Basic Physical Phenomena Occurring in RF Discharges 8
2.1.1 Debye Shielding and Sheath Formation 11
2.1.2 Phenomena in RF Sheaths 12
2.1.3 Bohm Criterion for Existence of a Pre-sheath 14
2.1.4 Induced DC Bias 16
2.1.5 Ambipolar Diffusion and Effects of Negative Ions 20
2.2 Chemical Considerations for Plasma Etching 23
2.3 General Description of Parallel-Plate Etch Tools 26
2.4 Significance of Low Pressure Plasma Etching 27
3 CHARACTERIZATION OF CONVENTIONAL PARALLEL-PLATE TOOLS 30
3.1 Experimental Set-up 31
3.1.1 Scanning Tuned Langmuir Probe Diagnosis 33
3.2 Diode Configuration- Results and Discussion 36
3.2.1 Effect of Pressure on Axial Plasma Density Distribution 36
3.2.1.1 Ar Discharge 37
3.2.1.2 Oxygen Discharge 39
3.2.1.3 CHF_3 Discharge 41
3.2.1.4 SF_6 Discharge 43
3.2.2 Radial Distribution of Plasma Density 45

Chapter Page

3.3 Triode Configuration- Results and Discussion 47
3.3.1 Effect of Pressure on Axial Plasma Density Distribution in Ar and Oxygen 47
3.3.2 Effect of Phase on Induced Bias 49
3.3.3 Effect of Phase on Radial Plasma Density Distribution 50
3.3.4 Effect of Phase on Axial Plasma Density Distribution 53
3.3.5 Effect of Phase on Etch-rates 55
3.4 Summary 58
4 MAGNETIC MULTIPOLE ENHANCED TRIODE REACTOR 59
4.1 Need for Magnetic Enhancement 59
4.2 Existing Approaches for Magnetic Enhancement 61
4.3 New Magnetic Multipole Enhanced Triode Reactor 67
4.3.1 Experimental Set-up 68
4.3.2 Description of Magnetic Multipolar Bucket 69
4.4 Experimental Results for Multipole Enhanced Reactor 71
4.4.1 Comparison With Triode Configuration 71
4.4.2 Polysilicon Etching in Multipole Reactor 75
4.5 Summary 85
5 A NEW PLASMA ETCHING DIAGNOSTIC TOOL BASED ON THERMAL IMAGING OF WAFER 86
5.1 Basic Theory of Radiometric Measurements 87
5.2 Experimental Setup 89
5.3 End-point Detection and In Situ Monitoring of Uniformity of Etching 94
5.3.1 Emissivity Model for a Thin Film Multilayer Structure 95
5.3.2 End-point Detection of Polysilicon Etching 98
5.3.3 Effect of Back-side Polysilicon 106
5.3.4 End-point Detection on Patterned Wafers 106
5.3.5 *In Situ* Monitoring of Uniformity of Etching 110
5.3.6 End-point Detection for Silicide and Polyside Etching 112
5.3.7 Effect of Viewing Angle on End-point Detection 115

Chapter **Page**

5.4 Temperature Measurements 118
5.4.1 Introduction 118
5.4.2 Calibration Technique 120
5.4.3 Effect of Process Parameters on Wafer Temperature 122
5.4.4 Heat of Reaction 125
5.5 Heat Transfer Analysis 128
5.5.1 Theoretical Model 129
5.5.2 Experimental Results and Discussion 133
5.5.3 Gas-Back-Cooled Chuck 135
5.5.4 3-D Heat Transfer Analysis 137
5.6 Limitations for the Applicability of the Technique 141
5.7 Summary 141
6 CONCLUSIONS AND RECOMMENDATIONS 142
6.1 Conclusions 142
6.2 Suggested Work 143

APPENDICES

A LANGMUIR PROBE DIAGNOSTICS OF PLASMAS 144
A.1 Introduction 144
A.2 Basic Theory of Langmuir Probe: The Case of Cylindrical Probe 144
A.3 Langmuir Probe Measurements of RF Discharges 148
B PLASMA ETCHING END-POINT DETERMINATION BY PLASMA IMPEDANCE MONITORING 154
B.1 Introduction 154
B.2 Experimental Setup 155
B.3 Results and Discussion 157
B.4 Summary 160

REFERENCES 161

LIST OF FIGURES

Figure		Page
1	The sheath structure showing the ion density (n_i), the time-averaged electron density ($\overline{n_e}$) and the instantaneous electron density (n_e) at one time in an RF cycle	13
2	An electrical circuit model of RF glow discharges in a diode	18
3	Primary processes occurring in a plasma etch process	24
4	Calculated mean free path as a function of pressure for air	29
5	Schematic diagrams of (a) diode and (b) triode reactor configurations	31
6	Schematic diagram of the experimental set-up	32
7	Experimental arrangement for the practical implementation of the tuned Langmuir probe technique	34
8	Axial variation of saturated ion current for various pressures in (a) and pressure and power dependence of induced bias in (b) for Ar plasma	38
9	Axial variation of saturated ion current for various pressures in (a) and pressure and power dependence of induced bias in (b) for O_2 plasma	40
10	Axial variation of saturated ion current for various pressures in (a) and pressure and power dependence of induced bias in (b) for CHF_3 plasma	42
11	Axial variation of saturated ion current for various pressures in (a) and pressure and power dependence of induced bias in (b) for SF_6 plasma	44
12	Radial plasma density distribution for Ar, O_2 and SF_6 plasma at 100 mTorr	46
13	Axial plasma density distribution in a triode for Ar for various pressures (180° phase, 200W/electrode power)	48
14	Axial plasma density distribution for O_2 for various pressures (180° phase, 200W/electrode power)	48
15	Effect of varying phase between 0° to 320° on induced bias for O_2, CHF_3 and SF_6 discharges at 100 mTorr	49

Figure Page

16 Lower electrode bias dependence on phase for different power conditions for SF_6 at 30 mTorr 50

17 Radial plasma density distribution measured 1.0" above the bottom electrode for three phase conditions in O_2 plasma at 100 mTorr 51

18 Radial plasma density distribution measured 1.0" above the bottom electrode for three phase conditions in CHF_3 plasma at 100 mTorr 51

19 Radial plasma density distribution measured 1.0" above the bottom electrode for three phase conditions in SF_6 plasma at 100 mTorr 52

20 Axial plasma density profile for three phase conditions in O_2 plasma at 100 mTorr 53

21 Axial plasma density profile for three phase condition in SF_6 plasma at 100 mTorr 54

22 Etch-rates measured across the wafer for polysilicon etching in 100 mTorr SF_6 plasma 56

23 Oxide etch-rates as function of phase in CHF_3 plasma 57

24 Schematics of a planar magnetron etching system with static magnetic field 62

25 Schematic diagram of a commercial magnetically enhanced etching system with rotating magnetic field 63

26 Schematic of a commercial tri-electrode reactor with magnetic confinement 64

27 Schematics of supermagnetron plasma etcher 66

28 A schematic diagram of the test-stand consisting electrical block diagram of the power supplies and connection to each electrode 68

29 (a) Multipolar magnetic bucket (b) radial field characteristics of the multipole plasma confinement system 70

30 Saturated ion current and DC bias on the lower electrode as a function of argon pressure (a) triode configuration (b) multipole enhanced triode configuration 72

31 Plasma uniformity scans performed in argon using a Langmuir probe for the pressure ranges of (a)10-30 mTorr and (b)1-3 mTorr 74

Figure **Page**

32 The induced bias variation as a function of upper and lower power (0-400W) in Cl_2 plasma at 100 mTorr in (a) and 1 mTorr in (b)..... 76

33 Geometric representation of an experimental design based FCC model with center point replication..... 78

34 RS-1 results for Cl_2 etching of polysilicon; upper and lower power dependence on lower and upper power..... 79

35 RS-1 results for Cl_2 etching of polysilicon; pressure and lower power dependence of polysilicon etch-rate and selectivity 80

36 RS-1 results for Cl_2 etching of polysilicon; pressure and upper power dependence of etch-rate and selectivity..... 82

37 RS-1 results for Cl_2 etching of polysilicon; power and upper power dependence of etch-rate and selectivity..... 83

38 SEM photograph of an etched profile for 15 mTorr, 55W lower power and 1.3 KW upper power condition..... 84

39 SEM photograph of an etched profile for 30 mTorr, 100W lower power and 1.3 KW upper power condition..... 84

40 Radiation thermometry with lens..... 88

41 Experimental set-up for *in situ* wafer monitoring during plasma etching by infrared camera for the cases of (a) normal imaging of wafer in an open-ended diode reactor and (b) oblique imaging in a production-type parallel-plate diode/triode reactor 90

42 Measured spectral responsivity and quantum efficiency of the PtSi SBD array..... 91

43 Product of the PtSi detector spectral responsivity and spectral radiant exitance from a blackbody source for different temperatures 92

44 Measured response of eight pixels selected across the detector array under uniform imager illumination condition 93

45 The apparent reflectivity and transmittivity of a semitransparent slab..... 98

46 Calculated reflectance, transmittance and emittance at 4.1 μm as a function of thickness of the material being etched in (b) for the multilayer structure as shown in (a)..... 100

Figure Page

47 Calculated reflectance, transmittance and emittance at 4.1 μm as a function of thickness of the material being etched in (b) for the multilayer structure as shown in (a) 101

48 Comparison of experimental data on end-point detection by laser interferometry and thermal imaging during plasma etching showing the laser interference fringes(truncated) in (a) and detected infrared signal from the multilayer structure (solid line) and a plain silicon wafer(dotted line) etched under identical conditions in (b) 103

49 Comparison of experimental data on end-point detection for polysilicon/SiO_2(5.4KÅ) etching by plasma impedance monitoring and thermal imaging at an angle 30° to normal 105

50 Effect of back-side polysilicon film on calculated emissivity variation in (a) and experimental end-point detection in (b) 107

51 Calculated emissivity as a function of film thickness for the polysilicon/SiO_2/Si multilayer structure for various oxide thicknesses 108

52 End-point detection for polysilicon etching on patterned area (dotted line) and unpatterned area (solid line) 109

53 Detected infrared signal intensity variation across the wafer for an etch time instant of 120 second demonstrating spatial end-point detection capability 111

54 Average etch-rate counters determined by monitoring progression of end-point of etching 112

55 Calculated emissivity of a $TaSi_2$/SiO_2(3000Å)/Si multilayer structure as a function of film thickness in (a) and experimental data on end-point detection for the same structure in (b) 113

56 Calculated emissivity variation as a function of film thickness in (b) for a polyside multilayer structure shown in (a) 114

57 Calculated emissivity variation as a function of film thickness for various viewing angles for polysilicon on oxidized(1000Å) Si in (a) and $TaSi_2$ on oxidized(3000Å) Si in (b) 116

58 Spatial end-point detection of $TaSi_2$ etching with an viewing angle of 80° to normal in parallel-plate triode reactor at four different time instants (a) 250 seconds, (b) 265 seconds, (c) 275 seconds and (d) 280 seconds 117

Figure Page

59 Calculated and measured signal of 320 X 244 IR-CCD imager using narrow-band filters 120

60 Calibration of the IR camera system for F/2.35 optics 121

61 Effect of pressure on steady-state temperature in an Ar plasma 123

62 Effect of power on steady-state wafer temperature in a Ar plasma in (a) and an SF_6+20%O_2 plasma in (b) 124

63 Effect of flow rate on steady-state temperature in a Ar plasma in (a) and in a SF_6+20%O_2 plasma in (b) 126

64 Illustration of heat load on the wafer due to etching reaction for SF_6 plasma in (a) and CF_4+10%O_2 plasma in (b) 127

65 A simple model used for heat transfer analysis 129

66 Thermal time constants and the ratio of temperature drop across the silicon wafer to total temperature drop as a function of the heat transfer coefficient (h) between the wafer and water cooled electrode 133

67 Typical waveforms of the infrared signal during plasma etching of a plain Si wafer in Ar plasma 134

68 Effect of pressure on heat transfer characteristic for unclamped wafer 134

69 Effect of flow-rate on heat transfer characteristics 136

70 Gas-back-cooled chuck (a)construction and (b) typical infrared signal during the test 137

71 Calculated temperature profiles along the radius of a 4 inch wafer with a 10 W heat source applied in the center of the wafer 138

72 Calculated temperature profiles along the radius of an 8 inch wafer with a 40W heat source applied at the periphery of the wafer for h=10 J/s-m^2-K in (a) and h=100 J/s-m^2-K in (b) 140

A.1 Typical I-V characteristics of a single Langmuir probe 145

A.2 Circuit diagram of the modified tuned Langmuir probe 152

B.1 A schematic diagram of the test consisting electrical block diagram of the power supplies and connection to each electrode 156

Figure Page

B.2 End-point detection of etching Si_3N_4 on Si in a diode configuration in an SF_6 plasma 157

B.3 End-point detection of etching polysilicon on oxidized Si in a triode configuration in an SF_6 plasma 159

B.4 End-point detection of stripping photoresist on aluminum coated Si in a magnetically enhanced triode reactor in an O_2 plasma 159

CHAPTER 1

MOTIVATION AND RESEARCH OBJECTIVES

1.1 Motivation

Plasma processing is a critical part of sub-micron circuit fabrication. Plasma processes are extensively used for deposition or selective etching of materials in semiconductor fabrication. Despite of their extensive use in semiconductor manufacturing, there is considerable lack of fundamental understanding of plasma processes from the point of view of both processes and reactors involved. Often, production engineers have to resort on establishing empirical trends after tedious and time consuming compilations of the end-product characteristics and the process/reactor variables.

A particular useful aspect of plasmas is their ability to enable high-temperature-type chemical reactions to be performed at low substrate temperatures. A substrate immersed in a plasma experiences a flux of energetic ions, electrons and reactive neutrals or radicals. The reactive neutrals can react with the surface chemically and result in isotropic etching. Additionally, energetic ions and neutrals can give rise to physical sputtering or otherwise can enhance the chemical reaction on the surface and the resulting etching is more or less anisotropic in nature. Furthermore, in certain situations, polymer forming radicals such as CF_x in fluorocarbon discharges can give rise to polymer deposition resulting in simultaneous etching or deposition, or side-wall passivation.[1] This side-wall passivation and continual removal of polymer by ion bombardment at the bottom of the feature can be utilized to produce the more desirable outwardly sloped vertical features, as is commonly sought for vias and trenches, which are to be metallized by subsequent deposition. The resultant etching rates and profiles depend on the feed gas, gas flow, power, pressure, substrate temperature, reactor geometry and many other parameters in a fairly complex and

interrelated manner. In a practical etching process, the end results are optimized through an artful balance of these parameters.

It is conceptually convenient to think of the main plasma discharge as being responsible for the plasma chemistry and the formation of ions, while the sheath region adjacent to electrode being responsible for the acceleration of the ions towards the substrate surface. In reality, however, these two regions are very closely coupled by a pre-sheath as discussed in Chapter 2. In RF plasmas, the sheaths and pre-sheaths oscillate at the RF frequency and this phenomena is also not well understood. Furthermore, the highly electronegative gases used in process plasmas can produce significant amount of negative ions in the plasma, which will substantially modify the ambipolar diffusion coefficient in the bulk plasma and thus effect the "Bohm criterion" for the existence of the pre-sheath (see Chapter 2). These effects further add to the complexity in determining the connections among the tool control parameters, the plasma discharge parameters and the etch characteristics.

In general, an etch process depends on both plasma volume effects associated with the plasma chemistry and surface interactions in presence of energetic particles. A detailed knowledge of electron energy distribution function, diffusion coefficients, particle transport dynamics, cross sections and threshold energies for various types of gas-phase processes among numerous species and absorption, reaction and desorption kinetics at the etching surface is required to describe a plasma etching process. Furthermore, this kind of description depends on discharge power, gas flow, pressure and reactor geometry. Therefore, it is close to impossible to give a complete description of etching and other plasma processes. However, experimental investigations, theoretical modeling and computer simulations can identify key parameters leading to an understanding of the underlying physical and chemical mechanisms.

Experimental measurements have been a leading factor in promoting understanding of this rapidly developing field. Numerous experimental studies have been carried out to investigate many fundamental parameters and processes in glow discharges. However, most of these studies use sophisticated measurement techniques and often the measurements are carried out in impractical research type plasma reactors. In production, development and optimization of a given etch process is still commonly done on trial-and-error bases. The trend of shrinking integrated circuit dimensions and wafer scale-up places even more stringent demands on material processing requiring more detailed understanding and monitoring of the etch process.

For any particular etch process, there are a number of requirements which must be met such as: throughput(etch-rate), uniformity, selectivity, profile shape and minimization of damage and contamination. In general, it is impossible to optimize all of these characteristics simultaneously using conventional parallel-plate etch-tool configurations. To increase etch-rate, for instance, the gas density(pressure) can be raised; but, this may reduce the average ion energy and directionality at the wafer owing to collisions in the sheath and can negatively impact the anisotropy. Higher etch-rates and desired anisotropy can be achieved by increasing the power, but it will increase the average energy of the impinging ions resulting in higher damage. Any gradients in radical or ion flux and ion energy near the wafer surface can cause non-uniform etching. Changing any of the controlling parameter, especially the gas flow-rate or flow-pattern, to enhance a particular etching characteristic can adversely effect the uniformity of etching. Thus, the development of new generation plasma etching tools, which can independently control many of the etching characteristics, is highly desirable. Additionally, these new generation tools should possess, if possible, the simplicity of the parallel-plate configurations and should be easily adaptable to the existing production lines.

The ultimate goal for an etch tool would be to translate the etch requirements into proper setting for the tool control parameters e.g., power, pressure, feed gas mixture, flow, bias voltages, etc., and then proceed to etch with closed loop control. This would imply a detailed understanding of the etch-tool, as is commonly done with chemical reactors which are based largely on thermally activated processes with Arrehenius rates. Plasma activated processes are, however, far more complex involving a myriad of non-equilibrium mechanisms. There is, at present, only an empirical understanding of how to set the tool control parameters to achieve a given set of etch characteristics. The underlying mechanisms in plasma processes are not well understood and there is much less understanding of how the tool control parameters relate to the plasma discharge characteristics which actually determine the etch process. Also, there are only a limited number of plasma and wafer diagnostics which are suitable for the production environment, which makes it difficult to monitor and control the process in real-time. The implication of this limited understanding and lack of adequate diagnostics are that: (1) there is an inadequate basis for transferring a process from the laboratory to production; (2) there is often no systematic way of determining the cause of a malfunctioning process; (3) it is difficult to optimize a given process; and (4) establishing new etch processes is largely by trial and error.

There is one other extremely important reason for increasing the fundamental understanding of plasma etching and for developing real-time *in situ* process sensors. It is highly likely that as artificial intelligence develops, automated manufacturing will become more sophisticated and increasingly important for remaining competitive. Designing an expert system for plasma etching necessitates a detailed understanding of the underlying mechanisms and suitable diagnostics to make real time decisions.

1.2 Objectives of the Research

The overall goal of the research carried out for this thesis has been to obtain a basic understanding of plasma processes leading to the development of next generation plasma etching tools suitable for fabricating sub-micron devices. Specifically, this investigation has been focused on studying the issues related to plasma etching technology with the objective of gaining a fundamental understanding of the etch process and the elucidation of the underlying mechanisms of the associated plasma reactor.

This broad objective of this program have been achieved by carrying out research in two key areas. Firstly, by using well developed diagnostics to characterize and optimize various parallel-plate etcher configurations and study technologically critical etching processes; and secondly, by developing new plasma etching diagnostics suitable for process monitoring.

Scanning tuned Langmuir probes were used initially to study the RF diode and triode configurations. These studies were aimed at developing basic understanding of various physical processes in the plasma reactors. During the course of this study, the voltage phase of the two RF waveforms in triode mode was found to be one of the key factors that can be used to modulate plasma etching characteristics. The understanding developed by these studies led to the development of the magnetic multipole reactor which has proved to be an extremely versatile, high rate, low damage, low pressure reactor. The multipole reactor was used in the study of chlorine etching of polysilicon features.

The new diagnostic technique developed under this research is based on thermal imaging of wafer by an infrared camera. This technique is found to be very useful for spatial detection of end-point during polysilicon and silicide etching and has a potential of being used as a sensor for process monitoring and control. End-point

detection capability of this technique is compared with a newly developed end-point detection technique based on plasma impedance monitoring as well with a standard interferometric technique. Thermal imaging also yields real-time etching uniformity measurements and is useful for very rapid optimization of the etch process uniformity. Furthermore, this technique is useful for measuring wafer temperature and heat transfer characteristics leading to the process and reactor design optimization.

In this thesis, the utility of these diagnostics is demonstrated by the insight gained into the underlying mechanisms of several key etching processes and various reactors. Existing parallel-plate reactor configurations are also reviewed and certain modifications are proposed.

The results of this work also have significant technological consequences and applications. For example, the diagnostic methods developed during the course of this work are suitable for use in the real-time sensing of the various wafer and reactor parameters to allow the implementation of 'sensor based' control of the reactor and the process. In addition, the physical reactor models developed in this thesis have generic application to other plasma reactors used for both etching and deposition. A direct implication of the understanding gained by this research is a realization of a relatively simple, low damage, high rate, magnetically enhanced, parallel-plate etch tool configuration capable of achieving the required profile control.

1.3 Thesis Content

Chapter 2 reviews basic physical and chemical phenomena occurring in RF glow discharges important for plasma etching applications.

Chapter 3 describes an improved Langmuir probe technique for measurement of plasma properties in RF discharges. A basic understanding gained by scanning tuned Langmuir probe, induced bias and etch-rate measurements on diode and triode

configurations is presented in this chapter. A new method for modulating plasma properties by controlling the RF phase between the powered electrodes in the triode reactor is also described in this chapter.

The understanding obtained by these studies has lead to a development of a novel magnetic multipole enhanced triode reactor configuration capable of high-rate, low-pressure, low-damage and highly selective etching and is described in Chapter 4. The operation of this reactor is compared with conventional triode reactor and the utility of this reactor is demonstrated using chlorine based chemistries for etching of polysilicon features.

Chapter 5 describes a new diagnostic technique based on thermal imaging of wafer. The usefulness of this technique is described into three areas: spatial end-point detection and *in situ* determination of uniformity of etching, wafer temperature measurements, and heat transfer analysis. Discussion on each of the areas is accompanied with an introduction and the technological importance of the results.

A detailed description of the tuned Langmuir probe technique is presented in Appendix A, while plasma impedance based end-point detection technique is described in Appendix B.

For the purpose of clarity, each chapter has its own introduction, review and summary sections.

CHAPTER 2

REVIEW OF PLASMA PHYSICS AND CHEMISTRY APPLICABLE TO ETCHING REACTORS

2.1 Basic Physical Phenomena Occurring in RF Discharges

A plasma is defined as a partially ionized gas composed of ions, electrons and a variety of neutral species. A glow discharge is a plasma that exists in the pressure range of interest for plasma etching and contains approximately equal concentrations of positively charged particles (positive ions) and negatively charge particles (electrons and negative ions).

The extensive use of plasmas to activate etch processes derives from two major features of low-temperature non-equilibrium discharges. The first of these is the existence of energetic electrons with average energies in the range of 2 to 10 eV in the plasma volume. These electron break bonds to form chemically active etchant species or their precursors. The electrons are also responsible for ionization, which sustains the discharge and creates ions. These ions are often essential to the etch process. The second important feature of plasmas for etching applications is the acceleration of ions at the plasma boundary. In many configurations, the ions are accelerated by the electric field in the sheath region between the plasma boundary and wafer. This field can accelerate ions, normal to the wafer surface, with typical energies in the range of 50 to 1000 eV. The ion bombardment often results in mechanisms which allow lithographic patterns to be etched anisotropically with little or no lateral removal of material. This feature is essential to realization of increasingly high device density found in modern integrated circuits, and, is perhaps, the major reason why plasma activated etching is used so extensively.

Majority of the plasma etching equipment used for semiconductor manufacturing to-date are based on 13.56 MHz, capacitively coupled, parallel plate geometry. In these tools, the feed-gas is weakly ionized as a result of inelastic collisions between neutrals and energetic electrons. Electrons have smaller mass and can respond to the RF field. Electron can gain energy directly from acceleration in the applied RF field and continue to gain energy through elastic collisions until an inelastic collision occurs. Electron impact ionization produces electron-ion pairs that sustain the discharge against electron loss, which is normally dominated by diffusion from the plasma volume to the electrodes and the reactor walls. Electrons have sufficiently high energy and mobility to escape the plasma volume. However, the Columbic forces between the electrons and positive ions create a field, referred to as the "ambipolar field", thus resulting in a self-limiting process and thereby maintaining charge neutrality in the plasma.

The processes occurring in RF discharges are generically similar to those occurring in the positive column region of the DC glow discharges. Several gas-phase processes such as impact ionization, dissociative ionization, dissociation, recombination, relaxation, electron attachment and resonance charge transfer can occur in the plasma. The plasma chemistry responsible for creating reactive radicals and ions through these processes will be largely determined by the electron energy distribution function (EEDF), because it is a quantity upon which the rates of the electron impact processes depend.[2] Acceleration of secondary electrons emitted from the wafer/electrode surface by the sheath and energy gained by electrons in the oscillating RF field in the sheath and at the sheath edge by so-called "surf-riding" mechanism can also play significant role in determining the exact nature of EEDF.[3] The steady state electron energy distribution is a balance between energy gain and

energy loss as a result of inelastic collisions or in certain cases electron-beam plasma interaction.

In capacitively coupled plasma reactors, the power supply is usually connected to the plasma electrode through a coupling capacitor, a feature which forces the time-averaged conduction current at the driven electrode to be zero. In this case, when one electrode has a smaller area than the other (typical case for most etching tools), a time averaged negative bias forms on the smaller electrode, owing to the difference in the mobility between the electrons and the ions. For a large area ratio, this so called self induced bias can be of the order of the peak RF voltage. This produces a sheath region between the plasma volume and the electrode which has a voltage drop in the range of 50 to 1000 eV. Ions created in the plasma accelerate across the sheath and impinge on the wafer and electrode surface. Ions are heavier and therefore less mobile than electrons. Consequently, ions respond only to a time averaged electric field in the plasma. At lower pressures, ions will suffer fewer collisions in the sheath and will therefore be incident on the wafer with essentially the full bias voltage. At higher pressures, sheath collisions will degrade the monoenergetic nature of the ion flux and will result in a spread of ion energies and a scattering in ion directionality.

For discharges at lower frequencies (KHz range), the discharge resembles a DC discharge with electrodes interchanging roles as anode and cathode every half cycle. These type of discharges are also referred to as "AC discharges" as opposed to "RF discharges". In these low frequency AC discharges, secondary electron emission from the cathode sustains the discharge similar to the case of DC discharges. When the discharge frequency is above 10 MHz, the ions cannot follow the electric field due to their heavy mass and respond only to a time-averaged electric field. The electrons can respond to the instantaneous field and gain sufficient energy to sustain the discharge by volumetric ionization. Secondary electron emission may no longer be the essential

process for maintaining the discharge. Unlike DC and low frequency discharges, continuity of current across the electrode sheaths is ensured by the alternating displacement current.

2.1.1 Debye Shielding and Sheath Formation

An unique feature of plasmas is their ability to shield out externally applied electric fields and internal charge concentrations. When a test charge or an object is inserted into a quasi-neutral plasma, an equal amount of charge of the opposite sign will be attracted in the form of a cloud surrounding the introduced charge or object. This cloud shields the test charge or object from the rest of the plasma. The Debye length is the characteristic distance over which electric field created by introducing the test charge or object is reduced by the e-folding length (approximately 62%). The mathematical relationship for the electron Debye length[4] is given as

$$\lambda_D = \left(\frac{\varepsilon_0 k T_e}{e^2 n_e} \right)^{\frac{1}{2}} \qquad (1)$$

where ε_0 - is the vacuum permittivty;

n_e is the unperturbed electron concentration;

e- is the electron charge;

k- is the Boltzmann constant ; and

T_e - is the electron temperature.

A similar Debye length can be defined for ions, but in most process plasmas the electron Debye length dominates because the electron temperature is usually much higher than the ion temperature. Debye length is the order of distance over which substantial deviation from quasi-neutrality can occur except near electrodes where the

deviation from quasi-neutrality can be strongly influenced by the magnitude of the applied voltage.

In the absence of a large applied voltage at an electrode (compared to the electron thermal energy which is typically a few eV), the distance over which deviations from quasi-neutrality occur is usually of the order of several Debye lengths. Since electron diffusivity is much higher than that for positive ions, an electron retarding electric field is set-up that repels electrons and attracts ions. Sheaths(defined as regions in which the quasi-neutrality condition does not hold) are formed at all grounded and powered surfaces representing boundaries for the plasma.

2.1.2 Phenomena in RF Sheaths

The sheaths insulate the plasma from electron loss. In general, for most process plasma discharges, the plasma potential is the most positive potential in the system so that the sheaths are formed at the boundaries. In RF discharges, the dynamics of the sheaths are more complex than for DC discharges and generally are not understood. The earliest studies on the RF sheaths were made by Butler and Kino[5] and since their pioneering work, numerous papers have been published outlining improved mathematical treatments.[6,7]

An approximate description of RF sheath based on physical reasoning is shown in Figure 1. The ions cannot respond to the instantaneous field. Instead, they move through a quasi-neutral pre-sheath and acquire a directed average velocity which is of the order of ion sound speed (see Section 2.1.3) at the sheath edge S_m where the electron density is equal to the ion density at all times. The region between the wall and the S_m is called the ion sheath since it is a region of net positive charge on time averaged basis although this does not hold during the entire RF cycle.[8]

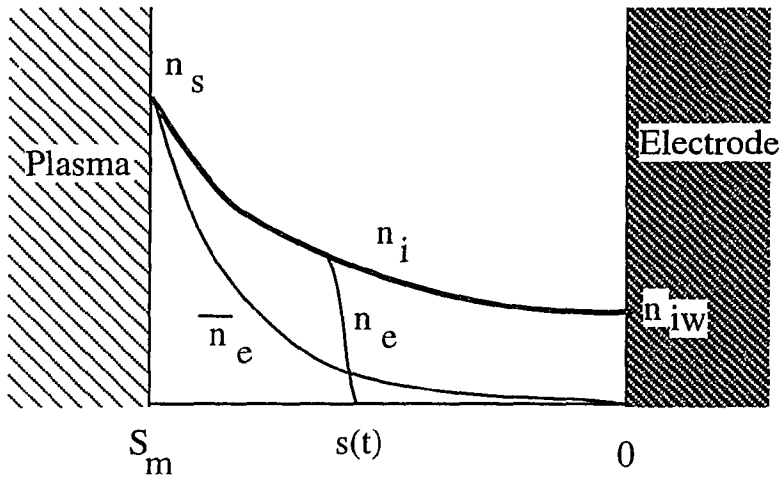

Figure 1 The sheath structure showing the ion density (n_i), the time-averaged electron density ($\overline{n_e}$) and the instantaneous electron density (n_e) at one time in an RF cycle. (Redrawn after Ref. 9)

As ions move to the wall, they gain momentum in the average sheath field and conversation of ion flux causes the ion density to fall toward the electrode/wall to a value, n_{iw}, at the wall. Since the response of an ion to the RF field can be neglected, the ion density in the sheath is stationary. In contrast, the electrons respond to the changing voltage across the sheath and their motion can be characterized most simply by the assumption of a moving sheath edge. The density profile of the electron at the moving sheath is a step-like profile.[9] The physical reason of such a step-like profile is that since the electron Debye length λ_D is much smaller than the ion sheath thickness S_m, the electron concentration falls sharply (within a few λ_D) from the charge neutrality condition (electron concentration(n_e) = positive ion concentration(n_+))at the sheath-plasma edge to n_e = 0 at the electron sheath boundary. Since the average ion

and electron currents to the wall in capacitively coupled systems must balance, and since the average sheath voltage $V_s \rangle\rangle kT_e / e$ for most of the RF cycle, the sheath must collapse for a small part of the RF cycle (when the RF voltage is maximum) enabling the electrons to reach the electrode. After the field reversal of the applied RF voltage at the electrode, the electron sheath edge moves away from the electrode. Thus, the RF field causes the sheaths to expand and decay modulating the sheath voltage and length. An electron in the glow near the sheath boundary comes under the influence of the repulsive field at the edge of the moving sheath. If the moving sheath edge has a velocity V_w and the electron velocity perpendicular to the sheath edge is V_{el}, the electron will encounter a collision and will be reflected back into the plasma with a velocity $-V_{el}+2V_w$. This phenomenon is often termed as the "surf riding" mechanism[3] or stochastic heating of electrons.[10] Electron reflection will occur at both electrode sheaths and the electron velocity after reflection will depend on the sheath thickness and the applied voltage.

2.1.3 Bohm Criterion for Existence of a Pre-sheath

A smooth transition region between the quasi-neutral plasma and the sheath exists and is known as the pre-sheath region. This region has a relatively weak electric field compared to that of the sheath which accelerates the ions from the quasi-neutral plasma toward the sheath. This implies that the ions arriving at the sheath will acquire a velocity, which is of the order of the ion acoustic speed in the pre-sheath region

$$u_s = \frac{kT_e}{M_+} \tag{2}$$

The existence of this enhanced velocity at the sheath edge and the resulting criterion requiring the existence of a pre-sheath was first demonstrated by Bohm[11] based on energy and momentum conservation arguments. The necessity for an ion

accelerating pre-sheath has become known as the *Bohm sheath criterion.* Chen[12] demonstrated the physical significance of this criterion by showing that the acceleration of ions and repulsion of electrons in a typical sheath must be such that the ion density decreases less rapidly than the electron density across the sheath. In these classical theories, an electropositive gas was normally considered with equal concentration of electrons and positive ions in the bulk of the plasma. Generally, the existence of negative ions has been ignored.

For discharges containing electronegative gases, as is the case for most plasma processing applications, the negative ions are present in copious amounts and their concentration can exceed than that of electrons.[13] This causes significant deviation in the mathematical relations derived for electropositive discharges. The concept of sheath, however, is not significantly changed for electronegative plasma due to the fact that negative ions experience only the time averaged field and are repelled from the sheath field. The negative ions do not play significant role in the sheath dynamics. However, the pre-sheath region can be significantly different due to the influence of negative ions on the pre-sheath electric field.

Braithwaite[14] showed that the acoustic positive ion flow at the sheath edge requires that

$$u_s = \left[\frac{(n_- + n_e) T_- T_e k}{(n_- T_e + n_e T_-) M_+} \right]^{\frac{1}{2}} \tag{3}$$

where subscripts +, - and e denote positive ion, negative ion and electron, respectively.

The physical significance of Eq. 3 is that as the ratio of negative ion concentration to electron concentration increases, the potential variation in the pre-sheath becomes more rapid. For a critical value of the ratio, an abrupt potential drop

occurs between the sheath edge and the plasma. This is accomplished by the formation of a "double layer" at the plasma-sheath boundary.[15] This double layer may play important part in many plasma processing applications.

Negative ions are reflected by the sheath and their generation and loss is dominated by volume processes such as attachment balanced by detachment and ion-ion recombination rather than by recombination at the wall. In an electronegative plasma, n_e can be much lower than n_+; and thus a much larger fraction of the random electron flux incident on the sheath must overcome the sheath barrier in order to equalize the positive ion flux to the electrode. This is ensured by a much lower sheath potential and hence induced DC bias than that occurs in electropositive gases.

2.1.4 Induced DC Bias

In capacitively coupled RF discharges, the time averaged conduction current to the powered electrode must be zero and this requirement is accomplished by formation of a self-induced DC potential. The formation of the induced DC bias, V_{dc}, on the RF electrode can be explained by the following arguments. Total conduction current (of the electrons and ions) to the electrode wall must be zero. However, in an RF sheath, this conduction is applicable only on a time averaged bases, i.e., averaged over a cycle. Electrons have much higher temperature (typically 2-10 eV) as compared with ions (typically 0.01-0.03 eV) and hence the electron current to the electrode is much higher than the ion current during an RF cycle if there is no DC bias to the electrode. A negative DC bias is self induced on the electrode to balance the electron and positive ion current averaged over an RF cycle. The potential drop in the sheath on a time averaged basis is the difference between the time averaged plasma potential and the self-induced DC bias on the electrode. The large potential drop in the sheath accelerates ions toward the electrode and decreases the electron current to the

electrode. Because of their mass, ions respond only to the time-average sheath field and flow to the electrode at nearly a steady rate. On the other hand, for most of the cycle the wall potential is strongly negative with respect to plasma due to the self-induced bias, the electrons are repelled from the wall and negligible current flows to the wall. Only near the peak of the RF cycle, when the RF electrode is the most positive, the sheath for electrons become thin and its potential drop is small, which allows a short burst of electrons to reach the wall. The negative charge carried by this short burst of electrons equals the positive charge of ions flowing to the wall continuously throughout the cycle. Thus, the application of the RF field produces a large increase of the time-averaged sheath potential drop (i.e. a rectification effect) comparable to the amplitude of the applied RF voltage.

A quantitative description of the DC bias in RF discharges has been hampered by insufficient understanding of RF sheaths. The classical theory of induced bias is based on the assumption that the current densities at powered electrode (area A_c) and grounded electrode (area A_a) are the same gives a relationship[16,17]

$$\frac{V_c}{V_a} = \left(\frac{A_a}{A_c}\right)^4 \tag{4}$$

Where V_c and V_a are the sheath voltage drops at the powered and grounded electrode, respectively.

The experimentally determined value of the exponent in Eq. 4 has ranged from 2 to 4.[18,19] The induced bias is known to be strongly dependent not only on the electrode area ratio but also on the power, pressure, nature of gas and electrode surface conditions.

From a simple electrical circuit representation of a plasma, it is a widely accepted practice to divide RF glow discharges into three parts: a sheath near each

electrode and a bulk plasma region between them. Figure 2 shows an equivalent electrical circuit model for RF glow discharges. The impedance of the bulk plasma, in general, can be assumed to be resistive due to the fact that conduction current by electrons dominates this region. The RF sheaths behaves like a non-linear, time varying capacitor. However, for practical purposes, it is sufficient to assume them as fixed capacitors. The impedance of the bulk plasma is much lower than that of a sheath and a large fraction of applied potential drops across the sheaths.

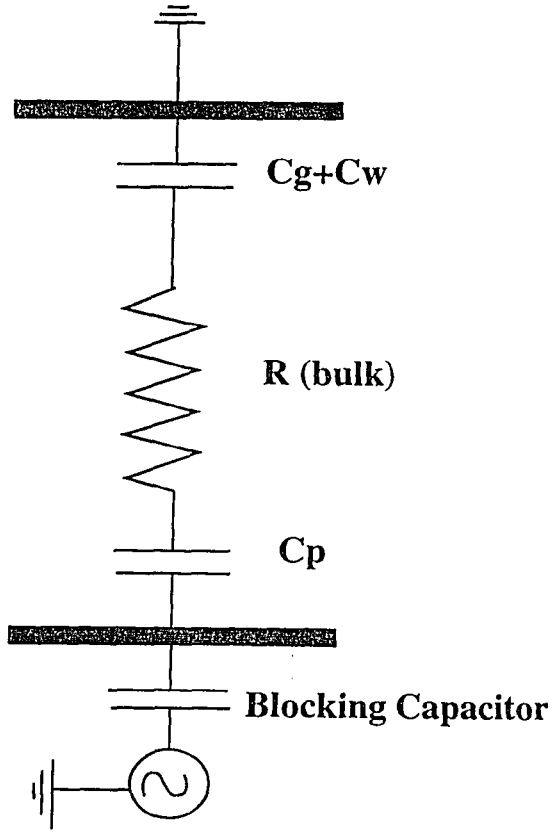

Figure 2 An electrical circuit model of RF glow discharges in a diode.

Assuming that the plasma potential is much smaller than the induced bias, the induced bias on the powered electrode can be given as[20]

$$V_{dc} = V_{rf} \frac{C_p - (C_g + C_w)}{C_p + (C_g + C_w)} \tag{5}$$

where subscripts p, g and w denote the powered electrode, grounded electrode and chamber wall sheath capacitance, respectively.

Electronegative discharges with very high negative ion to electron concentration ratio is an exception where an inductive component should be added in parallel to the bulk plasma resistance due to the inertia of the ions carrying current. Also, the sheaths are thinner and a large fraction of potential drop can occur in the bulk of the plasma.

Recently, several new theoretical models relating bias voltages to plasma and sheath properties have been published.[21,22] However, these models tend to be more elaborate to be used for predicting the values of the induced bias for a wide range of process parameter variation commonly encountered in plasma etching since these models require plasma parameters (which are generally not known) as an input.

In plasma processing, the DC bias (V_{dc}) is normally used as an energy indicator for ions impinging on the powered electrode. For a given discharge (e.g., fixed reactor geometry and feed-gas mixture), V_{dc} is generally used as being proportional to the power dissipation in the discharge. In most commercial plasma reactors, V_{dc} is measured at a point as close as possible to the electrode via a chock coil (for attenuating RF voltage) and a low-pass filter.

2.1.5 Ambipolar Diffusion and Effects of Negative Ions

Free diffusion charged species only occurs when the charge concentration is sufficiently low such that space charge effects are negligible. In the weakly-ionized plasmas used for semiconductor processing, the motion of charged particles is effected by the charge of many other charged particles and electrons and ions diffuse together in a process known as ambipolar diffusion.

When the charged particles diffuse freely, the diffusive flux Γ_i of species i is given by

$$\Gamma_i = n_i v_i = -D_i \nabla n_i \tag{6}$$

where

n_i - is the species number density;

v_i- is the average velocity of species i, and

D_i- is the free diffusion coefficient.

In the presence of an ambipolar space-charge electric field, the diffusion flux of a given charged species can be written as

$$\Gamma_i = -D_i \nabla n_i + Z_i n_i \mu_i E_s \tag{7}$$

where

Z_i- is the number of electron charge associated with that species;

μ_i -is the mobility; and

E_s- is the space-charge electric field.

For an ambipolar diffusion, the diffusion fluxes of negative and positive charges are equal.

$$\sum_k Z_k \Gamma_k = 0 \tag{8}$$

where the summation extends over all the charges.

A general expression for the ambipolar space-charge electric field can be derived from Eq. 7 and Eq. 8 as

$$E_s = \frac{\sum_k Z_k D_k \nabla n_k}{\sum_k Z_k^{\,2} \mu_k n_k}. \tag{9}$$

By substituting this expression in Eq. 7 and rearranging the result so that the flux of species i is proportional to its density gradient, the effective diffusion coefficient or the ambipolar diffusion coefficient for that species can be given as[23]

$$D_{a,i} = D_i - \frac{Z_i \mu_i}{\nabla n_i / n_i}\left[\frac{\sum_k Z_k D_k n_k (\nabla n_k / n_k)}{\sum_k Z_k^{\,2} \mu_k n_k}\right]. \tag{10}$$

At high charged particle densities, small fractional differences in densities can result in sizable net local charge densities and the resultant space-charge field retards the development of larger fractional differences. While responsible for ambipolar diffusion, this effect is also responsible for maintaining plasma quasi-neutrality, i.e., for maintaining approximate equality in local positive and negative charge density.

To get physical insight of ambipolar diffusion, the case of electropositive plasma is considered first assuming that only a single type of positive ions are present. Since $n_+ = n_e, \nabla n_+ = \nabla n_-, D_e >> D_+$ and $\mu_e >> \mu_+$, Eq. 10 reduces to

$$D_{a,e} \approx D_{a,+} \approx D_+ + \mu_+\left(\frac{D_e}{\mu_e}\right) \approx D_+\left(1 + \frac{T_e}{T_+}\right) \tag{11}$$

Normally, T_e / T_+ has a value in the range of 100. Thus the ambipolar field causes the positive ions to diffuse much faster than the free diffusion condition and at the same time the diffusion of electrons is much slower.

The presence of negative ions in electronegative plasmas necessitates modification of the ambipolar diffusion concept in at least two regards: first, there are three types of charged particles; secondly, these particles do not have same radial concentration distributions since negative ions experience inwardly directed Coulomb force from the sheath potential.

For an electronegative plasma with only single type negative and positive ions and with a large negative ion concentration such that $(n_- / n_+) >> (\mu_e / (\mu_- + \mu_+))$, μ_e can be ignored in the denominator of Eq. 10. The ambipolar diffusion constants for the charged species can be written as

$$\left.\begin{aligned} D_{a,e} &\approx D_e + \frac{\mu_e (D_+ - D_-)(\nabla n_+ / \nabla n_e)}{(n_- / n_+)(\mu_- + \mu_+)} \\ D_{a,-} &\approx \frac{(\mu_- D_+ - \mu_+ D_-) - \mu_- D_e (\nabla n_e / \nabla n_-)}{(\mu_- + \mu_+)} \\ D_{a,+} &\approx \frac{(\mu_- D_+ - \mu_+ D_-) - \mu_+ D_e (\nabla n_e / \nabla n_+)}{(\mu_- + \mu_+)} \end{aligned}\right\} \qquad (12)$$

For $\nabla n_e / \nabla n_- \to 0$, $\nabla n_e / \nabla n_+ \to 0$ and assuming that the mobility and free diffusion coefficient for positive and negative ion are the same, the ambipolar coefficients for both types of ions reduce to their free diffusion coefficients.

Thus, in an electronegative plasma, the ions diffuse much slower than the electropositive plasma while the electrons can diffuse faster than their free diffusion coefficient.

2.2 Chemical Considerations for Plasma Etching

A detailed description of chemical processes occurring in plasma is extremely complex and is not well understood. A rather simple conceptual description of various chemical processes responsible for etching can serve as a good introduction. The gas phase processes occurring in a glow discharge produce chemically reactive species (atoms, radicals and ions) form a relatively inert molecular gas. The etching gas is selected so as to generate species which react chemically with the material to be etched, and whose reaction product with the etched material is volatile.

Plasmas used for etching are referred to as non-equilibrium discharge because they are far from local thermodynamic equilibrium. Deviation from local non-equilibrium is primary due to the highly energetic electrons, which are responsible for sustaining the discharge through impact ionization of neutral molecules. Since, a distribution of electron energy exists, not all electrons are sufficiently energetic to ionize neutral molecules. Only electrons in the high energy tail of the distribution can ionize. The degree of ionization is quite low(10^{-4}-10^{-1}%) in processing plasmas. However, the degree of dissociation can reach 90% in some cases and 10% is not at all uncommon. The ease with which discharges dissociate molecules into reactive radicals is the major reason for enhanced chemical reactivity at low gas temperatures.

An ideal etch process based on solely chemical mechanisms can be described into seven steps as shown in Figure 3. These steps are as follows: generation of reactive species in plasma; diffusion of the reactive species to the surface being etched; adsorption of these species on the surface; chemical reaction on the surface resulting in a volatile by-product; desorption of the by-product from the surface, diffusion of the by-product into bulk plasma; and removal of the by-products from the etching chamber by vacuum pumps. The adsorption, reaction and desorption processes can be strongly influenced by the ion bombardment. If any of these steps fails to

occur, the overall etch cycle ceases. Product desorption is the most important step. Many reactive species can react readily with a solid surface, but unless the product has a reasonable vapor pressure so that desorption occurs, no etching takes place.

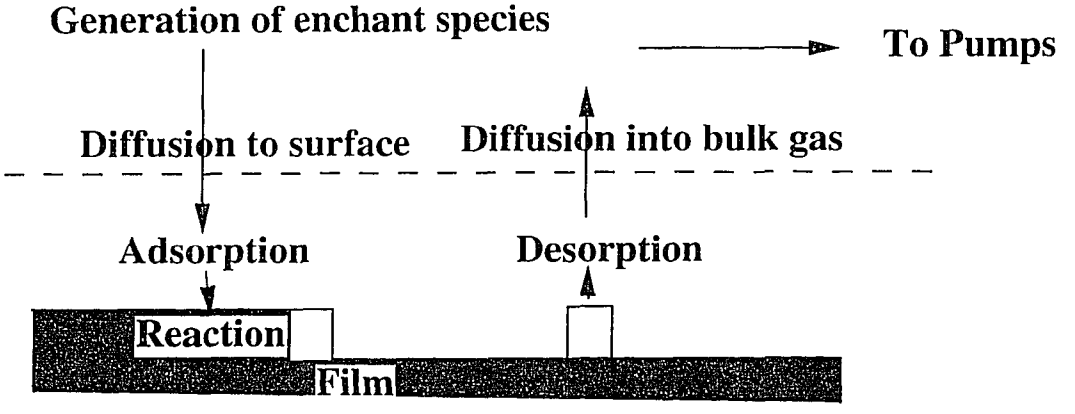

Figure 3 Primary processes occurring in a plasma etch process.

In an ideal chemical etching, the only function of the plasma is to maintain a supply of gaseous etchant species. Chemical etching is the most selective mechanism since unwanted reaction will not take place at all when their thermodynamics are unfavorable. Silicon etching by F radicals is a good example of chemical etching. In silicon/F radical etching, spontaneous reactions between F atoms and Si form SiF_4, a volatile byproduct. Flamm and his coworkers[24] have determined an etch rate ratio (selectivity) of silicon to silicon dioxide exposed to fluorine atoms of 41:1 in a purely chemical etch process. However, purely chemical attack, unlike other forms of plasma etching is isotropic. In reality, a combination of chemical and physical (such as ion

bombardment enhanced) etch mechanisms are used to obtain the desirable etch-rate, selectivity and anisotropy. Anisotropy can be induced by energetic ion bombardment enhanced reaction or by inhibitor layer formation. A good example of ion bombardment enhanced etching is the etching of Si in chlorine. An undoped single crystal Si surface is not etched by Cl_2 or Cl atoms at room temperature.[25] When the surface is simultaneously exposed to high energy ion flux, silicon chlorides are formed in a rapid reaction. Inhibitor ion-enhanced etching requires two conceptually different species; enchants and inhibitors. The inhibitor species form a thin film on the surfaces being etched. Only the bottom surfaces experience energetic ion bombardment due to directionality of ions. The film is continuously removed from the bottom surfaces by sputtering and etching takes place. Vertical side-walls experience little or no ion-bombardment and no etching takes place on vertical side-walls. The resultant etch-profile is anisotropic. In fluorocarbon plasmas, CF_2 radicals can be used to form a thin polymeric inhibitor films.[26]

A large variety of fluorine, chlorine, bromine and oxygen based etching plasmas with a profusion of gas additives are used in the semiconductor industry. In most cases a specific gas mixture is based on a great deal of empirical evidence obtained for a particular application rather than real fundamental understanding of the relevant plasma chemistry. Nevertheless, certain basic insights have proven to be helpful in formulating gas mixtures.

A classical example of using gas additives to obtain desired selectivity is the addition of O_2 or H_2 to the CF_4 feed gas. Pure CF_4 plasma etches silicon with a selectivity in the range of 2:1. The addition of small amounts of O_2 to CF_4 plasma is known to increase the F radical concentration in the discharge dramatically increasing both the etch-rate of Si etching and selectivity of Si to oxide etching. This is due to the reaction of oxygen with CF_x radicals forming CO, CO_2 and COF_2 and producing

more free fluorine by reducing the recombination of F atoms with CF_3.[27] When H_2 is added to CF_4, the Si etch-rate decreases monotonically as the percentage of H_2 is raised and eventually etching stops. The percentage of H_2 where Si etching stops depends upon the plasma etching process parameters, e.g. the total gas flow, power, pressure. Atomic H scavenges atomic F in the gas phase to form HF.[28] Addition of H_2 also increases selective deposition of polymer formation on Si surfaces. Similar results can also be obtained by using C_2F_6/H_2 or CHF_3 gas chemistries and these gases are widely used to etch SiO_2 more selective to Si.

A high Si to oxide selectivity can also be achieved in a glow discharge of SF_6 which provides a fluorine-rich plasma and is used extensively. Chlorine and bromine based chemistries are also widely used for Si and Al etching. Chlorine and bromine atoms have similar etching characteristics with respect to these materials, but chlorine is more widely used because it has much higher vapor pressure, is less corrosive and tends to form somewhat less toxic byproducts. O_2 is widely used for photoresist stripping and for removing polymers from the system.

2.3 General Description of Parallel-Plate Etch Tools

Parallel-plate configurations are widely used as a single wafer etcher due to their simplicity and ability to direct energetic ions normal to the surface being etched. Production etching systems can have a variety of configurations depending upon the parameters of a process needed to be controlled as well as the specific applications of the system. The most common, commercially used, single wafer etching tool configuration today is the parallel-plate planer diode. One of the two electrodes of the diode configuration is capacitively coupled to the RF power supply through an impedance matching network and the other electrode is grounded. The frequency of the RF power supply can range from several KHz to several MHz.[29] However, the

most common commercially used frequency is 13.56 MHz (an industry standard reflecting FCC regulations) and discussion in this thesis is limited only to the plasma processes occurring in a 13.56 MHz discharge. The major limitation of the diode configuration is the strong coupling between the plasma generation and the induced bias. As the power is increased to enhance ionization in plasma, the induced bias also increases and can cause substantial substrate damage.

Triodes, as their name implies, are tri-electrode discharge systems. In triodes, two of the three electrodes are powered while the third electrode is normally at the ground potential. The plasma parameters (ion energy, electron temperature and charged particle concentrations) can be somewhat independently varied in a triode relative to an equivalent diode system.[30]

2.4 Significance of Low Pressure Plasma Etching

In the plasma etching literature, various terms such as plasma etching (referred to etching wafer placed on grounded electrode in a relatively high pressure plasma) and reactive ion etching or reactive sputter etching (referred to etching wafer placed on powered electrode in a relatively low pressure plasma) are used extensively to describe various process conditions. However, plasma etching term is widely used today to describe all process conditions because it is a well accepted fact now that ions are rarely the etchant and neutrals are responsible for almost all reactive etching.[31] In this thesis, the term plasma etching is used instead of reactive ion etching to describe low pressure etching processes.

The stringent requirements of anisotropy for sub-micron circuit fabrication has demanded that etching is performed at lower pressures (<100 mTorr). This is due to the fact that the mean free path increases with decreasing pressure. As the mean free path is increased, the scattering in ion directionality and energy in the sheath region is

minimized and better anisotropy is achieved. The relationship between the mean free path and the pressure is given as[32]

$$\lambda = \frac{kT}{\sqrt{2}\pi P d^2} \tag{13}$$

where

T-is the temperature;

k- is the Boltzmann constant;

P-is the pressure; and

d- is the molecular diameter.

Figure 4 shows the calculated mean free path (MFP) for air molecules (average molecular diameter of 3.7Å) as a function of pressure. As can be seen from this figure, the MFPs are comparable to the system dimensions below 15 mTorr. Calculations of average MFP for the gases commonly used in plasma etching is extremely difficult due to presence of multiple species. However, the MFP for most of the gases used in plasma processing is within a factor of two for that of air at the same pressure. It should also be noted that the gas density linearly decreases with pressure. It is required that the ionization and dissociation efficiency of the reactor should be high enough to maintain adequate etch-rates at lower pressures. Reduced etch-rate at lower pressures in conventional parallel-plate tools places a lower limit on low pressure operation and a trade-off is usually made between etch-rate and pressure.

To-date, most of the experimental and theoretical work has been directed at obtaining a fundamental understanding of discharges at high pressure.[33,34] Consequently, low pressure plasma kinetics are very poorly understood. Low pressure plasma is expected to behave differently than the high pressure plasma but there is no significant understanding of low pressure plasma behavior at present.

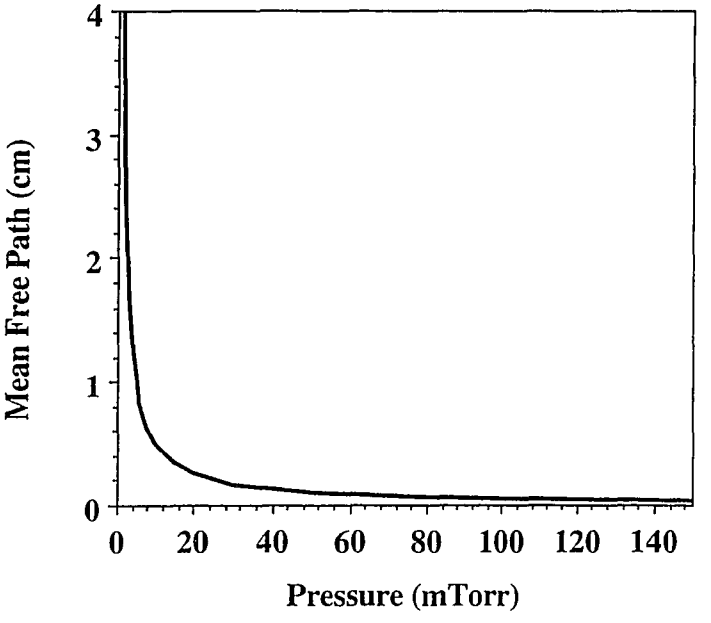

Figure 4 Calculated mean free path as a function of pressure for air.

Lower pressure operation will also effect the concentration of negative ions in the discharge. Generally due to reduced attachment cross-sections at low pressure, the relative concentration of negative ions can be expected to be lower. Thus, the overall behavior or kinetics of low pressure plasma can be expected to differ significantly from those at higher pressure.

CHAPTER 3

CHARACTERIZATION OF CONVENTIONAL PARALLEL-PLATE TOOLS

The main objective of this study was to obtain some basic insights of plasma behavior in production compatible parallel-plate etching reactors in the pressure range of 10 to 100 mTorr. Spatial distributions of plasma density (axial and radial) in various reactor configurations were measured for a range of process gases (Ar, O_2, CHF_3 and SF_6). A scanning Langmuir probe with a special tuning circuit to overcome RF interference was utilized for spatial mapping of plasma density. Etch-rate and induced bias measurements were also made to gain more insight into basic plasma processes occurring in low pressure RF glow discharges.

Two reactor configurations were studied in detail, namely the diode and the triode. Figure 5 shows the schematic diagrams of the two reactor geometry studied. In the diode mode, the upper electrode is grounded while in triode both the parallel plate electrodes are powered with the chamber walls serving as the grounded third electrode. The powered electrodes can be excited either at the same frequency[35] or using a dual frequency scheme.[36] For the work reported in this thesis, the single frequency excited triode reactor configuration was investigated. Process development on triode reactors is done on empirical basis and very little work has been reported describing fundamental plasma processes occurring in the triode configuration. Recently, the relative electrical phase applied to two driven electrodes in the single frequency excitation scheme was found to have significant effect on etching characteristics.[37] However, this effect is not well understood. In this chapter, characterization of the plasma generated in triode with an emphasis on the effect of phase is described.

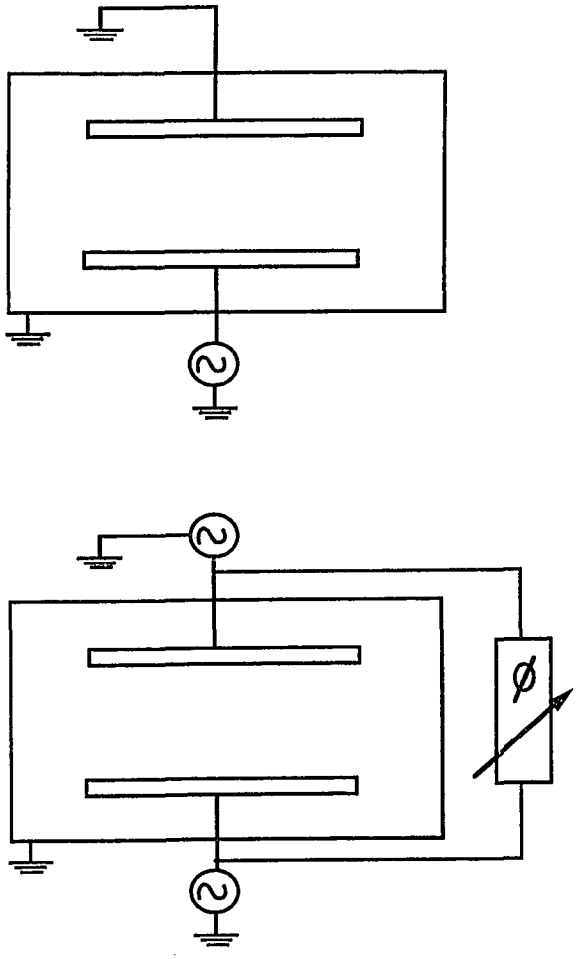

Figure 5 Schematic diagrams of (a) diode and (b) triode reactor configurations.

3.1 Experimental Set-up

Experiments were performed on a parallel-plate reactor with 8"-diameter stainless-steel electrodes. The overall reactor configuration is shown in Figure 6. The electrodes were surrounded by a 0.5" wide ground shield placed 0.1" away from the edge of the electrodes. The average distance between the ground shield edge and chamber wall was estimated to be 4 inches. The separation between the electrodes can be adjusted by independent motion of any of the electrodes. The electrodes were fitted with identical

"L" type matching networks and were powered by independent 1KW RF (13.56 MHz) power supplies excited by a single excitation source and a phase delay network. The forward and reflected powers were monitored by Bird wattmeters inserted between the power supplies and the matching networks. The flow of gases was controlled by MKS flow controllers, while the pressure was monitored by a Baratron capacitance manometer and regulated by a throttle valve. In the diode mode, the top electrode was grounded and only bottom electrode was powered. In the triode mode, both electrodes were powered with the stainless-steel chamber walls acting as the grounded electrode. The phase between the two RF waveforms applied to the upper and lower electrode was varied between 0° to 360° using the phase delay network.

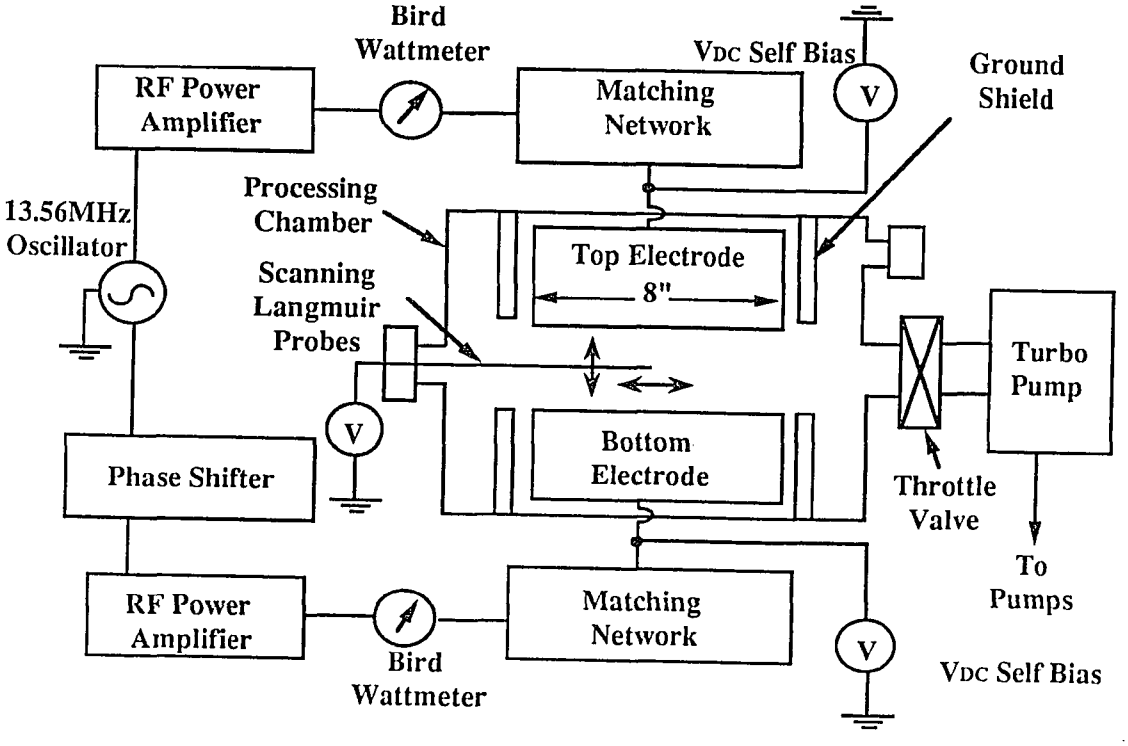

Figure 6 Schematic diagram of the experimental set-up.

The reactor was also fitted with two independent scanning Langmuir probes. One probe was capable of scanning the plasma region radially across the electrode at a specified height while the other can scan the central plasma region between the electrodes axially (in the "z" direction). Both probes were constructed from a 0.5 mm-diameter cylindrical platinum wire mounted in a hollow circular ceramic insulator (2 mm in diameter). The probe tip was adjusted to be 3 mm in length and was parallel to the electrode surfaces in both the cases.

3.1.1 Scanning Tuned Langmuir Probe Diagnosis of RF Glow Discharges

A tuning circuit was developed to overcome RF interference on the probe characteristics. The main function of the tuning circuit is to generate series resonance condition forcing the probe tip to float with the instantaneous potential and enabling the probe to measure only time averaged plasma characteristics. A basic circuit developed by Paranjpe and his coworkers[42] was modified to minimize interference from second and third harmonics of the fundamental 13.56 MHz frequency. More details on the nature of RF interference and the design and operation of the tuning circuit are presented in Appendix A. Prior to each Langmuir probe measurement, the probe was cleaned by operating it in strong electron saturation region and allowing the probe tip to glow red hot. Reproducibility of measurements was ensured by repeating measurements periodically.

The experimental arrangement for the practical implementation of the tuned Langmuir probe technique is illustrated in Figure 7 for radial scanning. The tuning network was mounted outside a feed-through connected on a bellows. The motor driven bellows allowed the scanning of the probe tip from the center of the electrode to a distance 8 inches away. Similar scanning mechanism was used to scan the other probe axially (with probe tip parallel to the electrode surfaces) the region between the

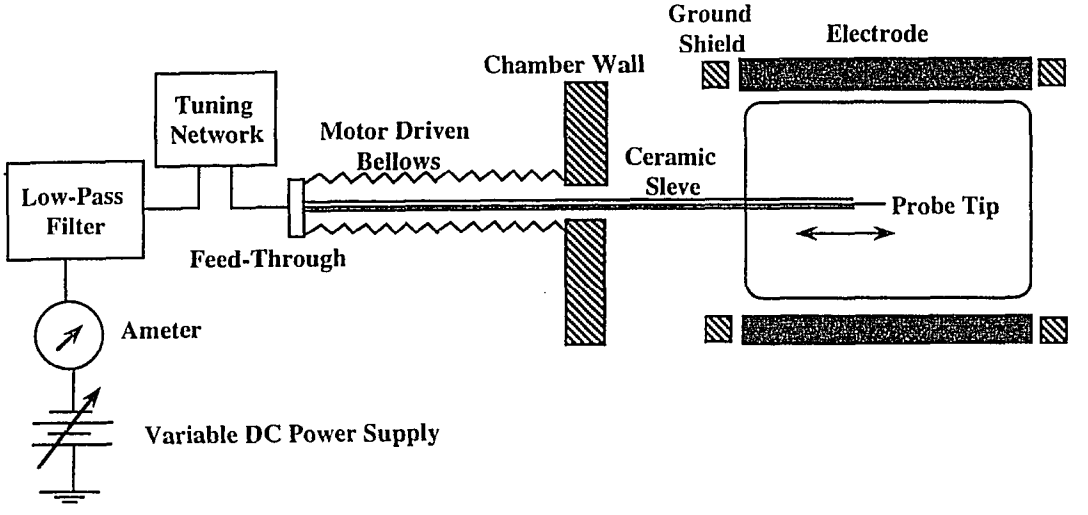

Figure 7 Experimental arrangement for the practical implementation of the tuned Langmuir probe technique.

parallel-plate electrodes. With the discharge energized, the tuning circuit was adjusted until the floating potential (measured on a DC coupled oscilloscope) of the probe placed in the center of the discharge is maximized. At this point the circuit is tuned, since maximization of the floating potential is a necessary and sufficient criterion for minimizing RF interference. To infer the plasma density distribution, the probe was biased negative with respect to ground (-80V) and scanned across the plasma. Tuning of the probe was not changed during a scan. Some detuning of the probe characteristic is possible; since, the probe to chamber capacitance may change with probe position. However, as shown by Paranjpe[42], the minute detuning is not expected to change probe characteristics in saturated ion current region if the probe is sufficiently biased negative with respect to the plasma.

Measurements were performed for a range of conditions in Ar, SF_6, O_2 and CHF_3 discharges. The discharge was allowed to operate for a while before the measurements were made to in order to ensure steady discharge operation. For each operating point, the matching network was adjusted to minimize reflected power. In all cases, reflected power was less than 3% of the forward power. If the applied negative bias on the probe is too large to substantially modify the plasma characteristics the induced DC bias should reflect the disturbed plasma condition. During a scan, the undisturbed plasma condition was ensured by monitoring the change in induced bias to be lower than ±5 V.

As discussed in Appendix A, the current to the probe in ion saturation region can be given as

$$I_+ = eAn_+\left(\frac{-1.27e(V - V_p)}{2\pi M_+}\right)^{\frac{1}{2}} \tag{14}$$

where

V_p- is the plasma potential;

V- is the probe potential; and

A-is the area of the probe tip.

The bulk plasma can be assumed equi-potential (nearly constant V_p). For a constant applied probe voltage, V, the saturated ion current should vary linearly with the positive ion concentration in the plasma and can be used to infer the positive ion distribution in the bulk plasma. In the electrode sheath region, however, the saturated ion current does not represent ion density due to the presence of very high sheath fields and also due to the fact that the ion flux becomes more anisotropic in the sheath region.

3.2 Diode Configuration- Results and Discussion

3.2.1 Effect of Pressure on Axial Plasma Density Distribution and Induced Bias

Spatial mapping of plasma density in axial direction was obtained by measuring saturated ion current of the tuned Langmuir probe as a function of probe position (scanned in a region between 0.2 inches above the lower electrode and 0.2 inches below the upper electrode) in Ar, O_2, CHF_3 and SF_6 discharges. The distance between the electrodes was fixed to 3 inches and the power applied to the lower electrode was set to 400 W for these measurements.

In order to obtain a broader view of plasma behavior, induced bias on the powered electrode was also measured for a wide range of power (varied from 20 to 400W) and pressure conditions. In general, for a given reactor with constant electrode areas, the DC bias decreases with pressure and increases with power. There are two factors responsible for the pressure dependence. The first factor is the effective ground electrode area which increases at lower pressure due to poor plasma confinement causing the effective ground electrode to powered electrode area ratio to increase. The second factor is the mean free path of charged particles which decreases with increasing pressure causing the sheath thickness and the potential drop across it to decrease. An increase in power is normally accompanied with an increase in the applied RF voltage. Since the sheath on the powered electrode has much smaller capacitance as compared with the sheath at the grounded electrode, majority of the applied RF voltage drop occurs in the powered electrode sheath causing the induced bias to increase with the power. However, the variation of induced bias as a function of pressure for various powering conditions is different for different gases and can be useful to infer plasma behavior.

3.2.1.1 Ar Discharge

Figure 8(a) shows the measured saturation ion current representing the spatial plasma density for Ar discharges as a function of probe position for various pressures. As can be seen in Figure 8(a), the saturated ion current continuously increases with pressure and the ion density has cosine-like distribution with a peak in the bulk plasma region followed by a decrease towards both electrodes. As the pressure is increased from 5 mTorr to 100 mTorr, the peak in plasma density shifts towards the powered (bottom) electrode. Between 100 to 200 mTorr pressure, however, the peak in plasma density moves away from the powered electrode. Figure 8(b) shows the measured V_{dc} for Ar discharge as a function of discharge pressure and power. Approximately 400 experimental data points were used to generate the two dimensional bias mapping plot. For Ar discharge, the induced bias gradually increases with power and decreases with pressure. However, between nearly 80 mTorr to 120 mTorr, the V_{dc} changes at much slower rate as compared with the other pressure ranges.

Recently, Meyyapan[43] has observed qualitatively similar ion density profile and increase in ionization with pressure in his theoretical simulations for low pressure Ar discharges in a symmetric system. Ar is a electropositive gas and the ambipolar diffusion constant for positive ion is higher than its free diffusion value. Generation of electron-ion pair in the bulk of the plasma is balanced by the recombination at the wall resulting in a density profile having a cosine-like distribution. The shifting of density peak away from the electrode above 100 mTorr suggests that the plasma characteristic is changed. Induced bias measurements also suggest some kind of transition in this pressure range. It can be seen from Figure 8(b) that this transition is nearly independent of applied power. The pressure dependent transition suggests that the transition plasma sheath from a collisionless to collisional regime. This argument agrees well with the experimental findings by others.

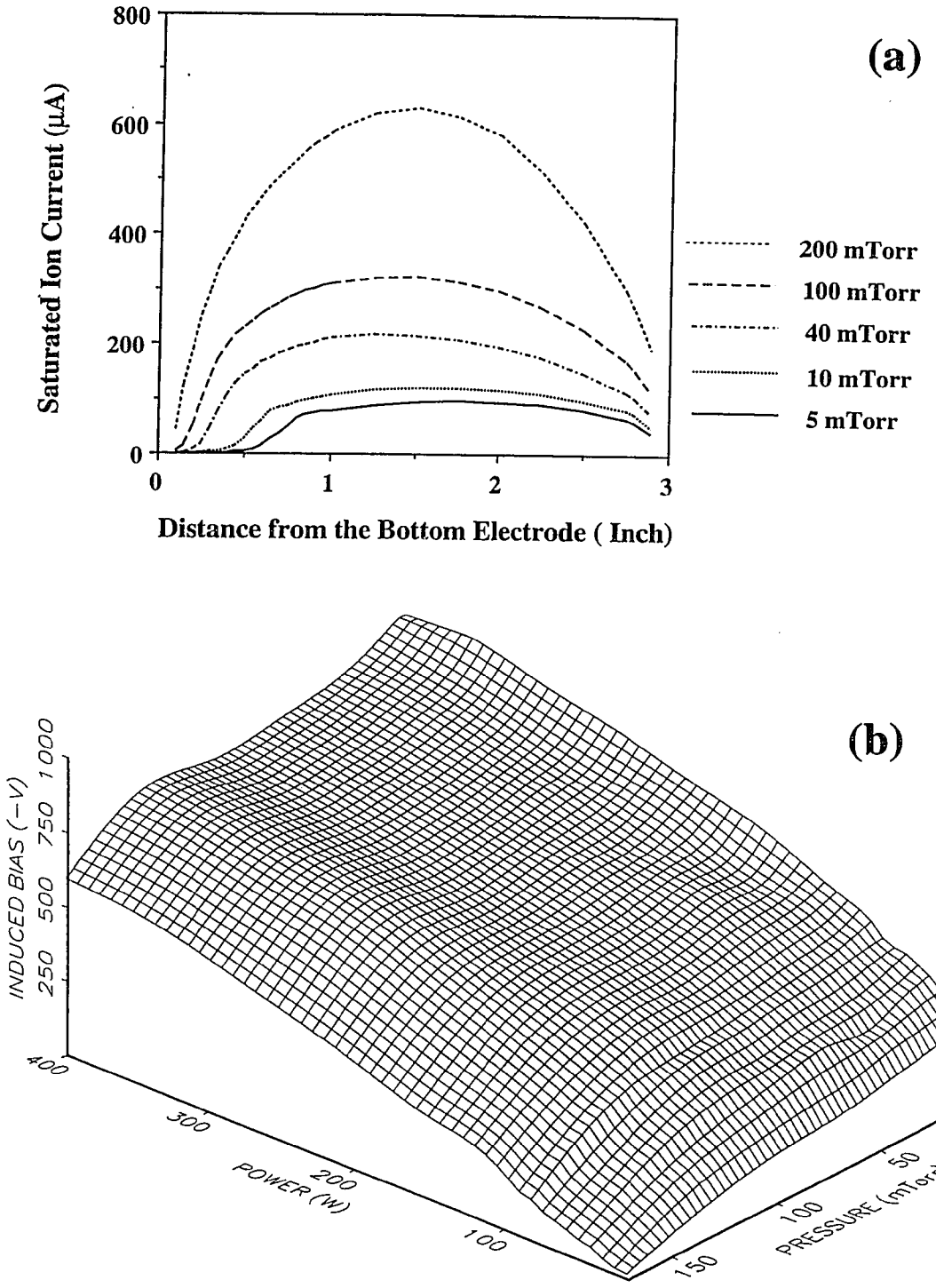

Figure 8 Axial variation of saturated ion current for various pressures in (a) and pressure and power dependence of induced bias in (b) for Ar plasma.

Kohler[44] and his coworkers found the plasma sheath in an Ar discharge to be collisionless at 50 mTorr while Bisschops [45] found the sheath to be collisional above 100 mTorr in their ion energy measurements at electrode surface. Recently, Doyle[46] and coworkers have also observed a transition in Ar plasma characteristics above 100 mTorr in their Langmuir probe measurements. The shifting of density peak away from the electrode also suggests the transition from stochastic heating of electrons at sheath boundary to Ohmic (bulk) heating in the plasma volume.

3.2.1.2 Oxygen Discharge

Plasma density distribution for dissociative molecular gases was found to be remarkably different than the inert Ar gas. The pressure dependence of density distribution function for O_2 plasma is shown in Figure 9(a). For oxygen plasma, the saturated ion current increases as the pressure is varied from 5 mTorr to 25 mTorr and has a cosine-like distribution. The peak in plasma density moves toward the powered electrode. At 40 mTorr, the plasma density peak occurs near the powered electrode sheath edge and plasma density start to decrease more linearly towards the top electrode. The trend continues as the pressure is raised further. However, the magnitude of saturated ion current in bulk plasma decreases as the pressure is increased from 40 to 100 mTorr. The pressure and power dependence of induced bias in O_2 plasma is shown in Figure 9(b). The induced bias increases gradually with power and decreases with pressure. Comparison of Figures 9(a) and 8(a) shows that the saturated ion current is lower for O_2 plasma as compared with Ar plasma. This is expected to be true for all dissociative gases since the dissociation thresholds are generally lower than the ionization thresholds and a large amount of neutral-electron collisions will result in dissociation rather than ionization. The transition from a cosine-like distribution to a linearly decreasing distribution takes place at around 40 mTorr suggesting that negative ions have started to

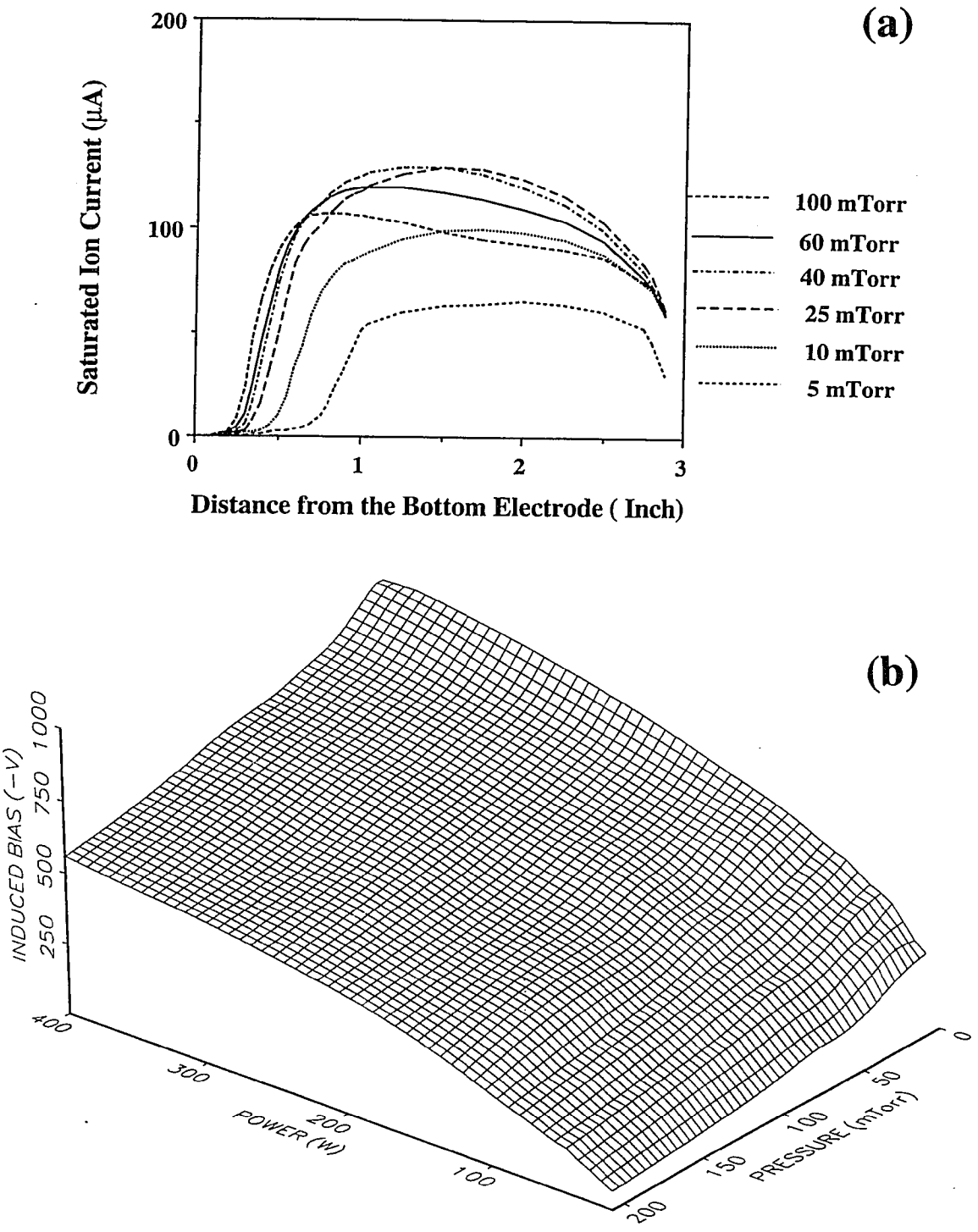

Figure 9 Axial variation of saturated ion current for various pressures in (a) and pressure and power dependence of induced bias in (b) for O_2 plasma.

contribute to the overall distribution profile. Electron attachment cross-sections for electronegative gases are known to increase with pressure and the ratio of negative ion concentration to electron concentration also increases with pressure. The results in Figure 9(a) suggests that the O_2 plasma behaves like an electropositive plasma below 40 mTorr and above this pressure, the reduced ambipolar diffusion constants for ionic species and ion-ion recombination in the bulk plasma changes the plasma density distribution. The variation in induced bias as a function of pressure is very gradual suggesting that the negative ion concentration is not high enough to modulate the pre-sheath properties. Electron energy distribution measurements by Sabadil[47] in a 27.1 MHz O_2 discharge also showed that the negative ions are present in a significantly low amount in O_2 discharges in the pressure range investigated.

3.2.1.3 CHF_3 Discharge

For a CHF_3 plasma, as shown in Figure 10(a), the transition from a cosine like distribution to a linearly decreasing distribution occurs between 10 to 20 mTorr. The saturated ion current decreases up to 60 mTorr. Above 60 mTorr, another peak in the plasma density starts to appear near the sheath edge of the grounded electrode. The plasma density in the central plasma region continue to decrease while the peak near the grounded electrode sheath edge continue to rise slowly. The induced bias in a CHF_3 discharge, as shown in Figure 10(b), also decreases with pressure and increases with power. For very low power (<50W) and pressures above 200 mTorr, the induced bias is very close to the ground potential.

The decrease in the saturated ion current with pressure above 20 mTorr can be due to two reasons. Energy of electrons is expected to be higher at low pressure due to higher mean free path.[48] Hence, more ionization rather than the dissociation can take place. Also, since the saturated ion current is inversely proportional to the mass of the

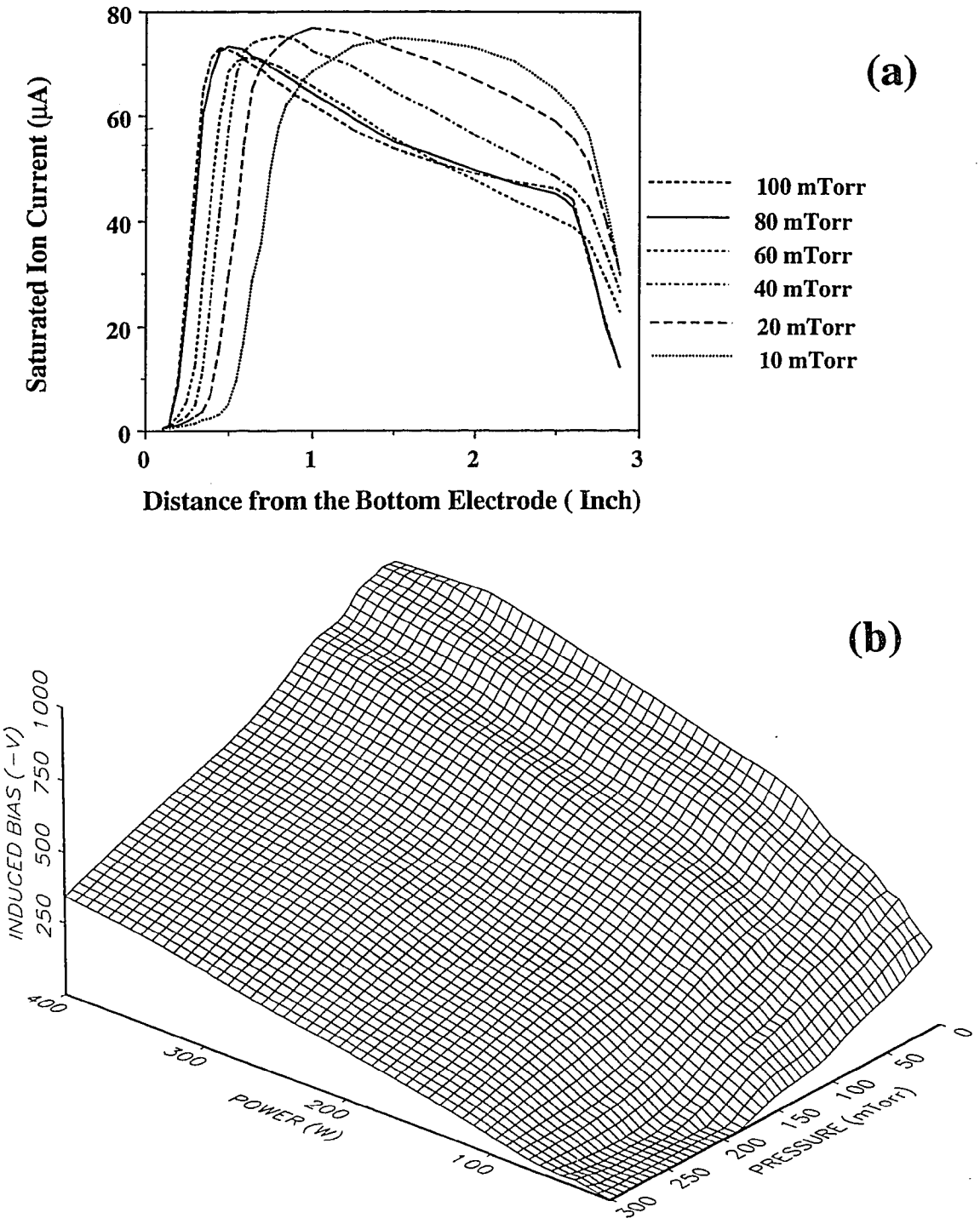

Figure 10 Axial variation of saturated ion current for various pressures in (a) and pressure and power dependence of induced bias in (b) for CHF_3 plasma.

dominant positive ion in the plasma, the possibility of a transition from a lighter to a heavier dominant ionic species with an increase in pressure can not be neglected. The second peak in the plasma density near the sheath boundary of the grounded electrode above 60 mTorr suggests that negative ions start playing a role in the pre-sheath region adjacent to the ground electrode sheath. It can be concluded that CHF_3 plasma contains more number of negative ions as compared with O_2 plasma for the same pressure. Recently, Haverlag and his coworkers[49] have estimated the negative ion to electron density ratio in the range of 5 to 8 for a CHF_3 discharge at 50 mTorr using a combination of microwave interferometry and laser induced photodetachment techniques. They also found that this ratio decreases with pressure. The more rapid transition of induced bias to ground potential in the very low power, high pressure regime suggests the amount of negative ions present in the plasma for these conditions is such that the negative ion kinetics dominate the electron kinetics.

3.2.1.4 SF_6 Discharge

For an SF_6 plasma, as shown in Figure 11(a), the plasma density profile has a shape close to the linearly decreasing distribution at 25 mTorr and the saturated ion current continue to decrease up to 60 mTorr. At 10 mTorr pressure (not shown in the figure), the density profile looks very similar to that of 25 mTorr but the saturated ion current is nearly 20% higher in magnitude. Above 60 mTorr, the peak density near the powered sheath start to increase along with the density in the bulk of the plasma and nearly about 100 mTorr, a second peak in density appears near the sheath boundary of the grounded electrode. As the pressure is further increased to 136 mTorr, the peak near the grounded electrode sheath boundary increased further and becomes comparable to the one near the powered electrode sheath boundary.

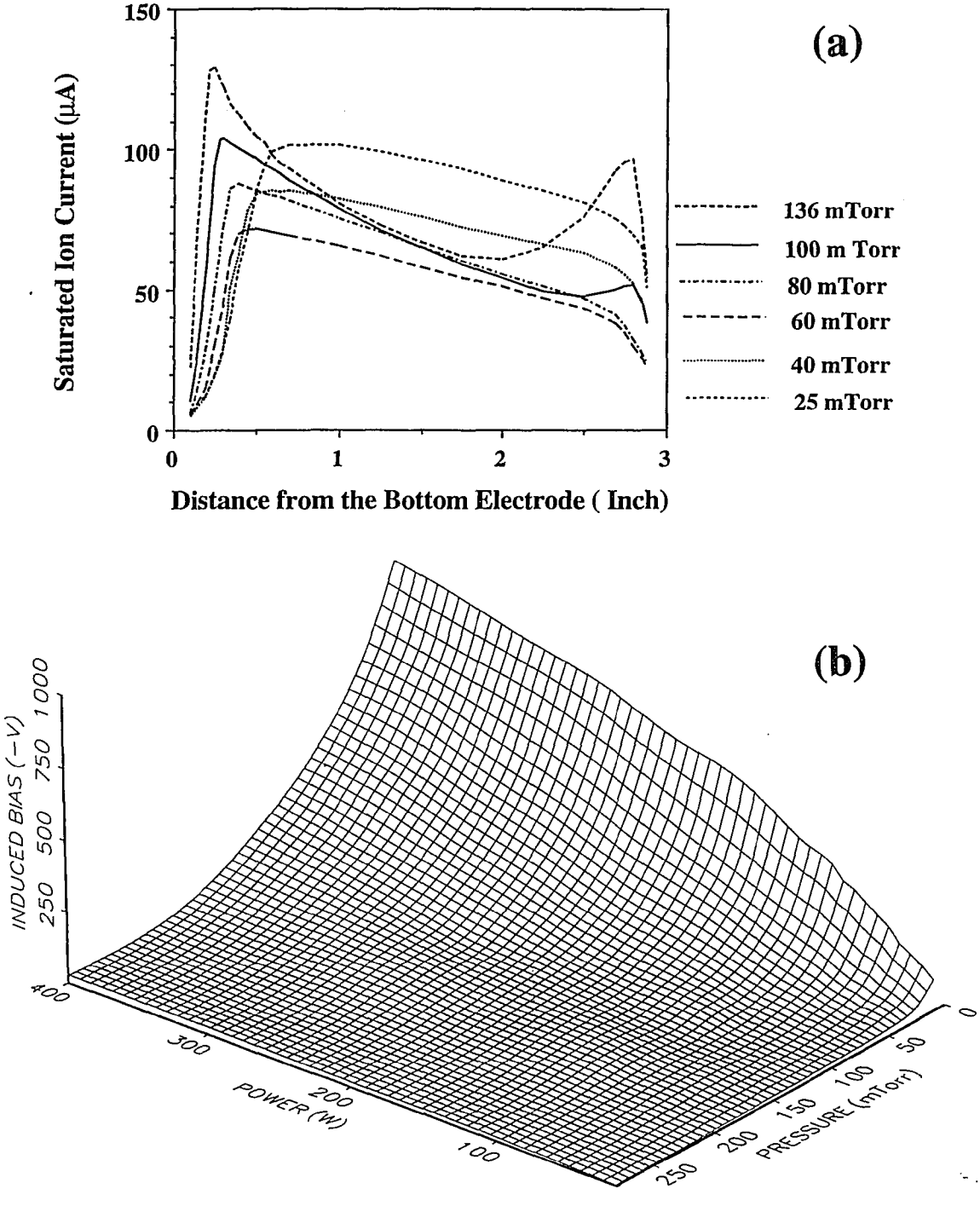

Figure 11 Axial variation of saturated ion current for various pressures in (a) and pressure and power dependence of induced bias in (b) for SF_6 plasma.

The induced bias for SF_6 discharge, as shown in Figure 11(a), behaves markedly different as compared with other gases investigated. The change in bias with power and pressure is much more rapid and the induced bias is nearly at ground potential for a large range of parameter space. The threshold at which transition to ground potential occurs is strongly dependent on power and pressure. At very low power(20W), the transition to nearly zero bias condition occurs at 50 mTorr. As the power is increased, the transition pressure also increases reaching to almost 230 mTorr for 400W power.

The presence of a more pronounced peak near the grounded electrode sheath region at 100 mTorr in the SF_6 plasma as compared with CHF_3 plasma suggests that SF_6 has more amount of negative ions. This difference is due to the fact that SF_6 and CHF_3 has very different electron attachment cross sections.[50] In fact, Picard[51] has measured the negative ion to electron concentration ratio of nearly 100 in a SF_6 discharge at 100 mTorr and shown that the ratio increases to nearly 1000 as the pressure is increased to 200 mTorr. The rapid transition of the induced bias to ground potential in Figure 11(b) suggests that the concentration of negative ions in plasma is strongly dependent on pressure and power in SF_6 discharge. SF_6 is known to have a large electron attachment cross section for low (~0 eV) energy electrons. As the power is raised, the average electron energy increases and the probability of formation of negative ions decreases.

3.2.2 Radial Distribution of Plasma Density

Figure 12 shows the radial distribution of plasma density measured 1.0 inches above the bottom electrode for Ar, O_2 and SF_6 at 100 mTorr. As can be seen from the figure, the plasma density of Ar decreases from the center towards the grounded walls showing that plasma generation in the bulk region is balanced by the ambipolar diffusion losses

to the reactor walls in the radial direction. The plasma density in the bulk of the discharge for O_2 is nearly flat and decreases in a region between the electrode edge and the grounded reactor wall. The SF_6 plasma density increases from the center of the electrode towards the edge of the electrode, peaks near the edge and then decreases away from the edge. This density profile suggests that negative ion-positive ion recombination in the bulk of the plasma dominates the bulk plasma region.

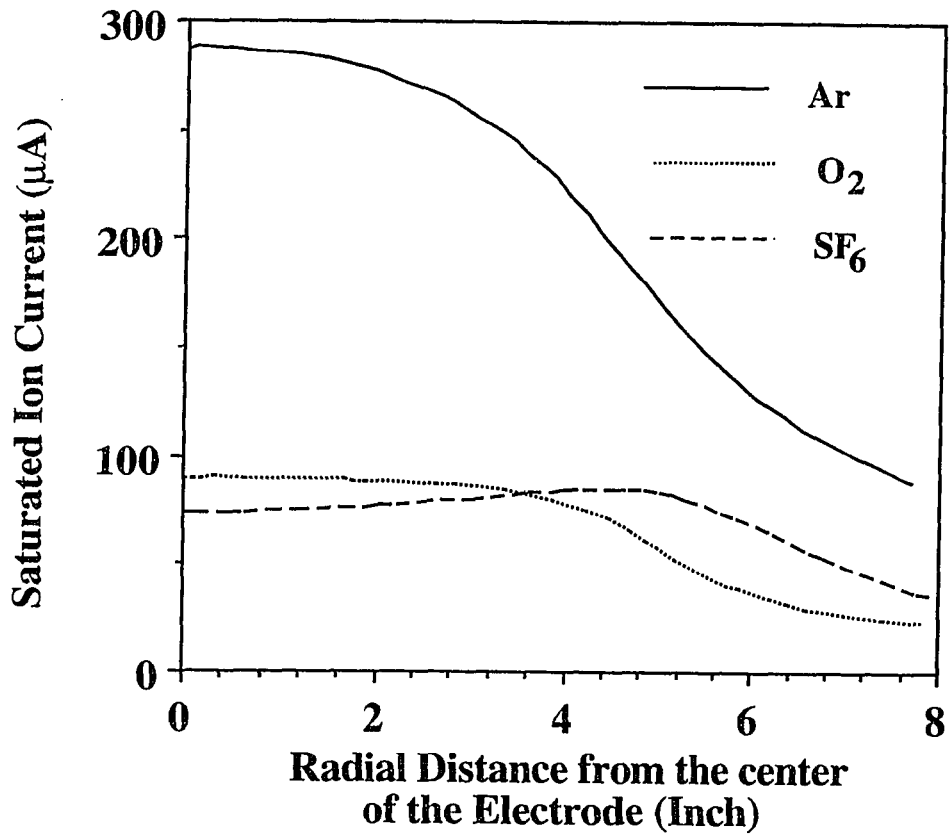

Figure 12 Radial plasma density distribution for Ar, O_2 and SF_6 plasma at 100 mTorr.

3.3 Triode Configuration- Results and Discussion

3.3.1 Effect of Pressure on Axial Plasma Density Distribution in Ar and Oxygen

Figure 13 shows the axial plasma density distribution in a triode for Ar at various pressures (180° phase, 200W/electrode power). As can be seen from the figure that the sheath thickness on both electrodes is nearly the same. The plasma density has a peak in the center of the discharge and follows a cosine-like distribution. The saturation current increases with pressure similar to the diode configuration. Comparison between Figure 13 and Figure 8 shows that for the saturated ion current in the triode case is nearly 60% higher than the diode case. Thus, for the same amount of total power, the plasma generation in triode is more efficient than the diode case. Higher ionization efficiency of the triode reactor can be explained by the following arguments. The effective sheath area, where electrons can gain energy, is much larger than the diode so that more electrons can gain energy from the oscillating sheaths. Also, the electron loss to the walls at grounded potential is minimized since the effective ground wall area is smaller for triode as compared with the diode configuration. The overall effect is the improved ionization efficiency.

Figure 14 shows the axial plasma density distribution for O_2 for various pressures (180° phase). The plasma density distribution is cosine-like at lower pressure and the saturated current increases with pressure up to 60 mTorr. Above 60 mTorr, the density distribution starts to become uniformly distributed (flat) between the electrodes and the saturated ion current decreases with pressure. At 100 mTorr, a very flat plasma density distribution is obtained. It should also be noted that the magnitude of saturated ion current for triode is 50% higher in the center of the discharge at 100 mTorr as compared with the diode case (Figure 9).

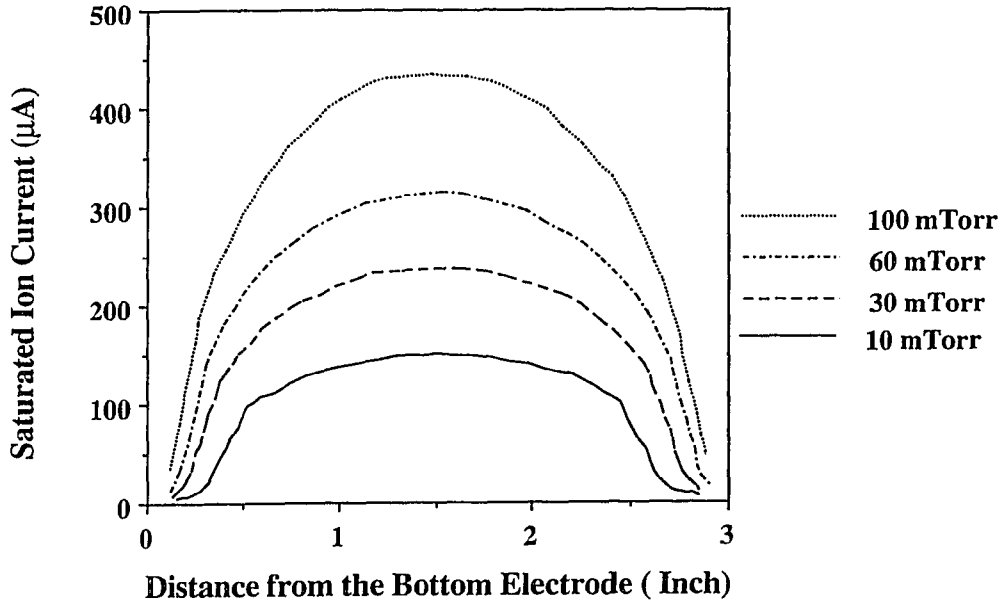

Figure 13 Axial plasma density distribution in a triode for Ar for various pressures (180° phase, 200W/electrode power).

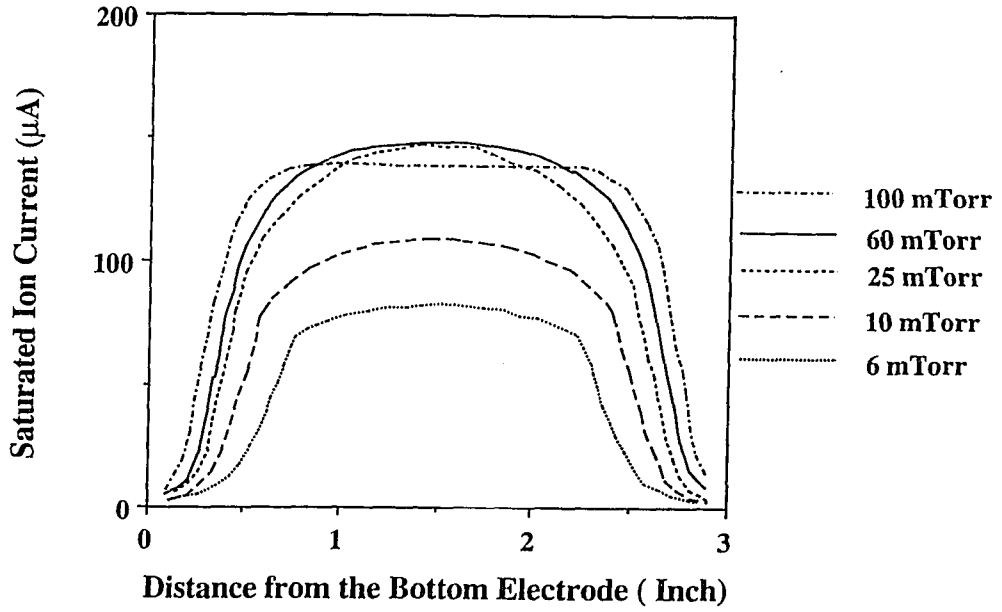

Figure 14 Axial plasma density distribution for O_2 for various pressures (180° phase, 200W/electrode power).

3.3.2 Effect of Phase on Induced Bias

Induced bias measurements represent the simplest way to gain some of the basic insights of the phase effect. Figure 15 shows the effect of varying phase between 0° to 300° on induced bias for O_2, CHF_3 and SF_6 discharges at 100 mTorr. As can be seen from the figure, the bias dependence on phase is sinusoidal and the value of induced bias on the lower electrode is maximum for out-of-phase (180°) excitation. Also, the effect of phase is more pronounced in SF_6 than other gases. Figure 16 shows the lower electrode bias dependence on phase for different power conditions for SF_6 at 30 mTorr. The induced bias has a sinusoidal dependence on phase for all power levels. It is interesting to note that when one electrode has low levels of power applied to it, the phase dependence of induced bias of the low powered electrode is more significant. Also comparison of Figure 15 and Figure 16 for SF_6 with 200W/electrode power shows that the phase effect is less pronounced at lower pressures.

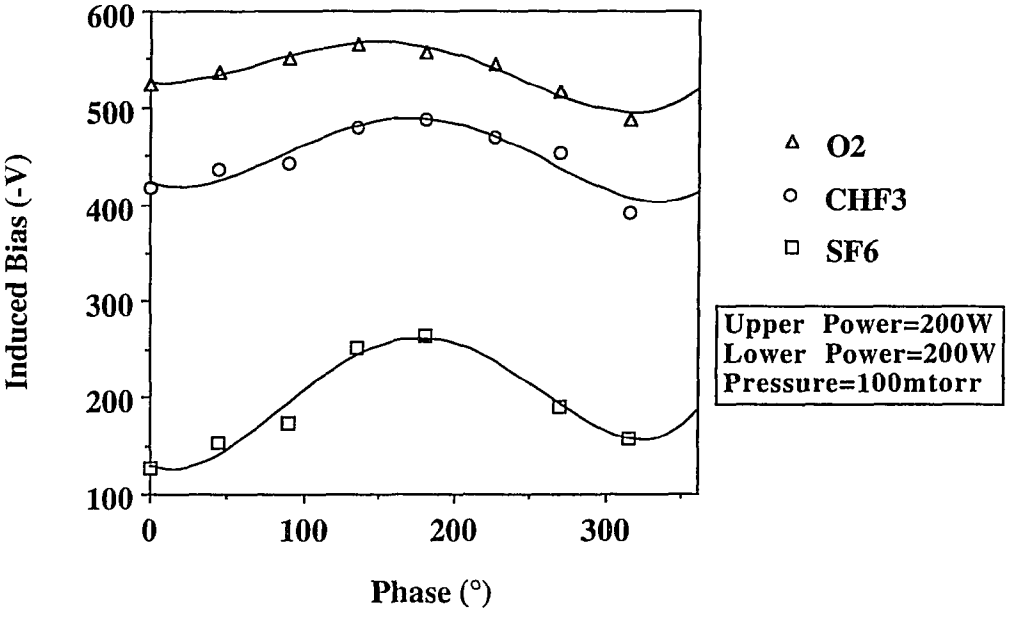

Figure 15 Effect of varying phase between 0° to 320° on induced bias for O_2, CHF_3 and SF_6 discharges at 100 mTorr.

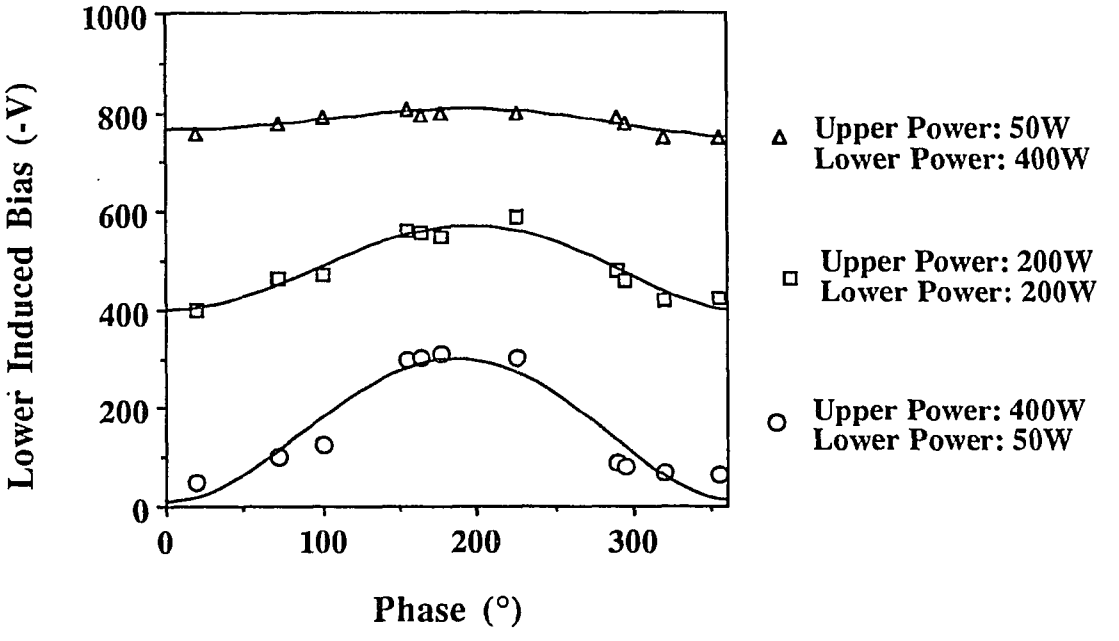

Figure 16 Lower electrode bias dependence on phase for different power conditions for SF_6 at 30 mTorr.

3.3.3 Effect of Phase on Radial Plasma Density Distribution

Figure 17 shows the radial plasma density distribution measured 1.0" above the bottom electrode for three phase conditions in O_2 plasma at 100 mTorr. As can be seen from the figure that the phase did not have significant effect on plasma distribution profile. However, the plasma density in the bulk of the plasma is higher for 180° excitation and is lower for 0° excitation. The phase was found to have a qualitatively similar (but less in magnitude) effect on plasma density distribution for Ar plasma.

Figure 18 shows the radial plasma density distribution measured 1.0" above the bottom electrode for three phase conditions for CHF_3 plasma at 100 mTorr. As can be seen from this figure that the plasma is more confined in the central region between the parallel-plate electrodes for 180° phase. For 0° phase excitation, the plasma density is lower in the central region and is higher in the region away from the electrode as compared with the 180° phase excitation condition.

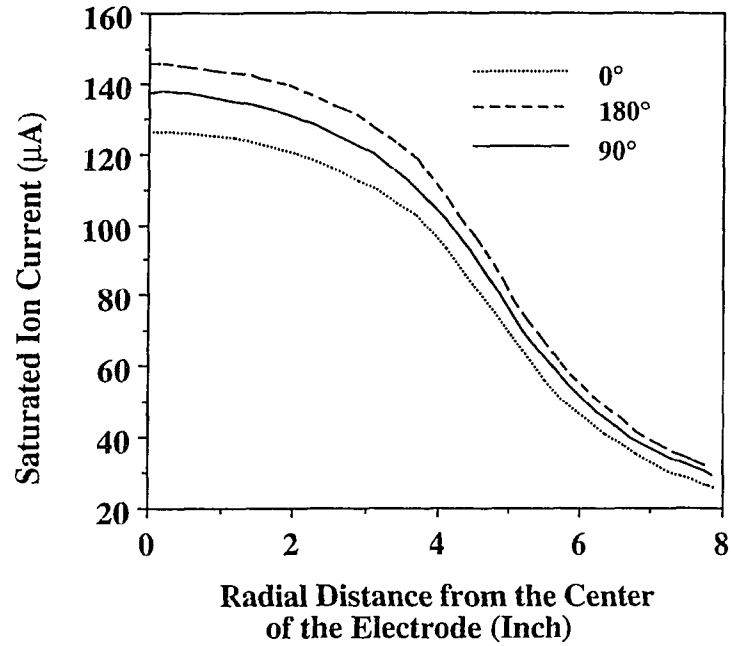

Figure 17 Radial plasma density distribution measured 1.0" above the bottom electrode for three phase conditions in O_2 plasma at 100 mTorr.

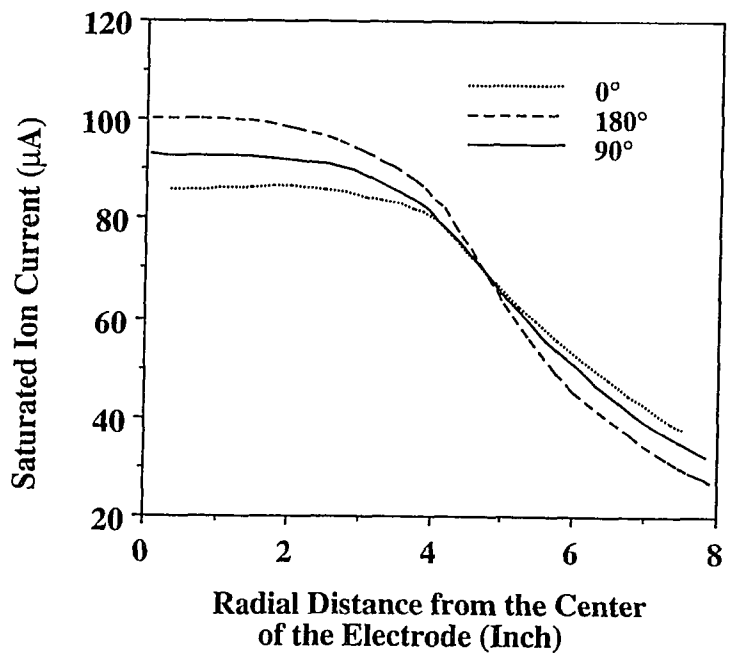

Figure 18 Radial plasma density distribution measured 1.0" above the bottom electrode for three phase conditions in CHF_3 plasma at 100 mTorr.

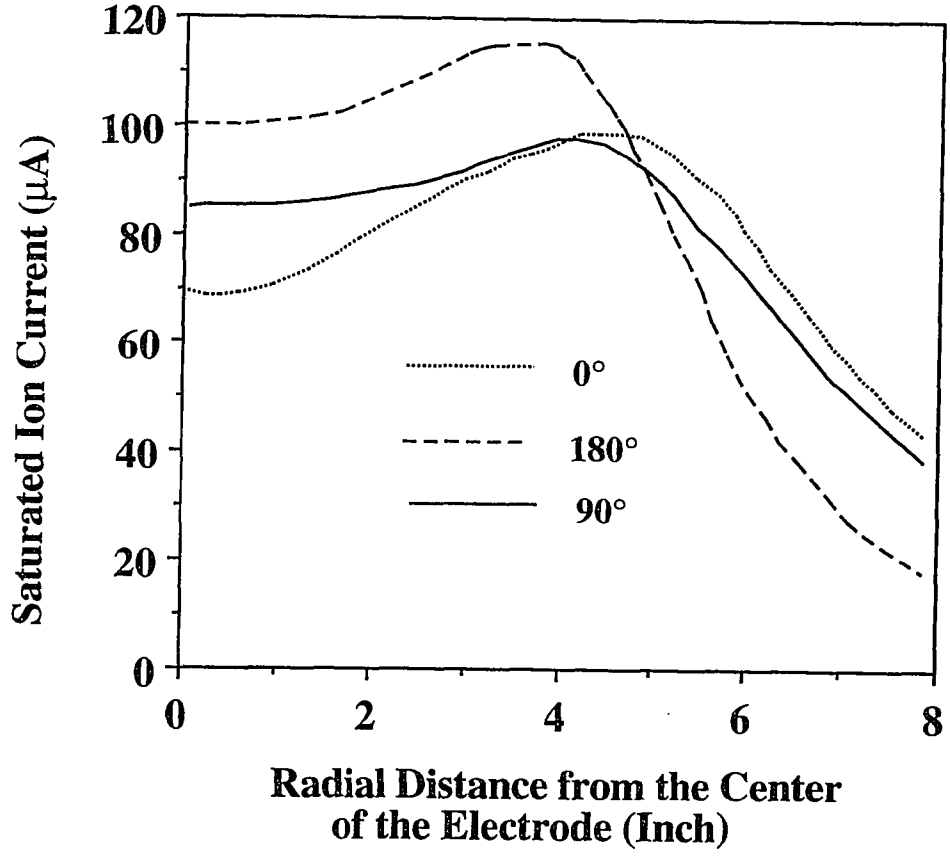

Figure 19 Radial plasma density distribution measured 1.0" above the bottom electrode for three phase conditions in SF_6 plasma at 100 mTorr.

Figure 19 shows the radial plasma density distribution measured 1.0" above the bottom electrode for three phase conditions of SF_6 plasma at 100 mTorr. As can be seen from this figure, for the phase angle of 180°, the plasma is better confined in the region between the powered electrodes and plasma density is higher in this region as compared with 0° phase excitation.

3.3.4 Effect of Phase on Axial Plasma Density Distribution

The phase effect was studied in more detail using axial scanning Langmuir probe measurements in O_2 and SF_6. Figure 20 shows the axial plasma density distribution in O_2 discharge at 100 mTorr for three phase conditions. It is evident from the figure that the plasma density is higher for 180° excitation. However, the phase has very little effect on axial plasma density distribution in O_2 discharge.

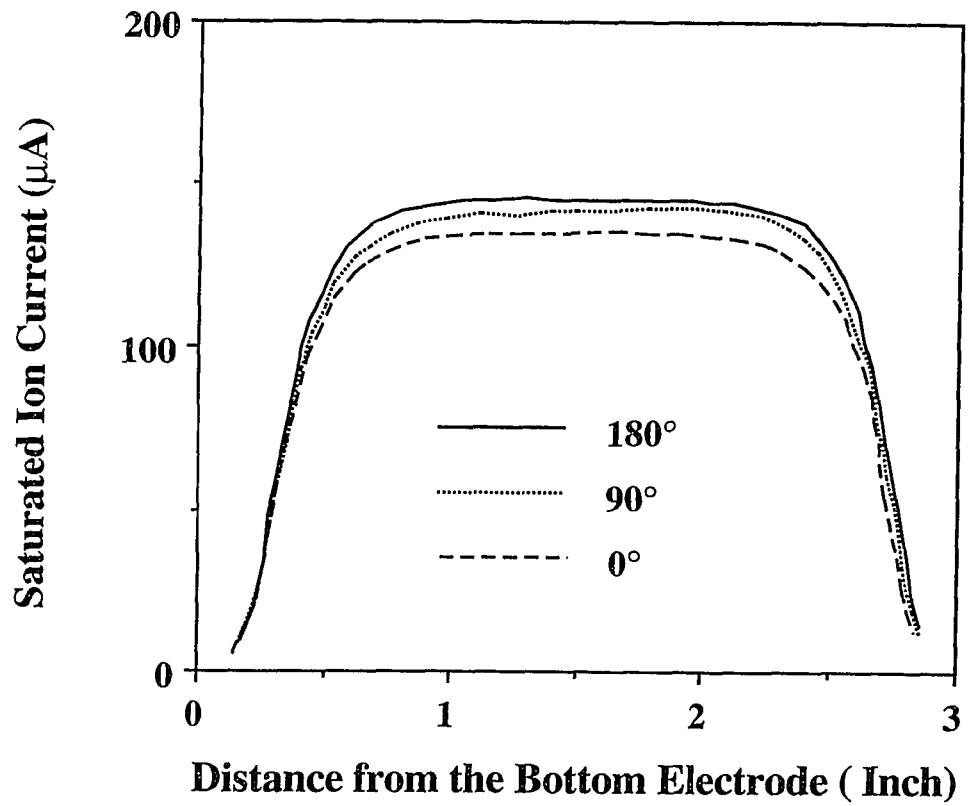

Figure 20 Axial plasma density profile for three phase conditions in O_2 plasma at 100 mTorr.

Figure 21 shows the axial plasma density profile for three phase conditions for SF_6 plasma at 100 mTorr. The plasma density distribution was found to be strongly affected by the phase. For out-of-phase excitation (180°) the plasma density peaks in the center of the discharge decreases towards the electrodes. A small peak near the sheath boundary of the top electrode is attributed to difficulty in obtaining proper tuning condition (reflected power = 10W) for the top electrode in this particular case. For in-phase excitation (0°), the plasma density has a peak near the sheath boundary of each electrode. For a 90° out-of-phase excitation, the plasma density profile has an intermediate profile.

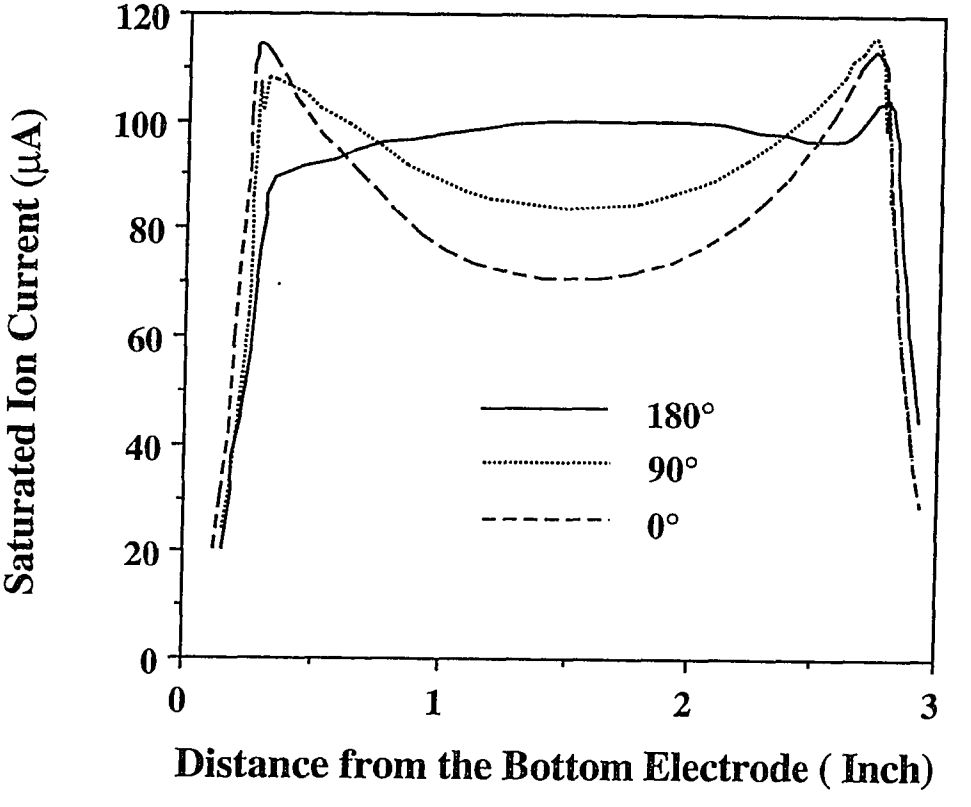

Figure 21 Axial plasma density profile for three phase condition in SF_6 plasma at 100 mTorr.

The initial understanding obtained by these measurements suggests that the phase effect may be due to the sheath phenomena. For 180° phase excitation, sheaths on both electrodes oscillate 180° out-of-phase with respect to each other. During contraction of sheath on one electrode, the sheath on the other electrode is expanding and electrons continuously gain energy alternatively from both the sheaths. For 0° excitation, the sheaths on both electrodes decay and expand simultaneously. Thus, during the expansion of the sheath, electrons gain energy while during contraction of sheaths, electrons in the bulk of the plasma cool down. Therefore, the electron energy distribution function is expected to be different in both cases. For strongly electronegative gases such as SF_6, the negative ions are more likely to be formed during the contraction of the sheaths for the case of 0° excitation since the average energy of electrons is decreased. For 180° excitation, the electrons gain energy continuously and negative ions are less likely to be formed. Thus, the plasma density distribution for SF_6 plasma is strongly effected by the phase. As the pressure is decreased, the average energy of electron in SF_6 plasma is expected to rise and the phase effect becomes less significant.

3.3.5 Effect of Phase on Etch-rates

The plasma density profiles suggest that the etch-rate should be higher for 180° phase excitation. This is indeed the case. The etch-rates measured across the wafer for polysilicon etching in 100 mTorr SF_6 plasma are plotted in Figure 22 (200W/electrode power). For 180° excitation, the etch-rate in the center of the wafer is nearly a factor of two higher than the 0° excitation and uniformity of etching is much better for 180° out of phase excitation. For a comparison purpose, the etch-rate measurements for a diode case with 400W power (same total power) are also platted in the same figure.

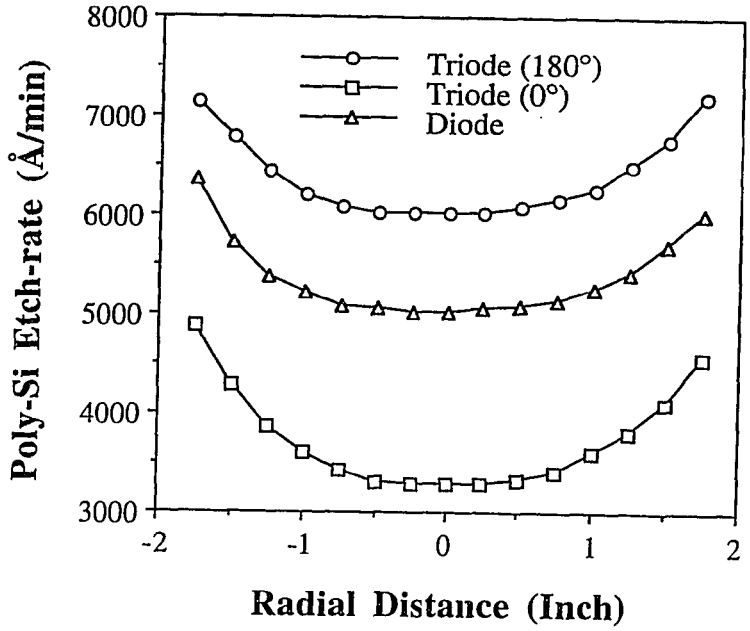

Figure 22 Etch-rates measured across the wafer for polysilicon etching in 100 mTorr SF_6 plasma.

In fact, etch-rate in diode is nearly 60% higher as compared with the 0° excitation. Etching of polysilicon in SF_6 plasma is known to due to spontaneous reaction between F radicals and Si. Thus, the concentration of reactive species produced near the wafer surface in the triode reactor is higher for 180° excitation and lower for 0° excitation than the diode configuration for same total applied power.

Oxide etch-rates as a function of phase in CHF_3 plasma (100 mTorr, 200W/electrode power) as shown in Figure 23 also show phase dependence. However, the etch-rate ratio of 180° excitation to 0° excitation is only 1.25. Thus, the phase effect is much less pronounced in CHF_3 plasma as compared with SF_6 at 100 mTorr as suggested by the induced bias (Figure 15) and plasma density measurements (Figures 18 and 19).

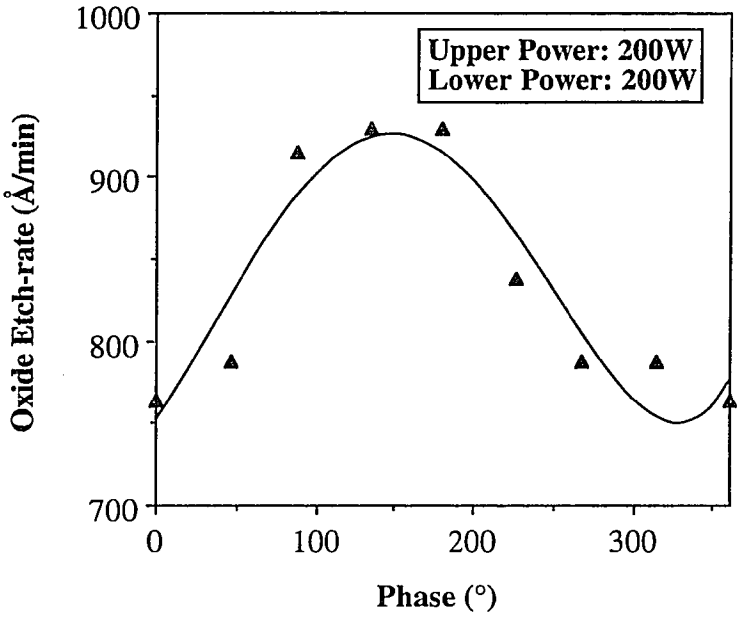

Figure 23 Oxide etch-rates as function of phase in CHF_3 plasma.

The phase effect was also investigated using a newly developed combined wavelength and frequency modulation infrared absorption spectroscopy (CWFMS).[38] Initial data obtained using this technique have shown that the concentrations of various radicals in SF_6 and CHF_3 discharges are also strongly affected by the phase.[39]

Work on characterization of parallel-plate diode and triode reactor configurations is being continued. Results described in this chapter along with some new results on investigation of the effect of various process parameters such as inter-electrode distance, power and pressure on plasma properties such as density distribution, electron temperature and plasma potential will be published in a near future.[40,41]

3.4 Summary

Spatial distributions of plasma density (radial and axial) in capacitively-coupled parallel-plate etching tools were measured for a range of process gases (Ar, O_2, CHF_3 and SF_6) using a scanning tuned Langmuir probe. Two reactor configurations have been studied in detail, namely the diode and triode. In the diode mode, the upper electrode is grounded while in the triode mode both the parallel-plate electrodes are powered with the chamber walls serving as the grounded third electrode. Using an RF phase shifting network, a single 13.56 MHz RF oscillator and two slaved power amplifiers, the voltage phase difference between the powered electrodes in the triode mode can be electrically controlled. The plasma density distribution was found to be dramatically different for dissociative molecular etching gases as compared to inert gases. The density distribution was also found to be strongly affected by the electronegativity of the process gas. The triode configuration was found to have higher ionization efficiency as compared with the diode configuration for the same total power. In the triode mode, the relative phase between the RF voltage waveforms applied to the electrodes strongly affects both the magnitude and distribution of the plasma density. For out-of-phase excitation (180°), higher etch-rates and better etch-uniformity are obtained as compared with the in-phase excitation(0°). These effects are more pronounced in SF_6. The effect of phase was found to increase with pressure and also found to be higher for strongly electronegative gases.

CHAPTER 4

MAGNETIC MULTIPOLE ENHANCED TRIODE REACTOR

4.1 Need for Magnetic Enhancement

To obtain faithful pattern transfer, it is desirable to operate reactors at low pressures to minimize, for example, scattering of ions while producing a dense uniform plasma to maximize etch rates.[52,53,54] Also, aspect-ratio dependent etch-rate non-uniformity (known as RIE lag) is known to be improved at low pressures.[55] Generally, the performance of parallel-plate diode configuration degrades at lower pressures, that is, below operating pressures of 30 mTorr.[56] In non-magnetic parallel-plate tools the plasma density drops to unacceptable levels as observed by very low etch rates and the induced bias on the electrodes rises to produce ion bombardment energies in excess of 1 KeV. These high values of the induced DC bias greatly enhance the possibility of wafer damage, erosion of photoresist and contamination from reactor walls and electrode surfaces. Some non-magnetic enhancement schemes to increase plasma density have included single or multi-frequency excited triode reactor configurations. These reactors do indeed decouple the plasma generation from the substrate bias up to some extent but the plasma density and uniformity drops considerably at pressures below 10 mTorr and it is also very difficult to sustain stable plasma at lower pressures.

In order to extend the operation of a parallel-plate reactor to very low pressures (<10 mTorr), some form of magnetic enhancement is required. Typically, magnetic fields are used to increase the collision probability between electrons and neutral feed-gas molecules and thereby generating dense, stable plasmas at lower pressures. When a magnetic field is applied, charged particles are "tied" to the magnetic field lines and gyrate around them.

The radius of gyration of a charged particle around a magnetic field is known as Larmor radius and is given by

$$R_L = \frac{mV}{eB} \tag{15}$$

where

m- is the mass of the particle;

B-is the magnetic field density;

V -is the velocity perpendicular to B; and

e -is the electronic charge.

A charged particle also experiences Lorentz or E X B force and many other forces depending upon the nature of applied E and B fields. A number of publications outline the motion of a charged particle in an electromagnetic field and a very comprehensive account on the subject is given by F. F. Chen.[57] However, in RF plasma, the E field oscillates at RF frequencies and the exact motion of charged particles in presence of magnetic field is very difficult to describe. Nevertheless, the qualitative explanation can be as follows:

The electrons are trapped in magnetic field lines and gyrate around it. The electron gyration radius is of the order of 1-3 mm[58] and is much lower than the dimensions of the chamber. This radius is smaller where magnetic field density is higher. Electrons also travel along the magnetic field line and the resultant path is helical. Due to negative potential of the walls and electrodes with respect to the plasma potential and gradient in the magnetic field, the electrons are reflected back and forth between points where the lines enter and leave the wall surface (referred as the "mirror effect"). Electrons experience drift due to Lorentzian forces. Electrons also jump from one magnetic field line to the next as they collide with the neutral gas molecules. At higher pressures, these kind of collisions dominate and magnetic field has little or no

effect on electron confinement. However, at low pressures, the electrons are trapped in the magnetic field, and thereby their path-length and lifetime in the system are greatly increased. In an efficient electron trap, the electron loss to the walls is minimized and the electrons that reach the wall should be incapable of ionizing, i.e. their energy should be degraded below the ionization threshold energy of the neutral gas.

The ions also meet the same forces, but due to their greater mass and slower speed, their motion is quite different than that of electrons. Due to their greater mass, ions have much larger Larmor radius than that of electrons and confinement of ions in magnetic field is poor.

In summary, utilization of a proper magnetic confinement scheme can result in enhanced ionization and dissociation efficiency of the plasma source at low pressures.

4.2 Existing Approaches for Magnetic Enhancement

One of the most common approach for magnetic enhancement is the magnetron. Magnetron sources are widely used in sputtering and a number of publications outline the geometry of various magnetron schemes.[59],[60] A comprehensive review of this subject is given by Vossen and Kern.[61] Arrangements similar to those used for magnetron sputtering have also been widely used for etching applications. In a magnetron based etcher, a highly uniform magnetic field and planner electrodes are essential for achieving acceptable etch-uniformity. Figure 24 shows one of the most common magnetron configuration, the planar magnetron, in which a static magnetic field is applied parallel to the electrode to create an intense plasma zone.[62] A nearly parallel magnetic field can be formed over the hollow region of the magnet where the wafer is normally kept. The electric field formed by the plasma sheath is perpendicular to the magnetic field increasing the ionization efficiency near the electrode surface. The magnetic field reduces the mobility of electrons near the electrode and the induced bias

in a magnetron is generally much lower as compared with a conventional diode system for similar operating conditions. However, the configuration shown in Figure 24 in common with all magnetron based reactors suffers from poor plasma uniformity and enhanced damage at lower pressures. In order to improve magnetic field uniformity, several dynamic magnetron apparatus have been used in commercial systems.

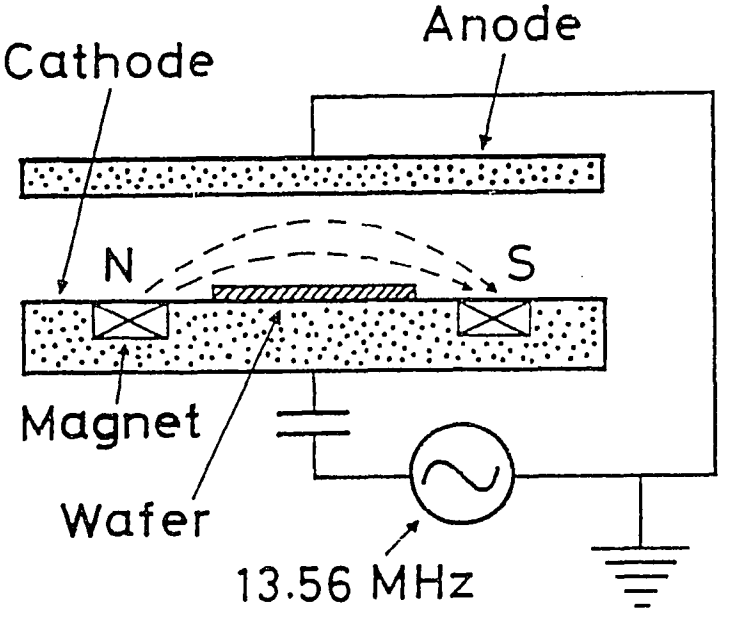

Figure 24 Schematics of a planar magnetron etching system with static magnetic field.

Figure 25 shows one of the commercially available configuration, in which, electro-magnets are used to rotate the magnetic field at 0.5 Hz parallel to the electrode surface. The magnetic field intensity can be adjusted depending upon the application. The advantage of rotating magnetic field is that it reduces the problem of non-uniform intensification of plasma associated with the static field configuration. In an another scheme, permanent magnets arranged in a racetrack-like belt are mechanically scanned over the wafer surface.[63]

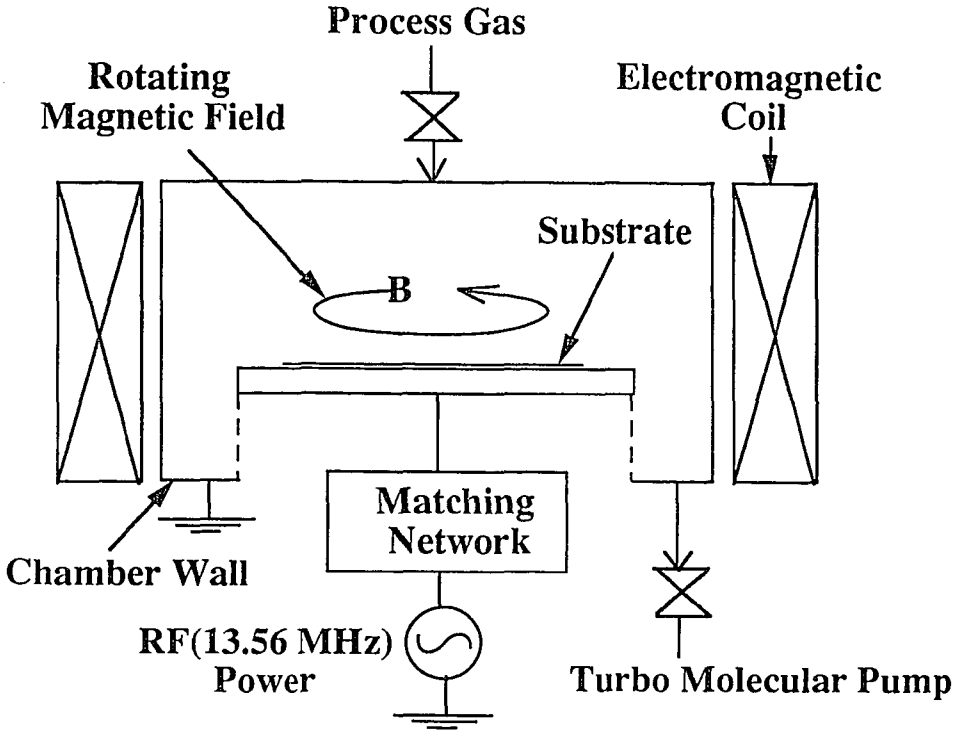

Figure 25 Schematic diagram of a commercial magnetically enhanced etching system with rotating magnetic field.

In general, magnetron schemes result in higher etch-rate and lower induced bias and can be operated at much lower pressures. Improvement in ionization efficiency and etch-rate generally depends on the applied magnetic field intensity. However, magnetron schemes generally suffer from the fact it is extremely difficult to obtain very uniform magnetic field across the wafer and substrate bias is not completely decoupled from the plasma generation. Also, local nonuniformity in plasma density near the wafer surface can result in wafer charge up and can degrade the quality of gate oxide and device performance.[64,65]

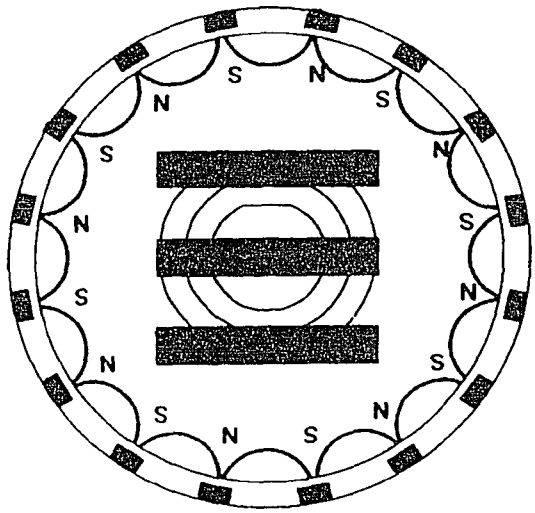

(a) Top View

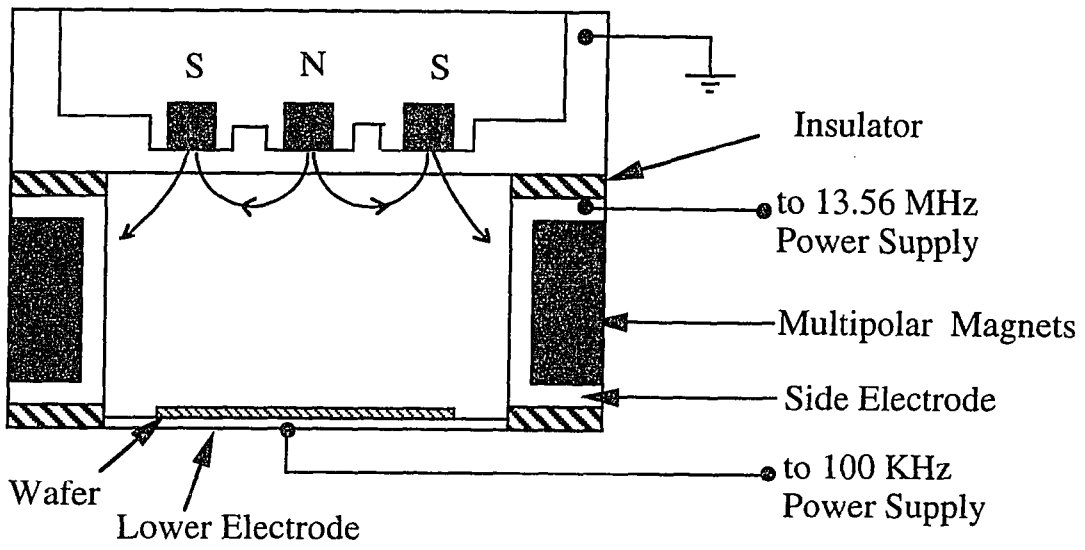

(b) Side View

Figure 26 Schematic of a commercial tri-electrode reactor with magnetic confinement.

In recent years, many new approaches have been proposed to decouple plasma generation form substrate bias while utilizing magnetic enhancement to increase etch-rates at lower pressures. These approaches are generally based on magnetic enhancement of triode configurations. One of the commercially available approach that appear in parallel with the work described in this thesis uses a dual frequency magnetically confined triode configuration and is shown in Figure 26.[66] This configuration includes two RF powered electrodes(13.56 MHz and 100 KHz) and a grounded electrode. 100 KHz power is applied to the wafer electrode and is used to control the energy of the ions incident on the wafer. The 13.56 MHz power is applied to the side wall electrode and independently controls the amount of ionization and reactive species generation. The upper electrode is grounded in this reactor geometry. Permanent magnets surrounding the chamber reduce the loss of charged particles to the reactor walls and thereby enhance the plasma density. The magnetic field is away from the wafer and does not directly influence etching at wafer surface. The major drawbacks of this configuration are that (i) it utilizes dual frequency scheme making experimental arrangement more complex; and (ii) it relies on powering magnetically enhanced side electrode for plasma generation which may result in very high sputter-rates of the electrode material contaminating the wafer.

A very recent approach utilizes a single frequency (13.56 MHz) excited, phase controlled, triode configuration (dubbed as supermagnetron) with mechanically rotating permanent annular magnets to generate magnetic field parallel to the electrode surface and is shown in Figure 27.[67] This approach represents complex experimental arrangement and also suffers from the non-uniform etching and high substrate damage due to intense magnetic field near the wafer surface.

Recently, the use of electron cyclotron resonance based microwave sources[68], helicon resonator sources[69] and inductively coupled plasma sources[70] for producing low

pressure, high density plasma is becoming more popular. All of these sources supply energy to electrons via magnetic field coupling and can produce very dense plasma at low pressures. However, since the uniformity and directionality of charged particles near the wafer surface are strongly affected by the local magnetic field, these schemes have potential problems of achieving high uniformity over larger diameter substrate. Other problems associated with these sources are the inherent high-cost and non-compatibility with existing parallel-plate production etchers.

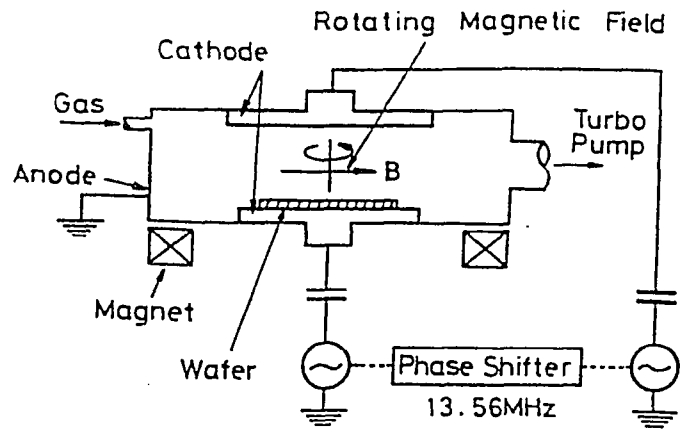

Figure 27 Schematics of supermagnetron plasma etcher.

The ideal magnetic confinement scheme should be simple and compatible with the existing parallel plate etching tools. The preferred configuration should have all the attributes of magnetic enhancement, namely: low pressure operation, high plasma density, low substrate bias voltage, very low magnetic field near the wafer surface and decoupling of plasma generation (reactive species concentration) from the substrate bias (ion bombardment energy). The next section describes a novel reactor configuration which has all of the above mentioned merits. The operation of this reactor is compared with conventional triode configuration and statistically-designed etch experiments were performed to characterize the performance of this reactor.

4.3 New Magnetic Multipole Enhanced Triode Reactor

The overall objective of this work has been to develop a parallel-plate magnetically-enhanced low-pressure reactor configuration that is suitable for use as a possible next generation of single wafer etchers. By decoupling the plasma generation from the substrate bias, better control of the photolithographically transferred pattern and low damage is possible. At the same time the reactor should possess the simplicity of parallel plate diode type etching tools and produce a very high degree of plasma uniformity across an 8" diameter working area.

We have achieved the above stated objectives by the addition of a simple inexpensive magnetic multipole to the parallel-plate triode, resulting in a magnetic enhanced etch reactor configuration, that has impressive low pressure characteristics.[71] The multipole electrode which is in the form of a cylindrical multipolar bucket, open at both ends, is added to the triode being employed as a plasma etching system. The multipole, in effect, becomes an extension of the ground shield surrounding either electrode. The resulting electrode configuration produces an extremely uniform, dense plasma at pressures as low as 2-3 x 10^{-4} Torr. The effect of the magnetic enhancement (electron containment, uniformity profile modification and low substrate bias) is particularly pronounced at lower pressures. Significant improvement over existing triode schemes is obtained using the grounded cylindrical multipolar bucket as an extension of the ground shield of the driven electrode (not the substrate electrode). This system is considerably simpler than dual frequency driven tri-electrode systems; since, it uses 13.56 MHz excitation of both electrodes. As the multipolar bucket is at ground potential, the possibility of wall material sputtering is greatly reduced.

4.3.1 Experimental Set-up

The magnetic multipole reactor is constructed by attaching an open-ended cylindrical multipolar "bucket" to the grounded plasma shield of the upper electrode of the conventional triode reactor. The overall schematic diagram of the resultant configuration is shown in Figure 28. The reactor has two RF powered electrodes with chamber and multipolar bucket walls acting as the grounded third electrode. The electrical phase of one electrode relative to the other at the operating frequency of 13.56 MHz is adjusted to 180°. The distance between the top and bottom electrodes is adjusted to 2.6 inches for the experiments. The reactor is also equipped with a laser interferometer for *in situ* etch-rate measurements.

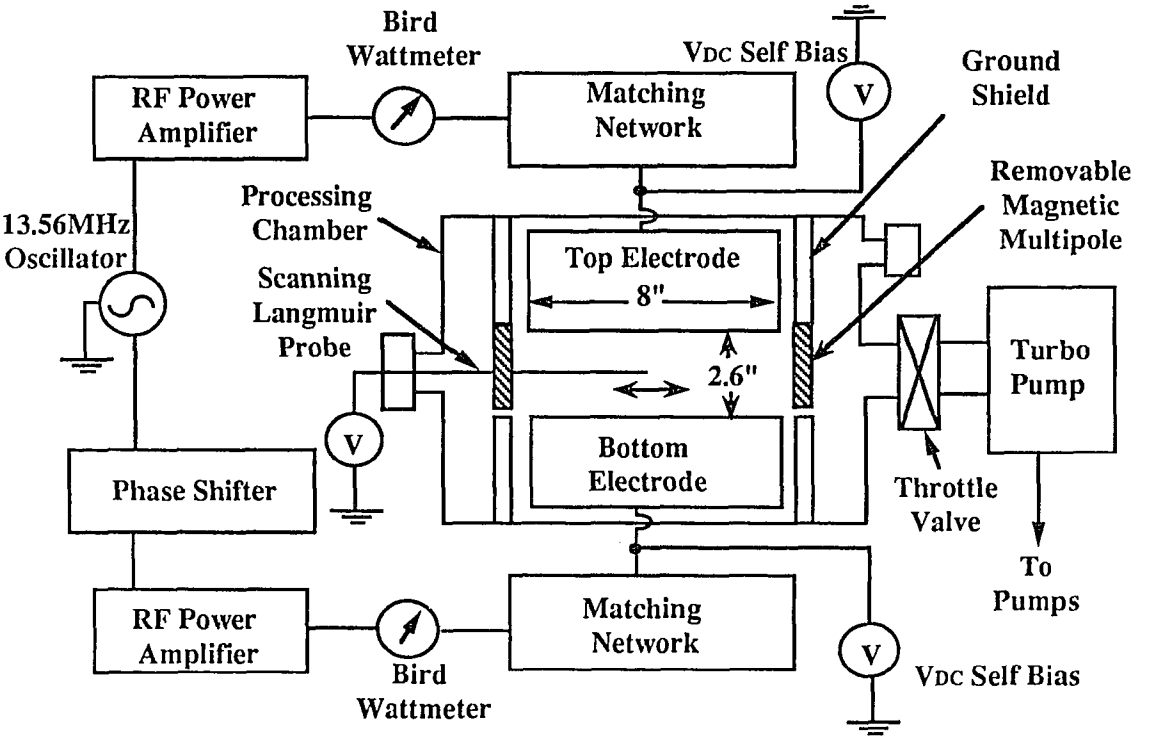

Figure 28 A schematic diagram of the test-stand consisting electrical block diagram of the power supplies and connection to each electrode.

4.3.2 Description of Magnetic Multipolar Bucket

The bucket, shown in Figure 29(a), is constructed using ceramic permanent magnets arranged on its outer surface to produce a multipolar "minimum-B field" or "picket fence" magnetic field profile. The cusp length, spacing, etc. are exactly the same as that used in high intensity ion sources for neutral injection in fusion reactors.[72],[73] These multipolar devices are characterized by a relatively field-free region in the center and a high intensity field that "shields" the walls. Effectively, the peripheral multipolar field causes magnetic confinement of the plasma electrons and provides a more efficient gas ionization process at low pressures. Typical field measurements are shown in Figure 29(b) for reference. For the multipole device used, the magnetic flux density falls off towards the center of the device. The .01 Tesla contour is located ~2.5 cm from the wall. Typically, 4" diameter wafers are used in the etching experiments and are thus located in a relatively magnetic field-free plasma region. Most of the high density plasma is confined to the walls of the multipole and near the top powered electrode of the triode reactor. To achieve uniform gas distribution, the gas injection is made an integral part of the multipole bucket. The multipolar bucket can shield the plasma from the walls to reduce the losses of fast electrons. The fields are in a multi-cusp arrangement created by heaving rows of permanent magnets with an alternating polarity. Measurements of this kind of confinement in ion sources proved that the main effect is the improved confinement of the fast electrons which may bounce some 75 times with the magnetic wall before being lost to the material wall.[74] The resulting long life time leads to a good ionization efficiency which permits operation at lower pressures. The cusp fields also lead to much improved plasma homogeneity.

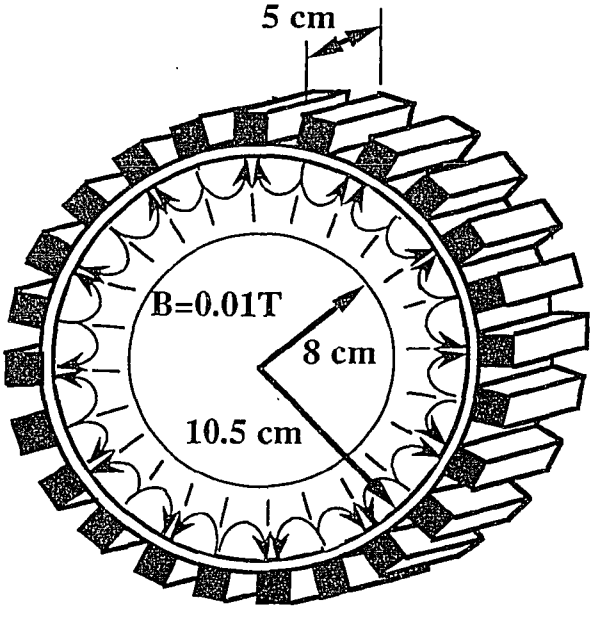

(a)

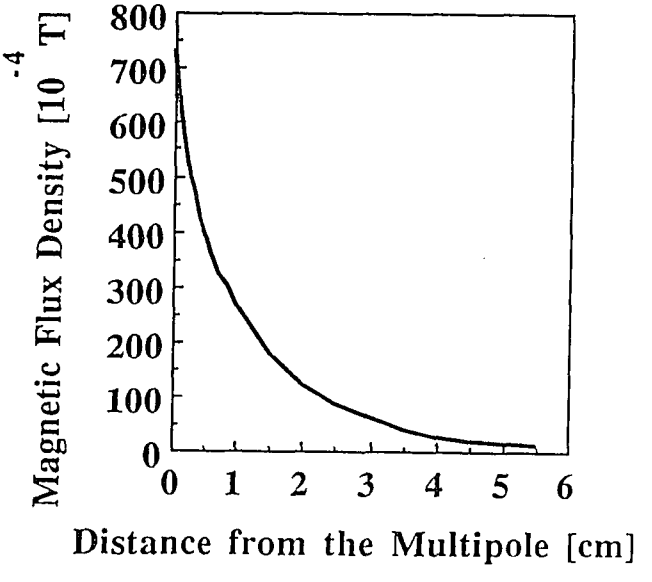

(b)

Figure 29 (a) Multipolar magnetic bucket (b) radial field characteristics of the multipole plasma confinement system.

4.4 Experimental Results for Multipole Enhanced Reactor

4.4.1 Comparison With Triode Configuration

To determine the relative plasma density and uniformity, the scanning Langmuir probe is placed mid-way between the electrodes (1.3 inches separation from each electrode) and is centered on the 8 inch diameter of the electrodes. It is biased at -50V to ground to measure the saturated ion current produced in Ar plasma by this configuration. The performance of the triode without the multipole as determined by the pressure dependence of the saturated ion current and the induced bias on the powered electrode is shown in Figure 30(a). The power to each electrode is set at 200 watts/electrode to produce argon plasma at 10 sccm flow. With decreasing pressure the saturation ion current decreases considerably. It decreases by more than an order of magnitude when pressure is lowered from 80 mTorr to 5 mTorr. The induced bias increases from about -480V to over -800V for the same pressure change. At pressures below 5 mTorr, these changes are even more pronounced. At 1 to 2 mTorr in the triode configuration, it is difficult to sustain the plasma. Figure 30(b) shows the induced DC bias and saturated ion current as a function of gas pressure of the triode reactor with the multipole installed under precisely the same operating conditions. Initially the saturation ion current decreases with decreasing pressure from 80 to around 30 mTorr. The decrease is comparable with the triode configuration. Below 30 mTorr; however, the decrease in saturation ion current levels off at 360 arbitrary units(A.U.) and remains nearly constant over the range from 30 mTorr to pressures as low as $2\text{-}3\text{x}10^{-4}$ Torr. The induced bias level rises from about -380V at 80 mTorr to a peak level of around -460V at 30 mTorr. On further decreasing of reactor pressure from 30 mTorr, the induced bias begins to drop and continues to decrease reaching a value of about -330V at $5\text{x}10^{-4}$ Torr.

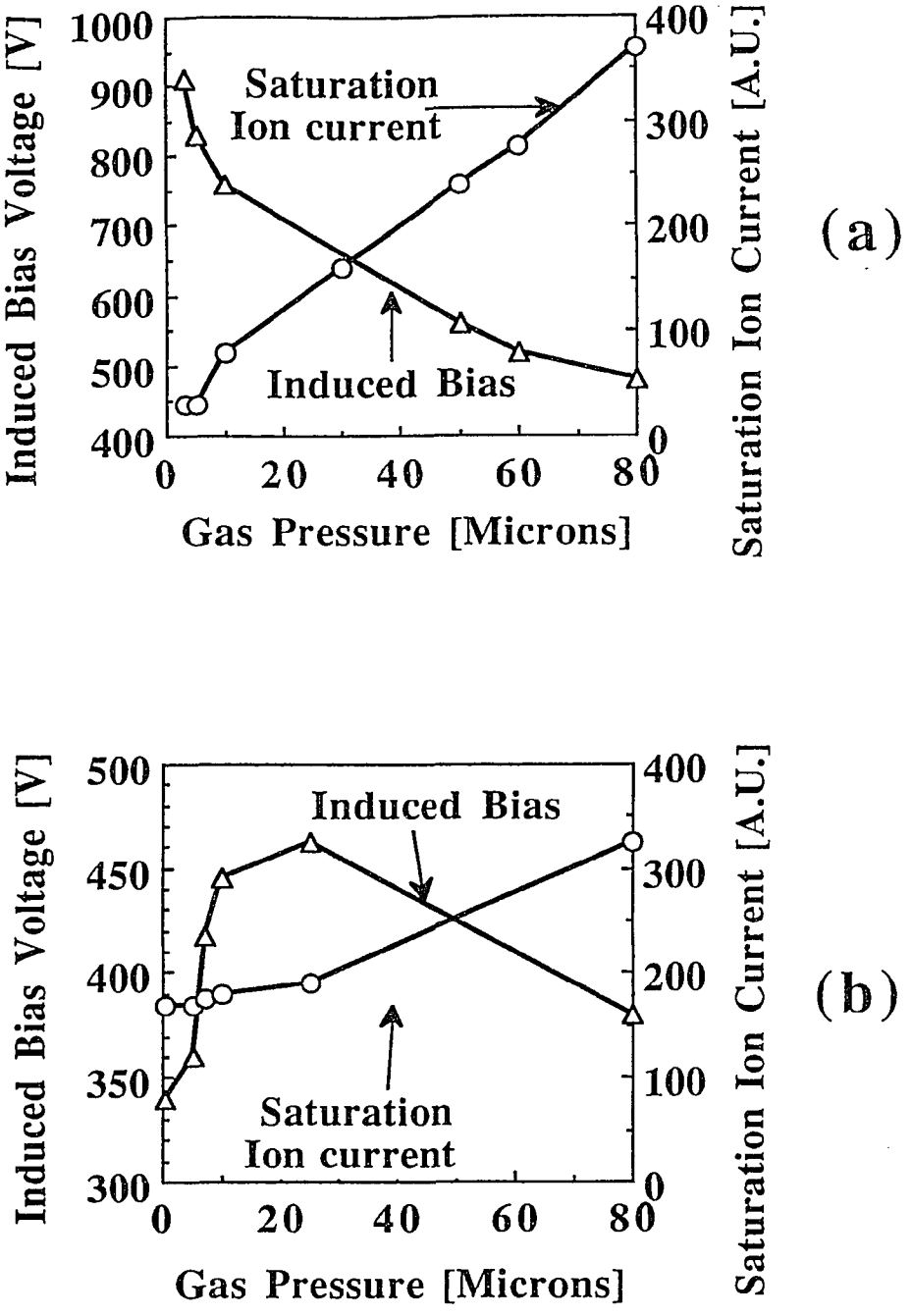

Figure 30 Saturated ion current and DC bias on the lower electrode as a function of argon pressure (a) triode configuration (b) multipole enhanced triode configuration.

The radial uniformity of the plasma is determined by measuring saturated current density using the Langmuir probe with argon pressure as a parameter. Figure 31 compares the plasma uniformity obtained by the biased Langmuir probe, scanned radially, parallel to the electrodes, for the triode and multipole-enhanced triode configurations. Figure 31(a) shows the effect of pressure variation on the plasma uniformity profile for a relatively high pressure regime($\geq$10 mTorr). The density appears to peak at about 1 to 2 cm from the multipole wall and becomes very uniform in the central electrode region for the multipole enhanced triode reactor configuration. The triode configured system shows significantly lower saturated ion current in the central region between the electrodes as compared with the multipole enhanced triode reactor configuration. Below 30 mTorr, the triode configured reactor shows a very non-uniform plasma density distribution that drops off roughly parabolic with distance from the center of the electrode. Figure 31(b) compares the saturated ion current uniformity without and with the multipole enhancement in a relatively low pressure discharge($\leq$ 3 mTorr). At 3 mTorr, the plasma density is extremely low for the simple triode configuration. At pressures below ~3 mTorr, it is difficult to keep the plasma excited without the multipole. As shown in Figure 31(b) the saturated ion current distribution using the multipole is more uniform than the simple triode configuration. At pressures around 1 mTorr and less, the density shows a parabolic type fall off toward the wall and a uniform central region for the multipole configuration. From the results shown in Figures 30 and 31, it appears that the magnetic field configuration of the multiple becomes increasingly effective with decreasing pressure. Plasma confinement and enhanced ionization accounts for the enhanced low pressure performance of the multipole-enhanced triode reactor. At pressures below 30 mTorr, magnetic confinement becomes effective in plasma and the induced bias decreases with decreasing pressure to maintain a constant power dissipation due to decreased neutral collisions in the plasma.

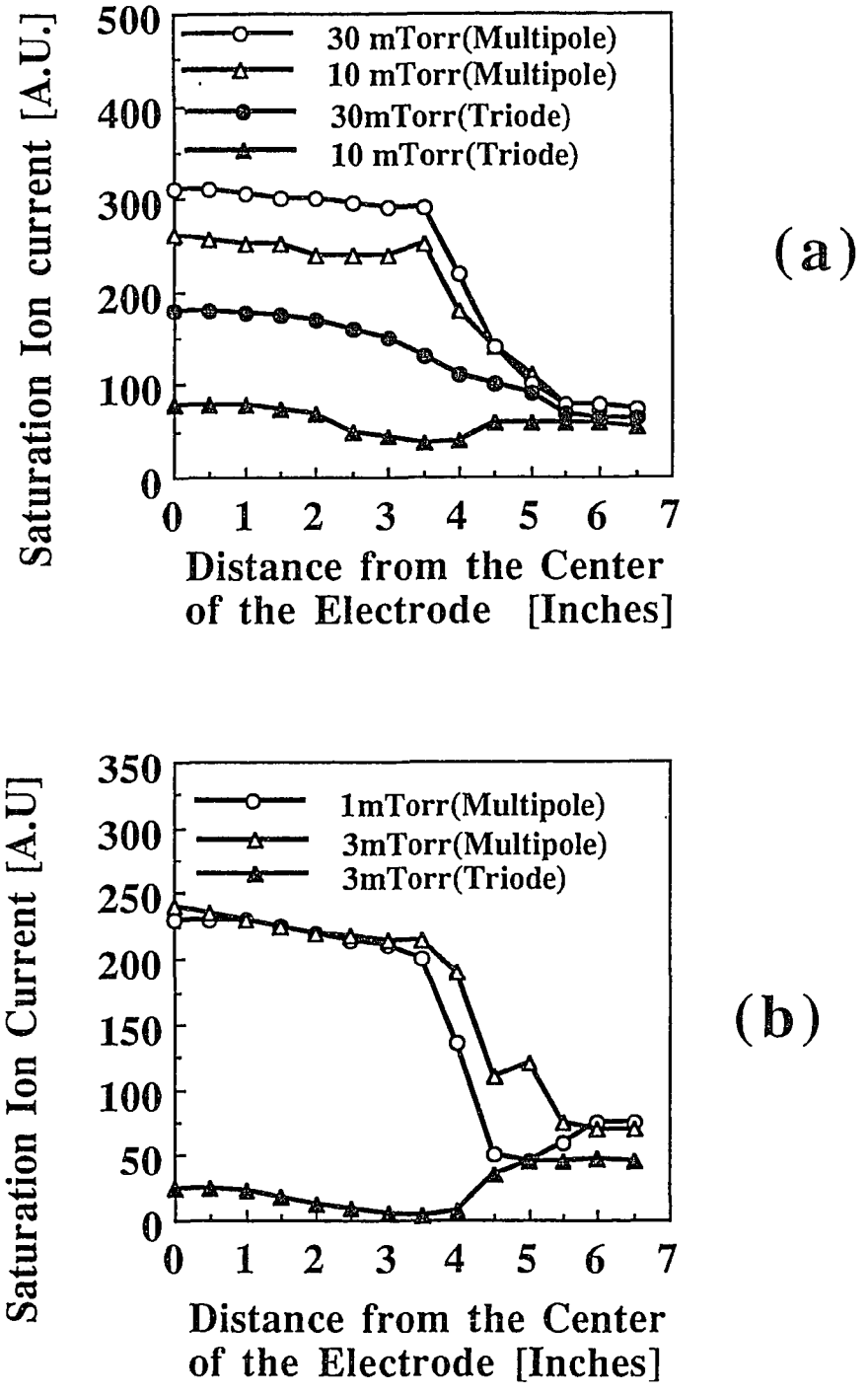

Figure 31 Plasma uniformity scans performed in argon using a Langmuir probe for the pressure ranges of (a) 10-30 mTorr and (b)1-3 mTorr.

The uniform plasma density profile at low pressures indicates that magnetic enhanced benefits can be obtained in simple geometry parallel plate reactor without compromising plasma uniformity.

The induced bias mapping of the magnetic multipole reactor in Cl_2 plasma is shown in Figure 32 for two different pressures. Inspection of Figure 32 shows that for a wide range of upper and lower power variation (0-400W), the induced bias on the lower electrode is nearly independent of the power applied to the upper electrode for both high pressure(100 mTorr as shown in Figure 32(a)) and low pressure (1 mTorr as shown in Figure 32(b)) discharge. Thus, in the multipole enhanced triode reactor, plasma generation is efficiently decoupled from the substrate bias and the intense plasma can be generated at lower pressure by applying high power to the upper electrode while the bias on the lower electrode can be independently controlled to obtain desired anisotropy and to minimize damage from energetic ion bombardment.

4.4.2 Polysilicon Etching in Multipole Reactor

Plasma processes are often developed by varying one factor (process variable) at a time while holding all other factors at same constant level. While this approach does not require a statistical design, it is expensive and can yield incomplete and often misleading results. This type of experimentation requires testing at many factor levels, does not account for experimental errors and ignores interactions among the process variables. For example, the etching rate typically increases with power, but the rate of increase depends upon the pressure, the composition of feed gas and the total wafer area.

The use of statistical methods for experimental design and analysis permits the efficient characterization and optimization of any number of process responses, e.g. etching rate and selectivity, as a function of process settings. This approach manipulates and optimizes the process efficiently with a minimum amount of experimentation. The use of this approach is very useful for plasma etch process optimization; since, it is

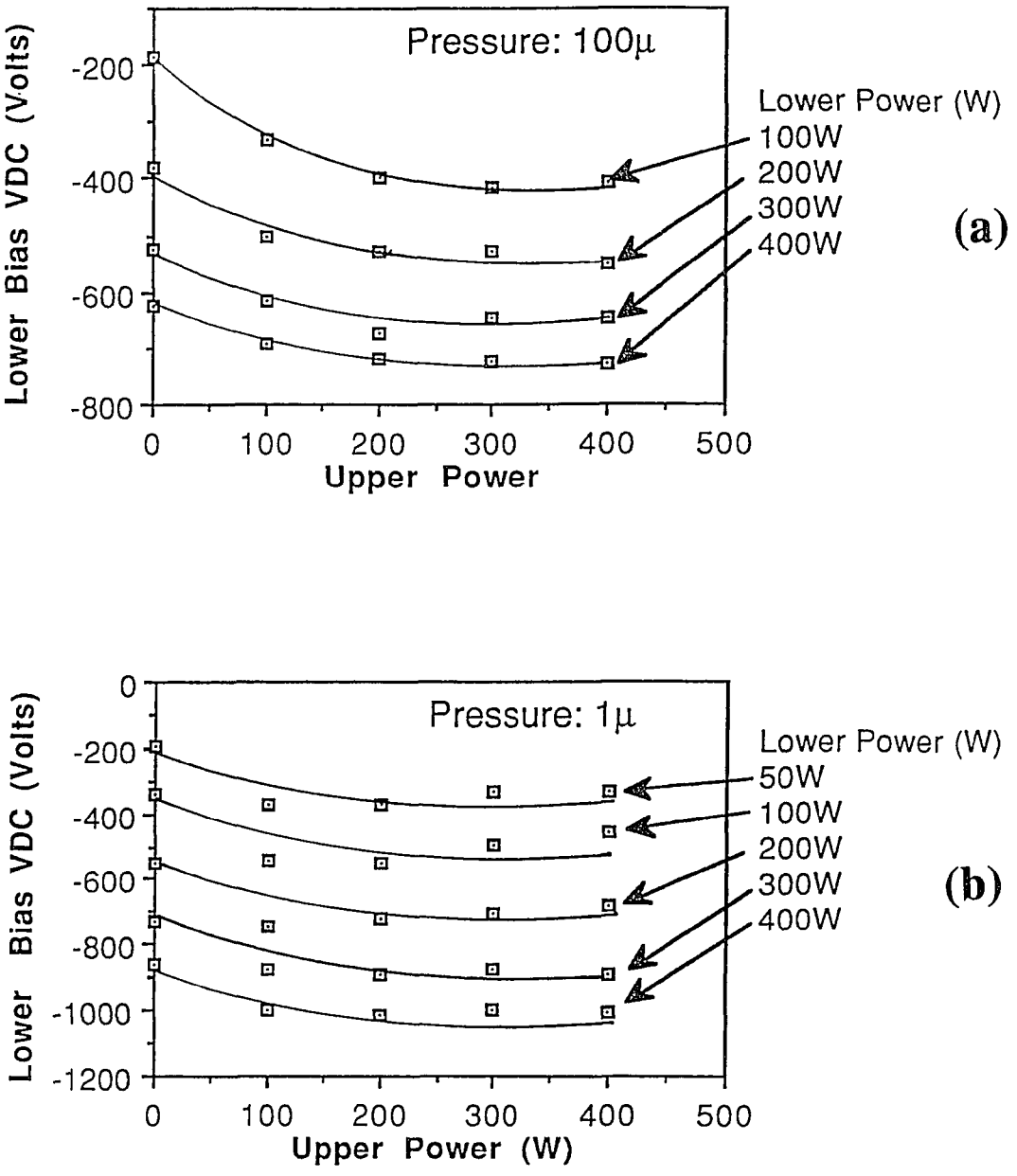

Figure 32 The induced bias variation as a function of upper and lower power (0-400W) in Cl_2 plasma at 100 mTorr in (a) and 1 mTorr in (b).

presently not possible to model plasma processes from a fundamental approach.

Response Surface methodology is a statistical technique by which the experimental strategy and data analysis are combined efficiently to generate a parametric model that represents the process response.[75] Once the response has been modeled, graphical representations of the response surfaces formed in the parameter space (e.g., contour plots) can be generated for use in process optimization.

Extra care should be taken in defining parameter range when applying to a process since the empirical model is a polynomial which can not be used for prediction outside the region explored experimentally. Only a correct theoretical model can be used for extrapolation.

The low pressure etch performance of the multipole reactor was characterized using response surface methodology.[76] A commercially available RS-1 software package was used to design and analyze statistical experiments. A Face Centered Cube (FCC) design model for three process variables was used for the study. Figure 33 shows the geometric representation of an experimental design based FCC model with center point replication.

The factor level coding of -1, 0 and 1 designate the lower, middle and upper levels of the variables, respectively. The design replicates the center to aid in the quality of prediction and have a minimum five degrees of freedom to estimate residual error.

Pressure, upper power and lower power were selected as the input variables. Cl_2 is a commonly used gas for polysilicon gate etching and was used for polysilicon etch characterization of the reactor. Induced lower electrode bias, polysilicon etch rate, and selectivity of polysilicon to oxide etching were selected as the outputs of the model. A quadratic model was used to determine the response of output parameters as a function of input variables. Since the objective of the experiment was to obtain low pressure, anisotropic, high-rate etching with minimal damage, the ranges for pressure,

upper power and lower power were selected 0.5 to 30 mTorr, 500 to 1300 W and 10 to 100 W, respectively. Wafers were etched by just placing them on the water cooled-lower electrode.

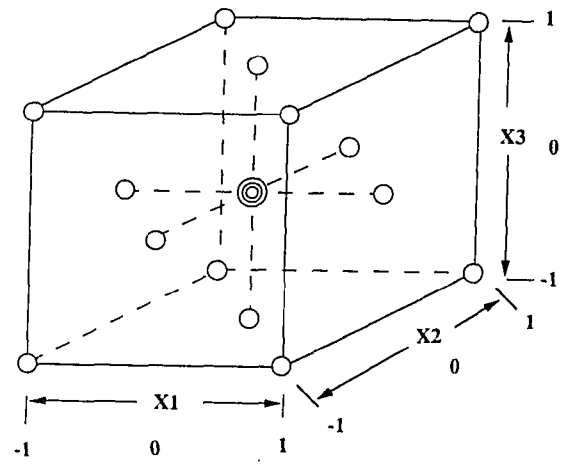

Figure 33 Geometric representation of an experimental design based FCC model with center point replication.

Figure 34 shows the upper and lower bias dependence on lower and upper power for 15 mTorr pressure. It is evident from the figure that the lower bias strongly depends on the lower power and is only weakly dependent on upper power at this pressure. Good decoupling of substrate bias from the plasma generation is obtained.

The pressure and lower power dependence of polysilicon etch-rate and selectivity are shown in Figure 35 for the case of a high upper power (1300 W) condition. For a constant lower power, the etch-rate and selectivity increase with pressure. For a constant pressure, the etch-rate increases with lower power but the selectivity decreases at the same time. A selectivity of 15 with etch-rates in the range of 4000 Å/min can be obtained for 100W lower power and 30 mTorr condition. By decreasing the lower power at 30 mTorr, selectivity as high as 50 can be achieved with etch-rates in the range of 2000Å/min.

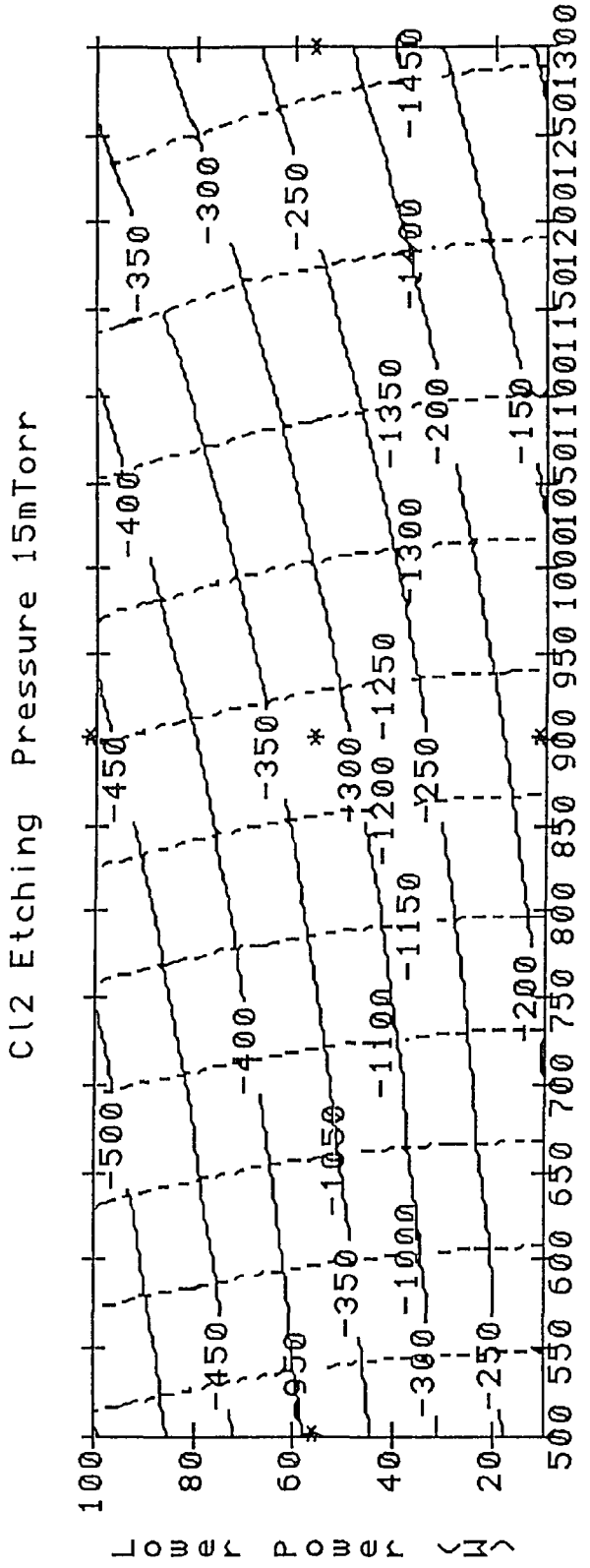

Figure 34 RS-1 results for Cl_2 etching of polysilicon: upper and lower power dependence on lower and upper power.

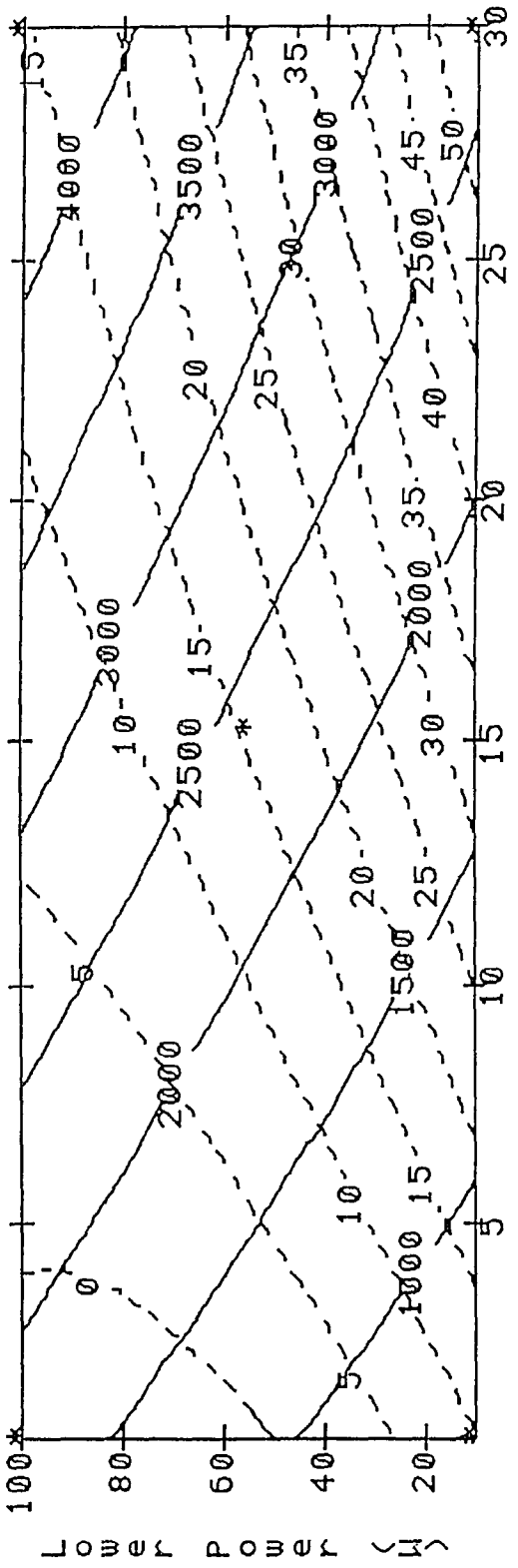

Figure 35 RS-1 results for Cl_2 etching of polysilicon: pressure and lower power dependence of polysilicon etch-rate and selectivity.

The pressure and upper power dependence of etch-rate and selectivity are shown in Figure 36 for constant lower power (55W) condition. As can be seen from the figure, etch-rate and selectivity increases with pressure for constant upper power. However, the increase is less rapid after a critical pressure, which depends on the upper power.

The lower and upper power dependence of the etch-rate and selectivity are shown in Figure 37. As can be seen from the figure, the etch-rates are strongly dependent on the lower power and increases with low power. However, selectivity decreases with increasing lower power. Both etch-rate and selectivity increase with upper power for a fixed low power condition. Therefore, to get high etch-rates with good selectivity, the etching should be performed with a high upper power and low lower power condition.

Figure 38 show the scanning electron microscope image of etch profiles for a 15 mTorr, 1.3 KW upper power and 55W lower power etching condition. As can be seen from the figure, very good anisotropy for this condition is obtained with a moderate etch-rate(2200Å/min) and good selectivity(20). Etch-rates can be increased by increasing lower power and pressure.

Figure 39 shows the etch-profiles obtained for 30 mTorr, 100W lower power and 1.3 KW upper power condition. Etch-rate of 4850Å/min are obtained with a selectivity of 15. However the photoresist starts to degrade and the etch-profiles become less anisotropic. The reduced anisotropy is due to the increase in pressure since scattering of ion directionality is more likely at higher pressure. Temperature of wafer is also expected to be higher for this condition since the etch-rate and lower power is higher than the previous condition. It should be noted that good anisotropy, high selectivity with reasonable etch-rates are obtained for uncooled and unclamped wafers without the need for He back-side cooling.

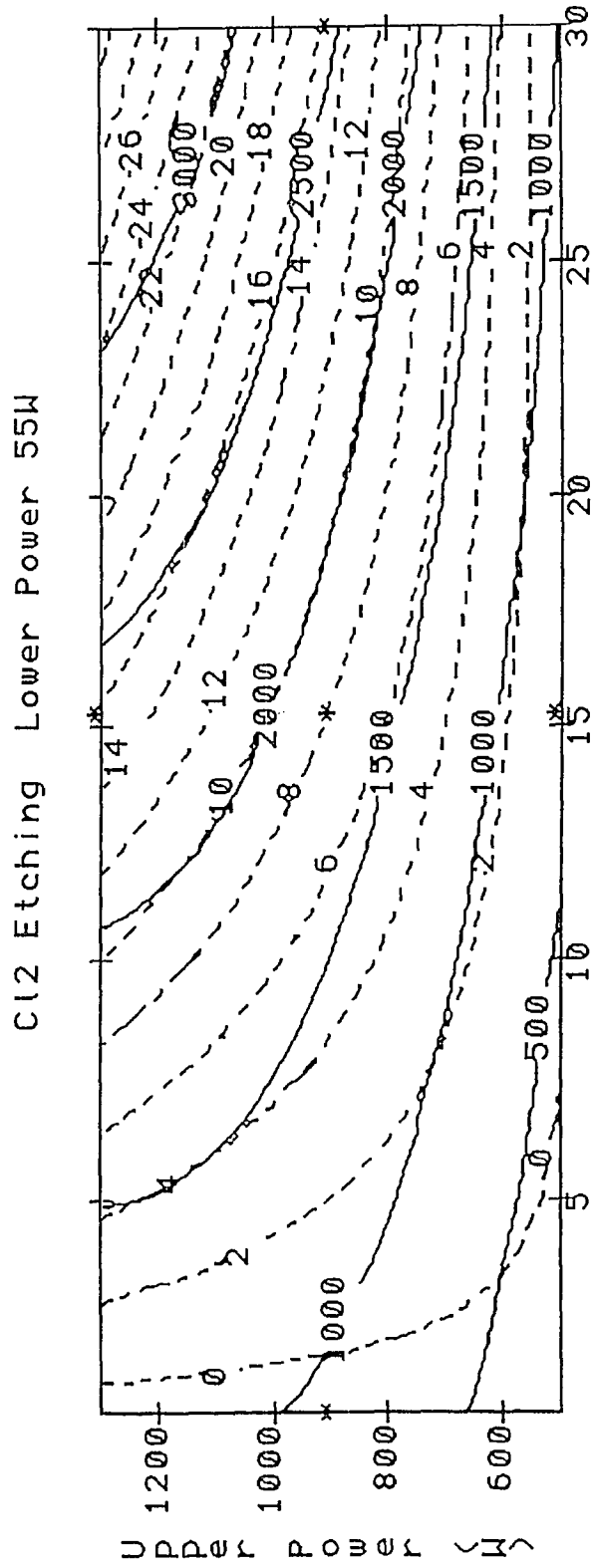

Figure 36 RS-1 results for Cl_2 etching of polysilicon: pressure and upper power dependence of etch-rate and selectivity.

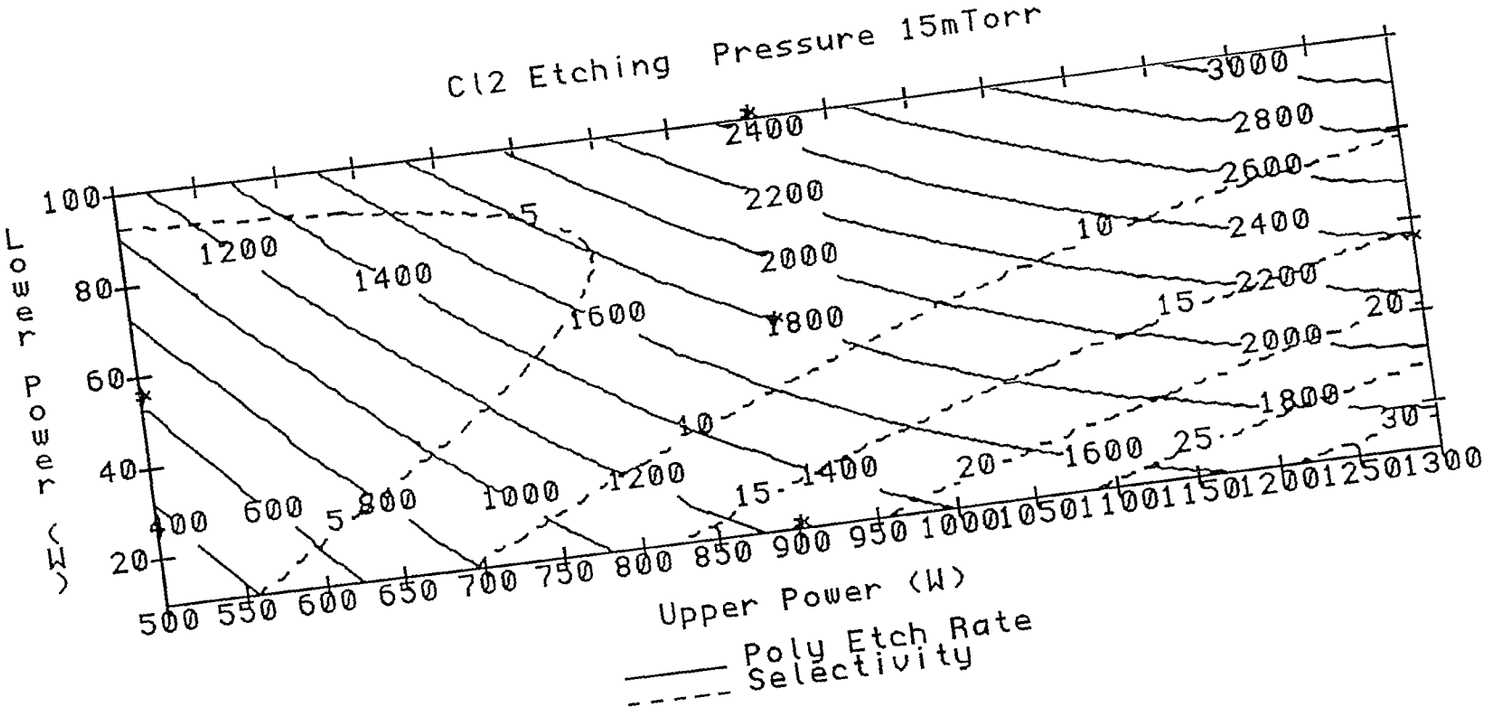

Figure 37 RS-1 results for Cl_2 etching of polysilicon: lower and upper power dependence of etch-rate and selectivity.

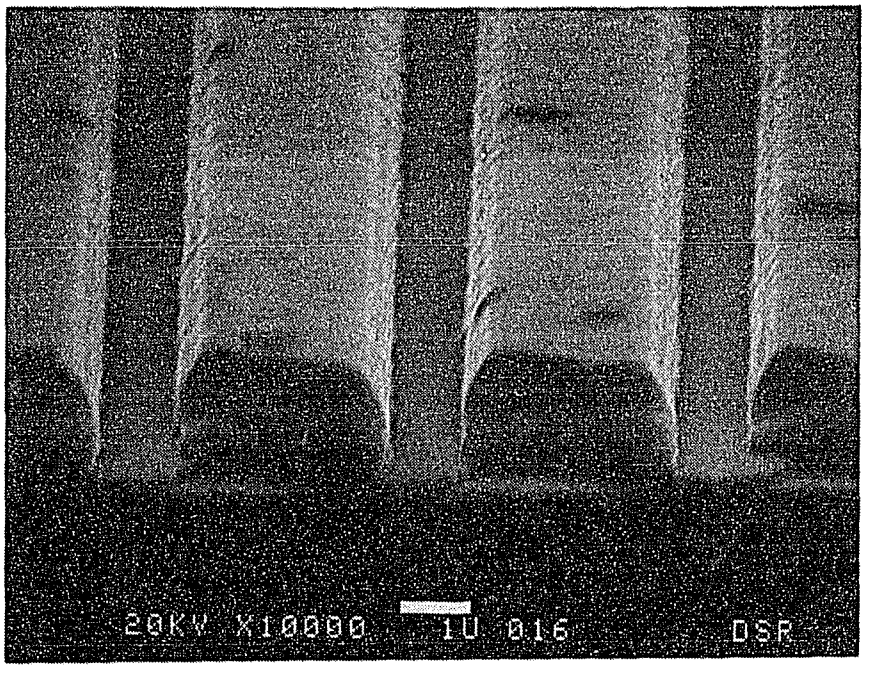

Figure 38 SEM photograph of an etched profile for 15 mTorr, 55W lower power and 1.3 KW upper power condition.

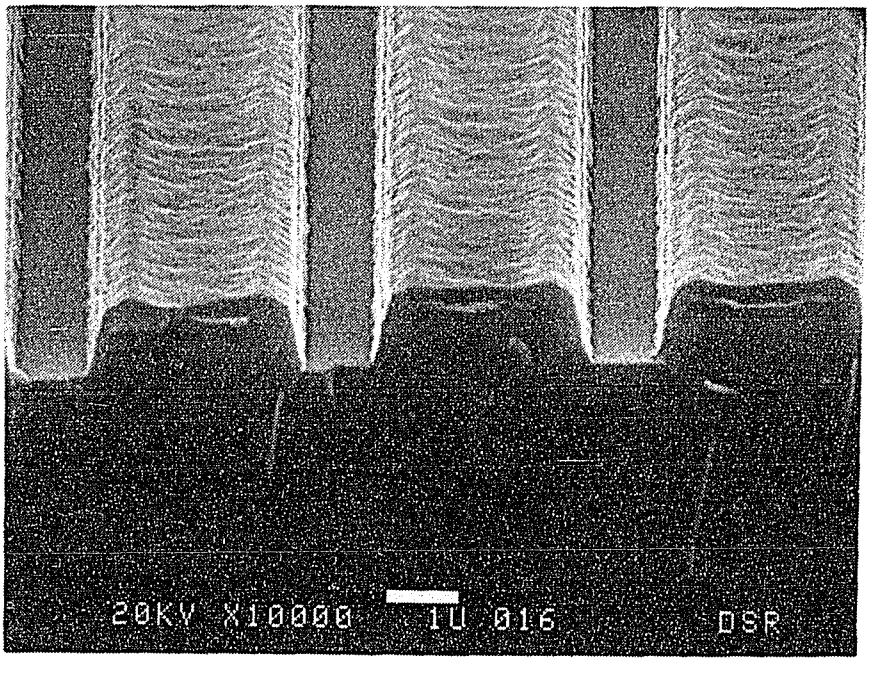

Figure 39 SEM photograph of an etched profile for 30 mTorr, 100W lower power and 1.3 KW upper power condition.

The surfaces of the oxide layer after the polysilicon is removed by plasma etching were also studied using X-ray Photoemission Spectroscopy (XPS). For very low lower power(10W) and high upper power (1000-1300W) conditions, significant amount of Fe was found on the oxide surfaces. However, for Fe residue levels were below the detection capability of XPS for all other conditions. These preliminary XPS results suggest that significant amount of sputtered material from upper electrode can deposit on the wafer when very low power is applied to the lower electrode. Replacement of the stain-less steel upper electrode with anodized aluminum electrode should reduce the wafer contamination since the sputtering yield for anodized Al is lower than satin-less steel.

4.5 Summary

A simple grounded magnetic multipole device can be added to a diode or triode reactor configuration while maintaining all the advantages of magnetic enhancement and diode simplicity to produce a high quality plasma etching tool. Very good decoupling between plasma generation and substrate bias is obtained in the multipole enhance triode reactor configuration. Good anisotropy, high selectivity with comparable etch-rates were obtained at pressures below 30 mTorr for polysilicon etching using Cl_2 chemistry.

CHAPTER 5

A NEW PLASMA ETCHING DIAGNOSTIC TOOL BASED ON THERMAL IMAGING OF WAFER

Requirement for larger wafers and thinner oxides for modern high-density high-yield high-throughput integrated circuit manufacturing is putting stringent demands for rapid optimization of an etch-process and for process monitoring and control. The ultimate goal for the design of an etch tool is to translate the etch requirements into proper settings of externally controllable tool parameters and then proceed to etch with closed loop control. However, there are only a limited number of plasma and wafer diagnostics which are suitable for the production environment. This makes it difficult to monitor and control the process in real time. Thus, development of a diagnostic tool capable of monitoring and controlling an etch-process in real-time as well as providing elucidation of some basic plasma processes will have an enormous value. This chapter describes a novel diagnostic tool which has a potential of meeting requirements of modern production reactors.

A new diagnostic tool based on thermal imaging of wafers using a high resolution infrared camera has been developed as part of this thesis and is described in this chapter. It has been demonstrated that this technique can be useful for end-point detection and *in situ* monitoring of etching uniformity on production-type etching tools.[77] This technique is also useful for inferring wafer temperature and heat transfer characteristics[78,79] which can be an additional aid for developing basic understanding of some of the physical and chemical processes that will in turn lead to process and reactor optimization.

In this chapter, basic theory of radiometric measurement is described first followed by the experimental development of this technique. The usefulness of this

technique along with theoretical and experimental results is described into three areas: spatial end-point detection and in *situ* determination of uniformity of etching, wafer temperature measurements and heat transfer analysis. Discussion on each of these areas is accompanied with an introduction and the technological importance of the results.

5.1 Basic Theory of Radiometric Measurements

Detailed mathematical modeling of various radiometric techniques has been reviewed by M. Kaplinsky and others.[80,81] A brief summary of important radiometric relations used in broad-band radiometry is presented here.

In radiometric temperature measurement systems, the temperature of the target is inferred from the signal intensity as measured by the photodetector viewing the radiant surface. The temperature of the target is related to the detected signal by a complex relationship involving the responsivity of the detector, spectral transmittivity of optical components and the emissive properties of the target.

The fundamental equation relating the spectral distribution of the radiating blackbody to its absolute temperature is the Plank's relation:

$$L_{\lambda,b}(\lambda,T)=\frac{C_1}{\lambda^5\left[\exp\left(\frac{C_2}{\lambda T}\right)-1\right]} \tag{16}$$

where

$L_{\lambda,b}(\lambda,T)$ - is the blackbody spectral radiance [W/m^2·μm];

T- temperature of the blackbody radiator [K];

λ-is the wavelength [μm];

C_1= 1.1911X10^8 - is the first radiation constant [W·μm^4/m·sr]; and

C_2= 1.4388X10^4 - is the second radiation constant [μm·K].

For non-blackbodies (gray or color), the spectral radiance can also be accurately obtained from the Plank relation if the spectral emissivity of the surface is known or can be measured.

The spectral radiance is invariant along a beam of radiant flux. This property enables the radiant flux to be collected by an IR detector using a suitable collection optics as shown in Figure 40.

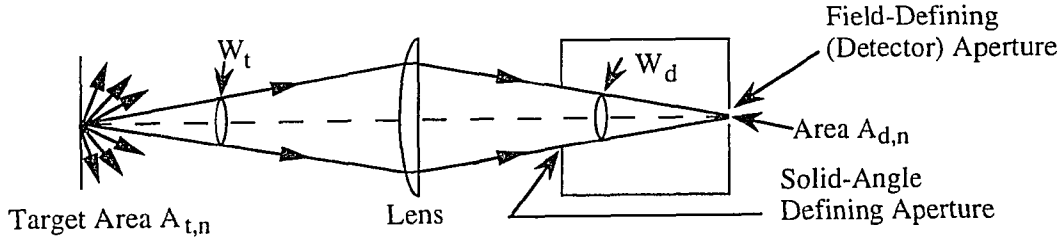

Figure 40 Radiation thermometry with lens.

The expression for the signal detected by the detector viewing the radiant target is given by:

$$S(T) = A_{d,n}.\omega_d.\frac{t_i}{Q_{el}}\int_0^{\infty}\varepsilon(\lambda,T)\tau(\lambda).R(\lambda).L\lambda,b(\lambda,T)d\lambda \qquad (17)$$

where

$S(T)$ - is the output signal of the detector in electrons;

t_i - integration time;

Q_{el} -is the charge of the electron;

$\tau(\lambda)$-is the transmittivity of the optics;

$\varepsilon(\lambda,T)$-is the emissivity of the target; and

$R(\lambda)$-is the responsivity of the detector.

Thus, for a specific radiometric system, the detected signal is strongly dependent on the spectral emissivity and temperature of the radiating surface. The temperature of the target is determined by measuring the spectral radiance in a specified spectral region and by supplying appropriate value of emissivity and characteristic parameters of the detector and the optics.

5.2 Experimental Setup

The experimental set up used for this work is shown in Figure 41. A high resolution infrared television camera is used for *in situ* monitoring of Si wafers during plasma etching. The charge-coupled-devices (CCD) based camera has a 320X 244 PtSi Schottky barrier detector array with 40X40 μm^2 pixels and is operated at 30 frames/s with 100-mm f/1.4 to f/4.0 optics[82]. It detects infrared radiation in the 1-to 5-μm spectral range and is capable of detecting noise equivalent differential temperature (NEΔT) of less than 0.1°C. The spectral responsivity of $R(\lambda)$ of the infrared imager depends on the quantum efficiency of the PtSi Schottky barrier detectors and can be approximated by the Fowler equation as:

$$R(\lambda) = C\left(1 - \frac{\Psi_{ms}\lambda}{1.24}\right)^2 \text{ in A/W} \qquad (18)$$

where

C- is the quantum efficiency coefficient in eV^{-1}; and

Ψ_{ms}– is the Schottky barrier height in eV.

The measured spectral responsivity and quantum efficiency of the PtSi SBD array corresponding to $C = 0.267 eV^{-1}$ and $\Psi_{ms} = 0.2272$ eV is shown in Figure 42.

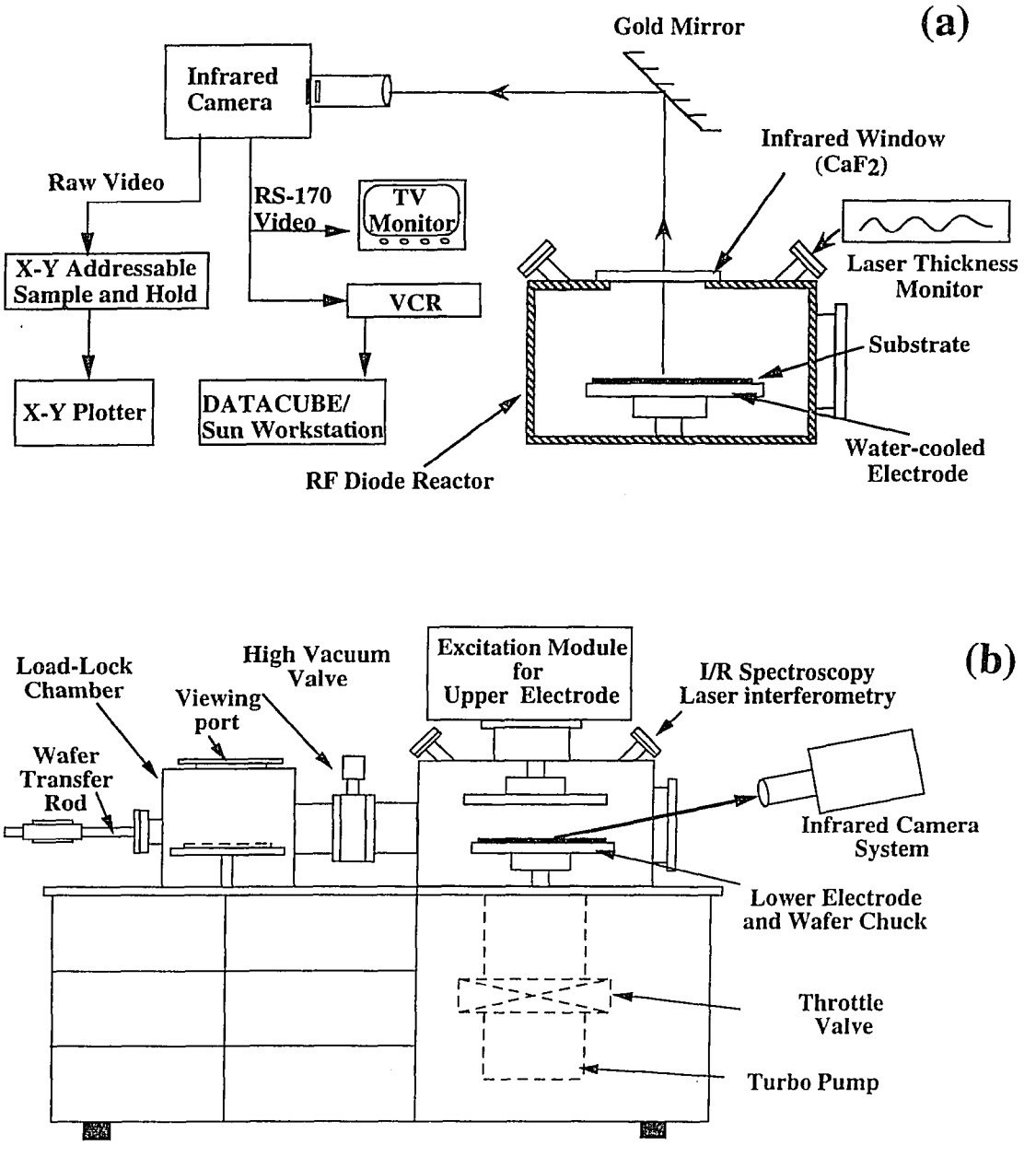

Figure 41 Experimental set-up for *in situ* wafer monitoring during plasma etching by infrared camera for the cases of (a) normal imaging of wafer in an open-ended diode reactor and (b) oblique imaging in a production-type parallel-plate diode/triode reactor.

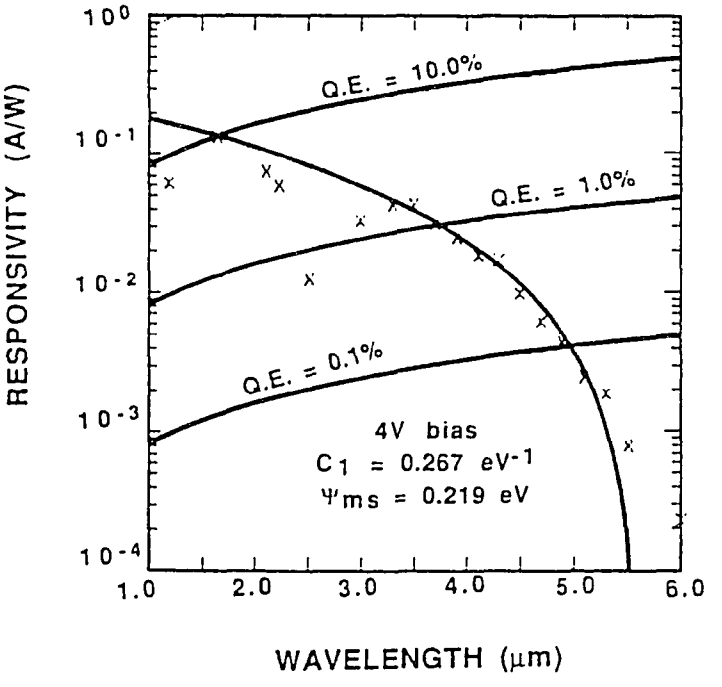

Figure 42 Measured spectral responsivity and quantum efficiency of the PtSi SBD array.

The product of the detector spectral responsivity and spectral radiant exitance of a black-body source for different temperatures assuming f/1.4 optics is shown in Figure 43. As can be seen from the figure, the detector response peaks at 4.1 μm for the radiation source at 85 °C and has an effective FWHM bandwidth of 1.5 μm. The charge handling capacity of the SBD imager is $1.2X10^6$ electrons/pixel. The infrared signal emitted from the wafer under certain plasma etching conditions was strong enough to saturate the detectors using f/1.4 optics. To circumvent this, the amount of signal reaching the detectors was controlled by varying the aperture of the lens to avoid saturation. An alternative of controlling aperture would be to control the integration time of the imager or to use narrow-band or neutral density filters.

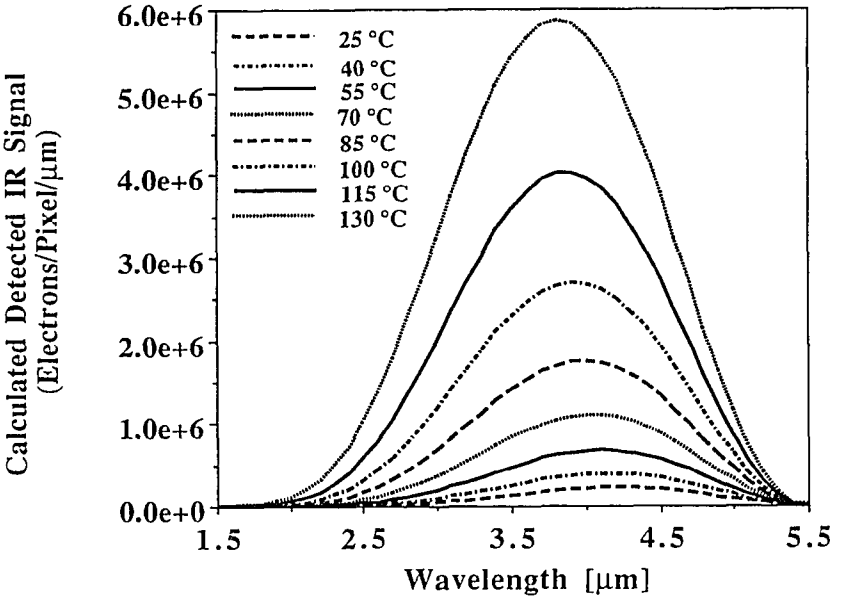

Figure 43 Product of the PtSi detector spectral responsivity and spectral radiant exitance from a blackbody source for different temperatures.

Thermal images obtained by the camera can be displayed on a TV monitor or can be stored on a VCR. A DATACUBE workstation is used to digitize the images and for subsequent signal processing. The IR camera system is calibrated so that the radiometric information can be recovered from the digitized image.

The camera system is capable of performing one-point and two-point uniformity corrections for image enhancement. However, these corrections require complex signal processing in order to recover the radiometric information. Figure 44 shows the measured response of eight pixels selected across the detector array without uniformity correction. As can be seen from the figure, the pixels across the detector array have very uniform response and uniformity correction schemes were not utilized for this work.

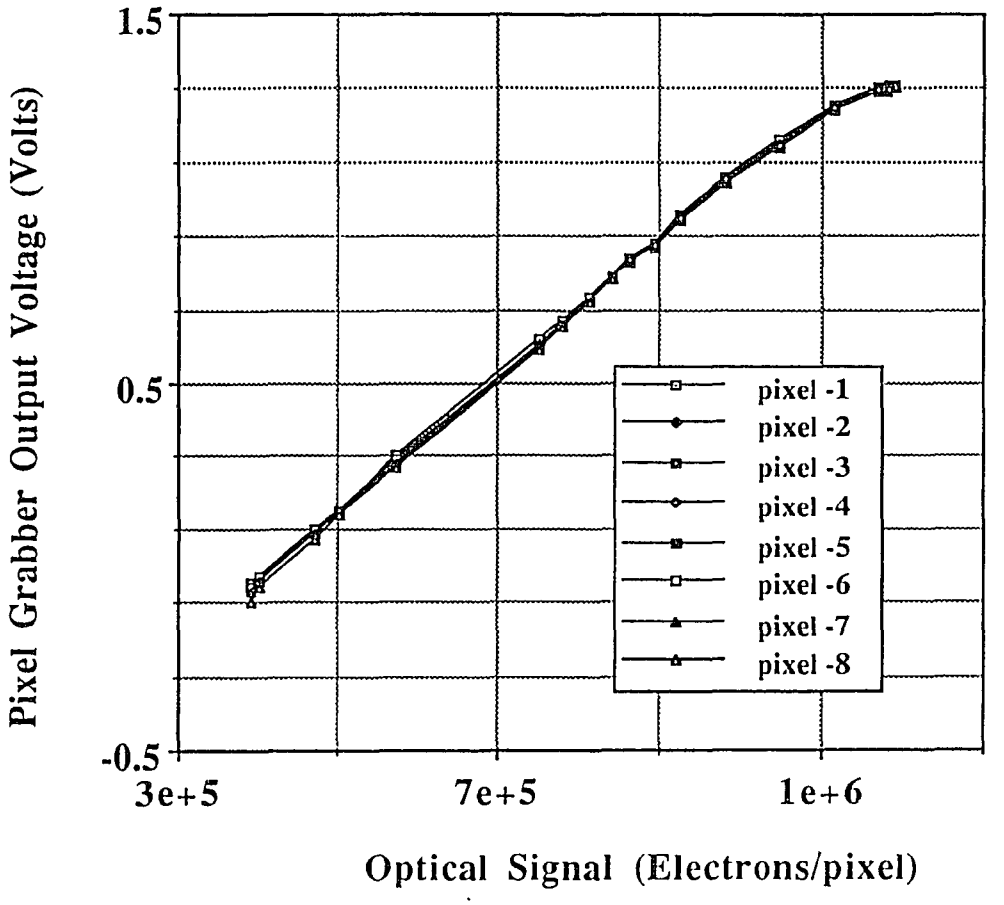

Figure 44 Measured response of eight pixels selected across the detector array under uniform imager illumination condition.

The camera system was installed on a production-compatible etching reactor which can be configured in diode or triode mode. The reactor consisted of two 8-inch stainless steel electrodes powered by two 1KW power amplifiers which were excited by a common 13.56 MHz oscillator. The voltage phase between the two electrodes was adjusted by a phase delay network. Optical access to the wafer surface was achieved through a CaF_2 window. For normal to the wafer plane imaging, the top

electrode was replaced with the window and system was operated in an open-ended diode mode by applying power only to the lower electrode. For oblique imaging, the system was operated with the top electrode in place in the diode mode(top electrode grounded) or in the triode mode(both electrodes powered with the chamber wall as the grounded electrode). Typical experiments were performed for normal imaging unless described otherwise.

5.3 End-point Detection and *In Situ* Monitoring of Uniformity of Etching

End-point detection and uniformity of etching are the major concerns in plasma etching because very thin gate oxides(<100 Å) used for modern VLSI and ULSI circuits cannot tolerate over-etching. These become more critical as the wafer size increases or a new higher etch-rate process is developed. Also, in deep trench etching, good uniformity is required to have a uniform capacitance distribution in the trenches across the wafer.

At present time, the available techniques for end-point detection include: laser reflection interferometry[83,84], optical emission spectroscopy[85], mass spectrometry[86], ellipsometry[87], plasma impedance monitoring[88] and infrared absorption spectroscopy.[89] However, these techniques either yield end-point information limited only to a single or few points on the wafer or provide a qualitative information on uniformity of etching. The infrared camera thermally maps the wafer during etching and utilizes a drastic change in the emissivity at a thin film interface to detect the end-point. This technique can monitor end-point spatially on the entire wafer and can determine uniformity of etching in real-time.

Considerable efforts have been made in understanding and reducing the non-uniform etching generally observed in plasma processing. Non-uniformity can be caused by gradients in etchant concentration, ion bombardment flux or ion energy.[90]

Such gradients tend to develop at the boundary of the wafer and are thought to be responsible for the commonly observed "bull's eye" clearing pattern where the etch rate monotonically decreases from the wafer periphery to its center. In practice, pressure, power, inter-electrode distance and gas flow are interactively adjusted until an acceptable uniformity is achieved. This empirical approach is taken because the underlying mechanisms responsible for non-uniform etching are not known quantitatively. A large number of time-consuming experiments are required to find a satisfactory process, since uniformity can not be measured by conventional means without taking the wafer out of the reactor. Hence, *in situ* monitoring of spatial uniformity and end-point can have an enormous value for achieving very rapid optimization of reactor settings and for real-time process monitoring and control.

In a standard self-aligned MOS fabrication process, highly doped polysilicon or polyside layers (used as a gate material) deposited on the gate and field oxides are etched. It is required to stop etching(end-point detection) when the gate material is completely removed from the gate oxide for minimal device damage. Thermal imaging by the infrared camera was found to be very useful for end-point detection and for real-time monitoring of uniformity of etching for these type of processes. This is due to the fact that the emissivity of the thin film multilayer structure changes drastically at the thin film interface in these type of processes.

5.3.1 Emissivity Model for a Thin Film Multilayer Structure

Any material at temperature above the absolute temperature generates radiation within its entire volume. The emissive property of the material; however, is strongly dependent on the optical properties of the material. In other words, emission of radiation is a volumetric process and only a portion of the radiant flux generated within the material will be emitted. For a strongly absorbing material such as metal,

only few micron thick surface layer will contribute to the radiation. For semitransparent materials, such as Si, the entire volume of the material will contribute to the total emitted radiation. The emission from a semitransparent slab with parallel surfaces was first described by McMahon,[91] in which, he introduced the concepts of spectral emissive power and apparent reflectance and transmittance. His theory was limited to only the passage of radiant energy normal to the surface but is very useful to the very common problem of interpretation of reflectance and transmittance.

In his model, he considered a slab of total thickness(d) with optical properties $n(\lambda,T)$ and $k(\lambda,T)$ and defined the volume emissive power, $j(\lambda,T)$, as the radiant flux generated per unit volume within the wavelength interval $\lambda+d\lambda$ for a material at temperature T. He considered the propagation of radiant flux generated by a very thin layer (dx) and then integrated the radiation emitted from the entire thickness of the slab.

In the course of traversing through the slab, the radiant flux is diminished by a factor $e^{-\alpha d}$, where α is the absorption coefficient. The internal transmittance, t, of the slab can be defined as:

$$t = e^{-\alpha d} \tag{19}$$

The incident flux upon striking the surface is partially reflected and the balance passes through the interface. The reflected portion is given by the reflectivity computed from the Frensal relations for normal incidence conditions as:

$$r = \left(\frac{\bar{n}-1}{\bar{n}+1}\right)^2 \tag{20}$$

where

$\bar{n}$ is the complex index of refraction.

It is important to recognize that this reflectivity, r, is based upon single reflection. By integrating the emitted flux over the entire thickness(d), comparing the emitted radiation with that of a blackbody and using the existence of energy balance between the emission and absorption of a body in thermal equilibrium, he showed that the emissivity for a semitransparent slab can be given as

$$\varepsilon(\lambda,T)=\frac{\{1-r(\lambda,T)\}\{1-t(\lambda,T)\}}{1-r(\lambda,T)t(\lambda,T)} \tag{21}$$

He also showed that Kirchhoff's law can be applied to the semitransparent slab in the form of:

$$\varepsilon(\lambda,T)=1-R(\lambda,T)-T(\lambda,T) \tag{22}$$

where

$R(\lambda,T)=r\left[1+\frac{t^2(1-r)^2}{1-r^2t^2}\right]$ and $T=t\left[\frac{(1-r)^2}{1-r^2t^2}\right]$ are the apparent reflectivity and transmittivity and includes the multiple reflections.

Figure 45 illustrates a simple ray trace analysis for calculating apparent reflectivity and transmittivity for a semitransparent slab.

Gordon[92] extended the theory of McMahon for hemispherical emission. He included the directional dependence of plane parallel and plane perpendicular polarization components and treated the flux generated as randomly polarized. He concluded that Eq. 22 can be used for emission in any direction.

The model given by Eq. 22 can be easily extended to the practical application of plasma etching, where thin films are present on a semitransparent substrate. However, the interference occurring from the coherent reflections from thin film interfaces should also be included in the model.

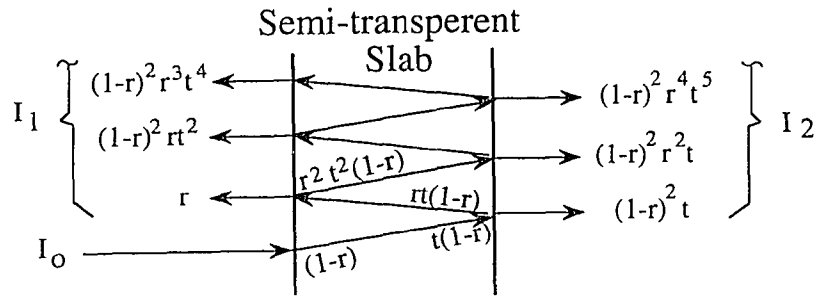

$$R = \frac{I_1}{I_0} = r + (1-r)^2 rt^2 + (1-r)^2 r^3 t^4 + \ldots = r\left[1 + \frac{t^2(1-r)^2}{1-r^2t^2}\right]$$

$$T = \frac{I_2}{I_0} = (1-r)^2\left\{t + r^2t^3 + r^4t^5 + \ldots\right\} = \frac{t(1-r)^2}{1-r^2t^2}$$

Figure 45 The apparent reflectivity and transmittivity of a semitransparent slab.

If the optical properties of the films and the substrate are known, emissivity of any multilayer structure can be determined by calculating apparent reflectivity and transmittivity using thin film optical analysis. A detailed account on thin film optical analysis is given in the book by H. Macleod.[93]

5.3.2 End-point Detection of Polysilicon Etching

The emissivity of a multilayer structure can be calculated by the model discussed in the previous section. Figure 46(b) shows the calculated transmittance, reflectance and emittance at 4.1 μm as a function of the thickness of the films for a multilayer structure as shown in Figure 46(a). The simulation of emissivity in Figure 46(b) was done using Film*Star Thin Film Evaluation Package and includes the effects of the free carrier absorption on n and k. Due to very high thermal conductivity of Si, a

constant temperature can be assumed throughout the thickness of the wafer for the purpose of modeling emission of thermal radiation from the silicon wafer (see Section 5.5.1). The emissivity of the multilayer is calculated only at 4.1 μm wavelength since the detector response peaks in the vicinity of this wavelength for the temperature range of interest in plasma etching. The spectral dependence of emissivity in the spectral range of interest can also be calculated using this model but was not required for the purpose of end-point detection. The doping concentration of the polysilicon film used in experiments is estimated to be about 2 X 10^{20} cm^{-3}. The values of refractive index (n) and extinction coefficient (k) at 4.1 μm for the polysilicon films with doping concentration of 2 X 10^{20} cm^{-3} were obtained from the published data by J. Lavine et. al.[94] The inspection of the variation of thermal emissivity with thickness of the multilayer structure in Figure 46(b) indicates that emissivity change at the interface can be used to monitor end-point and uniformity of etching across the wafer.

This model does not represent the actual emissivity because it does not account for the back-side roughness of the wafer (which can result in scattering and incoherent reflections) and reflections from the water-cooled back-plate on which the wafer rests. The reflections from the water-cooled back plate can be considered in the model by assuming a multilayer structure in which a reflective Al back-plate is placed underneath the wafer and is shown in Figure 47(a). Figure 47(b) shows the calculated transmittance, reflectance and emittance at 4.1 μm as a function of the thickness of the films for a multilayer structure as shown in Figure 47(a). Comparison of Figure 46(b) and 47(b) shows that reflections from the back-side water-cooled plate increase the total emittance. However, the qualitative change in emissivity as a function of thickness of film being etched is similar in both cases. The model without a reflective back-plate is sufficient to describe the end-point detection by the infrared camera; therefore, only this model is used throughout this chapter.

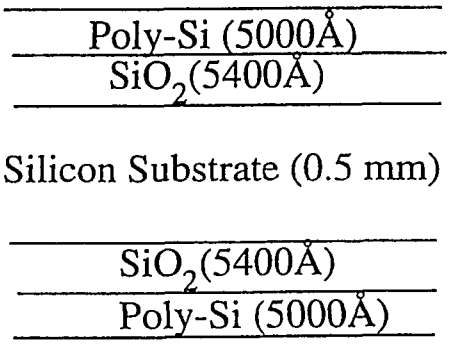

(a)

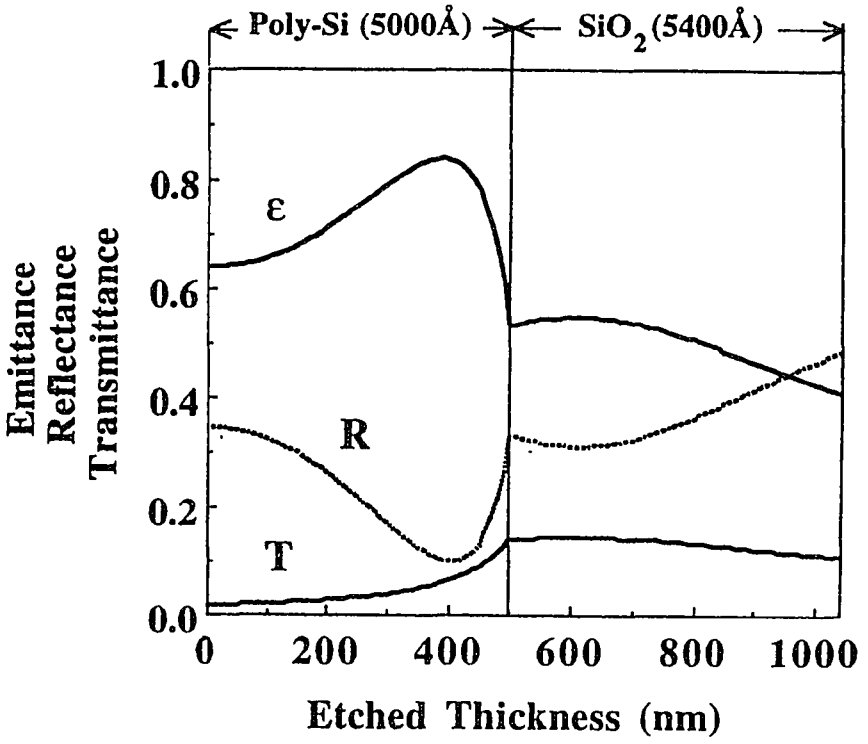

(b)

Figure 46 Calculated reflectance, transmittance and emittance at 4.1 μm as a function of thickness of the material being etched in (b) for the multilayer structure as shown in (a).

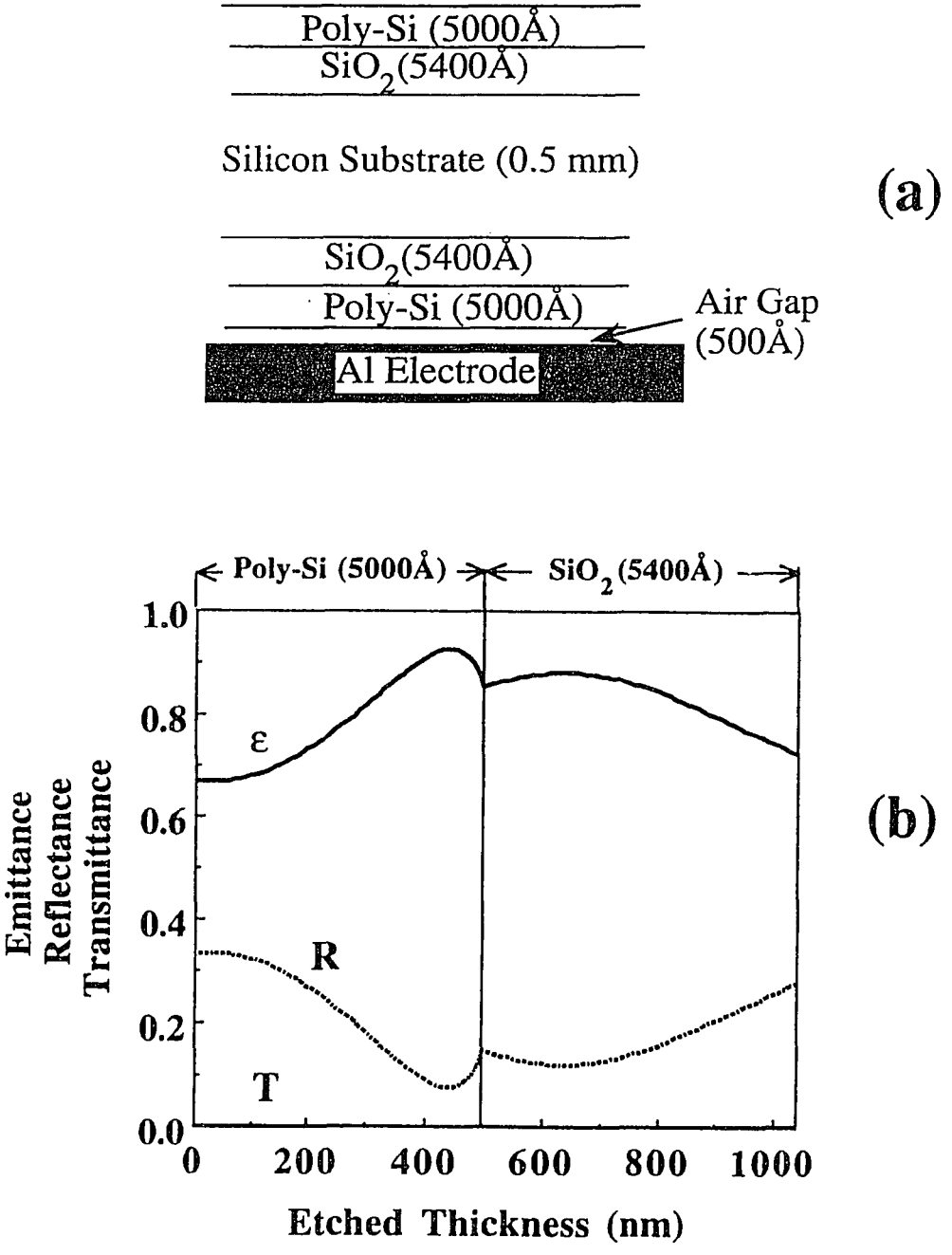

Figure 47 Calculated reflectance, transmittance and emittance at 4.1 μm as a function of thickness of the material being etched in (b) for the multilayer structure as shown in (a).

Scattering from the rough back-side of the wafer is very difficult to model and can affect the magnitude of the reflected signal from the back-plate. The average surface roughness of the back-side of the wafers used in this study was found to be in the range of 1-2 μm, which is comparable or less than the spectral wavelength range of interest. Therefore, scattering from the rough back-side was not included in the model.

The application of infrared imaging for end-point detection during plasma etching of the polysilicon-SiO_2-Si multilayer(see Figure 46(a)) is illustrated in Figure 48(b) and is compared with the commonly used laser interferometry technique for thickness monitoring as illustrated in Figure 48(a). Figure 48(b) represents the signal detected by a single pixel (located in the center of the wafer) out of the entire pixel array. With the imaging optics used for this experiment, each pixel represents signal emitted by an area of approximately 0.1 mm^2 on the wafer. A CF_4 and 15% O_2 gas mixture was used during plasma etching at a total pressure of 25 mTorr. To differentiate the effect of temperature rise from that of the emissivity variation on detected signal, the solid curve representing the infrared signal detected during etching of front-side polysilicon/SiO_2 multilayer should be compared with the superimposed dotted curve representing the infrared signal obtained during etching of a plain silicon wafer (with multilayer on the back-side only) under identical conditions. Furthermore, inspection of the infrared signal (solid curve) in Figure 48(b) shows that it is consistent with the computed curves in Figure 48(b) and the comparison with the laser interferometer signal in Figure 48(a) shows that the end-point for etching of the polysilicon can readily be detected. The end-point of the SiO_2 etching was not found to be identical for both techniques due to nonuniformity in etching. Although the detected signal was coming from the same location on the wafer in both cases, exothermic Si etching due to higher etch-rate on the edge of the wafer caused the wafer temperature to rise prior to the detection of the SiO_2 etching end-point by laser

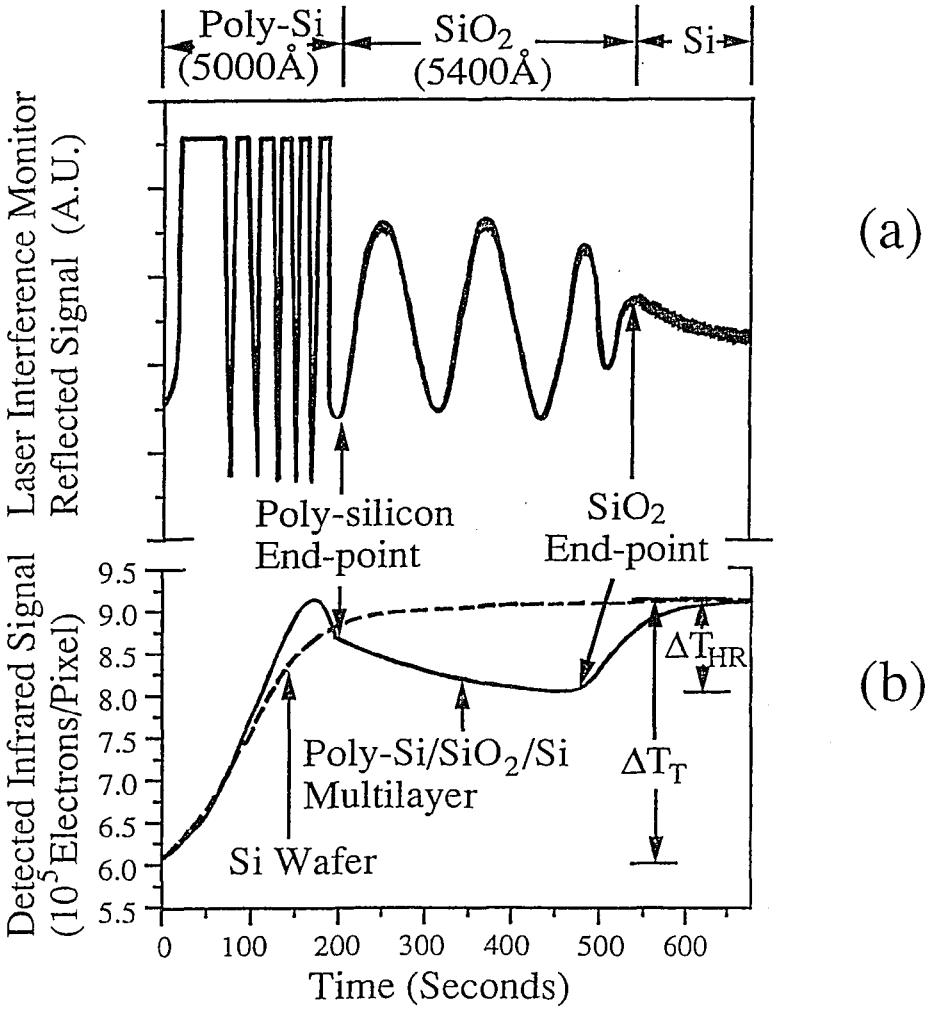

Figure 48 Comparison of experimental data on end-point detection by laser interferometry and thermal imaging during plasma etching showing the laser interference fringes(truncated) in (a) and detected infrared signal from the multilayer structure (solid line) and a plain silicon wafer(dotted line) etched under identical conditions in (b).

interferometric technique. It is also interesting to note in Figure 48(b) that the increase of the infrared signal after the etching of SiO_2 is completed is due to the exothermic heat reaction associated with the etching of silicon in CF_4/O_2 plasma. In this test, the etch-rates of polysilicon and SiO_2 are estimated (see Figure 48(a)) to be 2100 Å/min and 1040Å/min, respectively. As shown in Figure 48(b), the temperature rise due to the change in heat of reaction between SiO_2 and Si etching in this case is estimated to be ΔT_{HR}= 16 °C as compared to the total temperature rise ΔT_T= 54 °C. More discussion on the temperature change due to heat of reaction is presented in Section 5.4.4.

End-point detection using infrared camera is also compared with a newly developed technique based on plasma impedance monitoring. Figure 49 compares the end-point detection by infrared imaging (viewing angle of 30° to normal in this case) with plasma impedance monitoring technique. End-points detected by these two techniques were not identical due to non-uniformity of etching. The infrared signal shown in this figure represents only a single point on the wafer; whereas, the plasma impedance monitoring technique represents an averaged signal over the entire area of the wafer. When the infrared images of the entire silicon wafer are analyzed (see section 5.3.5), both techniques agree well and the thermal imaging technique has the advantage of providing etching information spatially on the entire wafer. A detailed description of the end-point detection by plasma impedance monitoring technique is presented in Appendix B.

In these cases, the polysilicon (5000Å) film which was present on the back side of the wafer contributes significantly to the total emitted signal after the polysilicon layer on the front surface is removed. The change in signal which enables the detection of end-point is not very large.

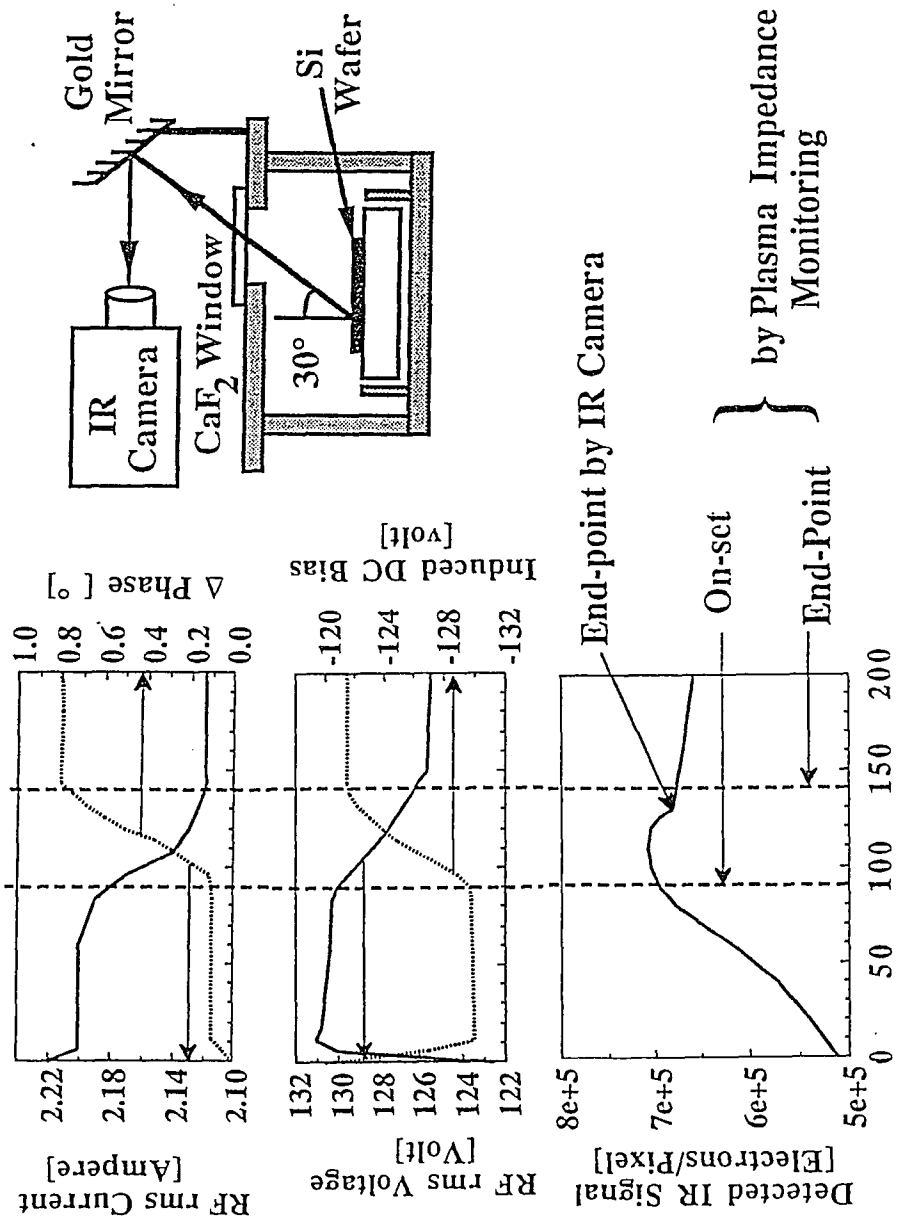

Figure 49 Comparison of experimental data on end-point detection for polysilicon/Si02(5.4KÅ) etching by plasma impedance monitoring and thermal imaging at an angle 30° to normal.

5.3.3 Effect of Back-side Polysilicon

Figure 50(a) shows the emissivity(calculated) variation using the structure of Figure 46(a) with and without thin film layers on the back-side of the wafer. As can be seen from the figure, the thermal radiation emitted from the etched polysilicon is the main source of the detected signal in absence of the polysilicon oxide film on the back-side. Figure 50(b) shows the detected infrared signal during the etching of polysilicon film on oxidized wafers with and without films on the backside, etched under identical conditions. Inspection of this figure shows that for the case without films (specifically polysilicon film) on the backside, the end-point of etching can accurately be detected and the experimental results compares well with the calculated results of Figure 50(a).

Thus, the standard integrated circuit fabrication procedure, in which the polysilicon/oxide on the backside is removed prior to plasma etch, results in an improved end-point detection scheme.

Discussion from here on is limited only to the case without films on the back-side of the wafer. In polysilicon gate etching, a polysilicon layer deposited on gate and field oxide is etched with only the polysilicon gate area masked. Thus, the end-point detection scheme should be able to detect the end-point regardless of the underlying oxide thickness.

Figure 51 shows the calculated emissivity for the polysilicon/SiO_2/Si as a function of oxide thickness. It can be seen from the figure that the end-point can be detected irrespective of the underlying oxide thickness, making this technique useful for detecting end-point in polysilicon gate etching.

5.3.4 End-point Detection on Patterned Wafers

Figure 52 demonstrates the feasibility of end-point detection on a patterned wafer. A photoresist masked polysilicon layer was etched on a oxidized (1000Å SiO_2) silicon wafer in an SF_6 plasma. The patterned mask contained features with 0.5 micron to 5.0

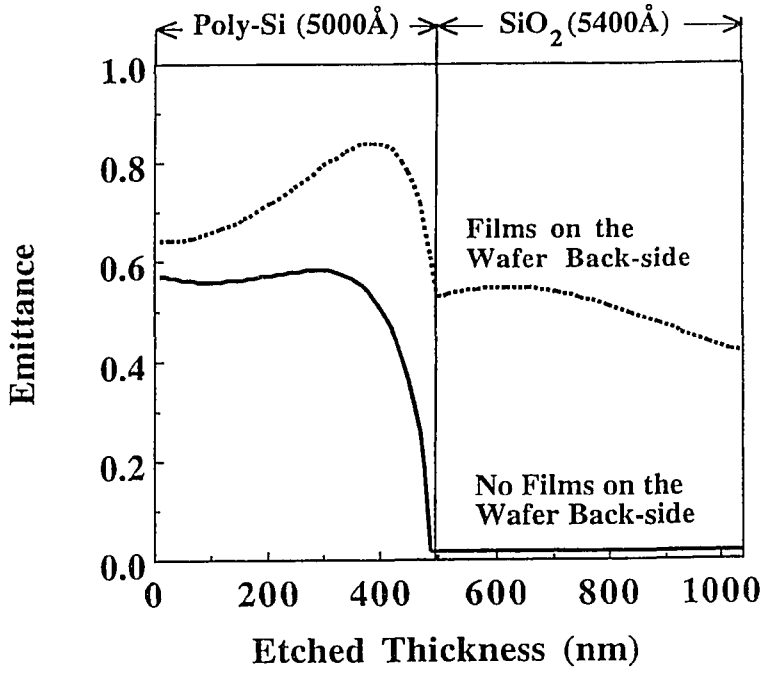

(a)

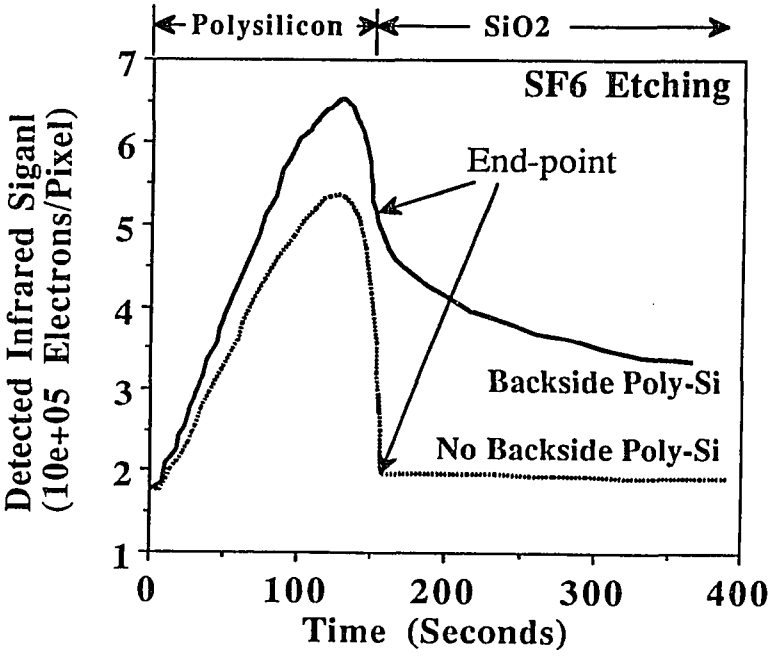

(b)

Figure 50 Effect of back-side polysilicon film on calculated emissivity variation in (a) and experimental end-point detection in (b).

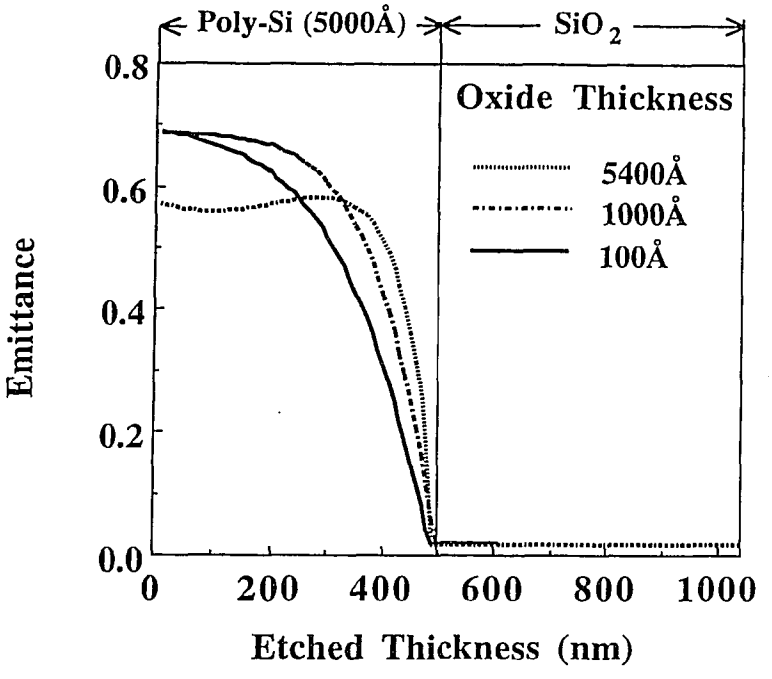

Figure 51 Calculated emissivity as a function of film thickness for the polysilicon/SiO_2/Si multilayer structure for various oxide thicknesses.

micron line-widths. Five 1.0 cm^2 knock-out chip areas were left unpatterned on the wafer to facilitate a comparison between end-points for both cases. The solid line(Pixel-1) represents the signal obtained from a pixel collecting signal from an unpatterned area and the dotted line(Pixel-2) represents the signal obtained from a pixel collecting signal from a patterned area. Inspection of this figure indicates that the change of slope of the dotted curve corresponds to the end-point of etching in the patterned area. With proper signal processing, it is possible to automatically detect end-point spatially on the patterned wafers. At this point it should be noted that the signal from each pixel represents an average signal emitted from ~0.1 mm^2 area on the wafer. Thus, the signal of the pixel viewing at the patterned area represents an

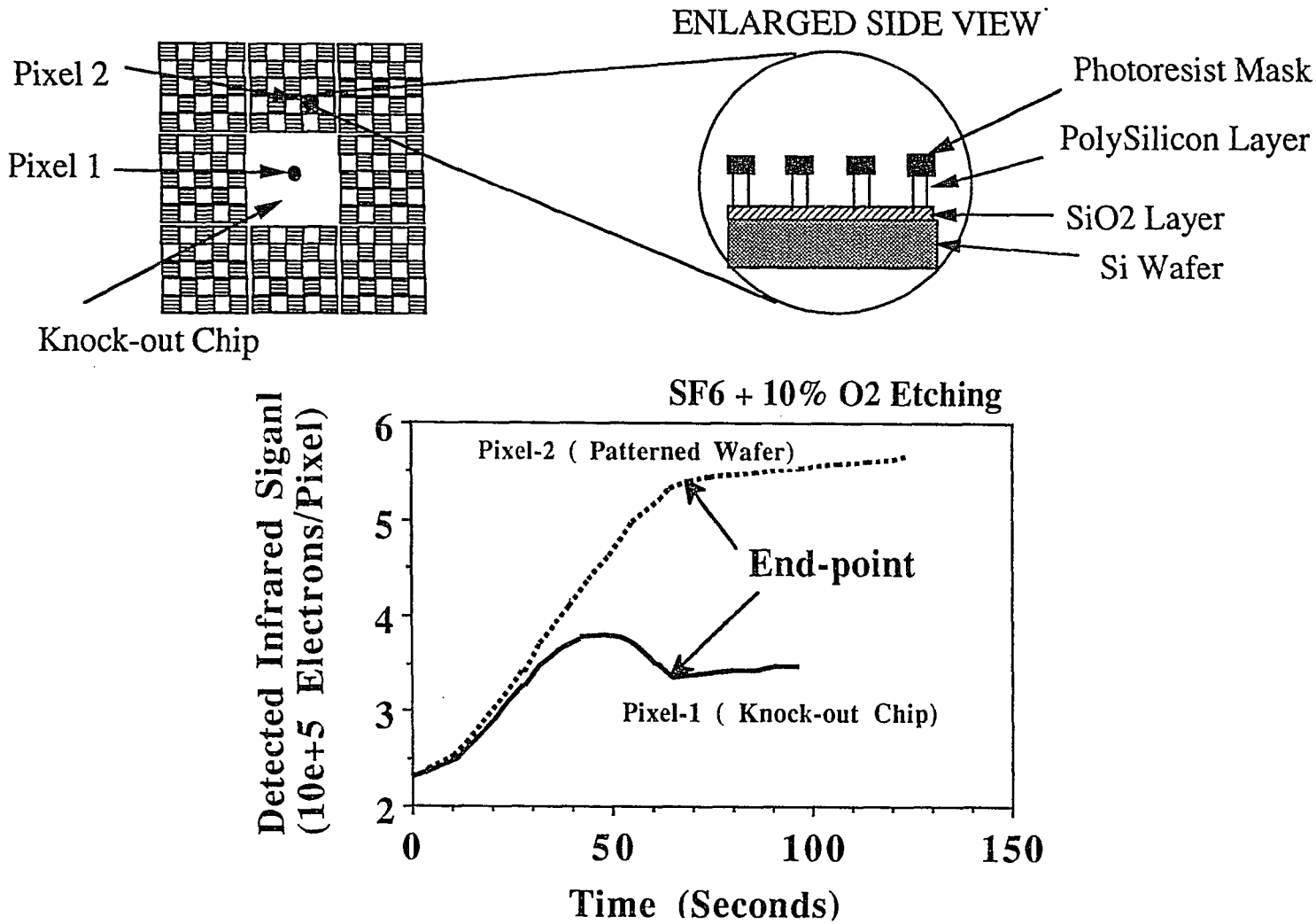

Figure 52 End-point detection for polysilicon etching on patterned area (dotted line) and unpatterned area (solid line).

average signal of etching many submicron and micron size features in that area. The signal is expected to be dependent on the feature sizes and geometries. Theoretical modeling for this case is extremely difficult because the emitted signal can be strongly polarized for the case where the features being etched have smaller dimensions than that of the emission wavelength.[95] It is also interesting to note that the signal from the unpatterned area after the polysilicon layer is completely removed from the unmasked area is higher in this case than that for the case of etching a blanket (without any patterns on the entire wafer) polysilicon etching (see Figure 50(b)). Plasma etching using SF_6 under the conditions used for this experiment is isotropic in nature. Thus, after the polysilicon layer was completely removed from the unmasked areas, lateral etching of polysilicon under the masked area caused the wafer temperature to be higher due to exothermicity of the polysilicon etching reaction.

5.3.5 *In Situ* Monitoring of Uniformity of Etching

Figure 53 illustrates the spatial end-point detection capability of the infrared imaging. The detected infrared signal intensity variation across the wafer during etching polysilicon on 7500Å SiO_2/Si in SF_6 plasma is plotted in this figure for an etch-time instant of 120 second. As can be seen from the figure that the spatial end-point of etching can be monitored by proper signal processing. If the initial thickness of the polysilicon layer being etched is known, the spatial average etch-rate can be obtained by real-time monitoring of progression of end-point.

Figure 54 shows the etch-rate counters as determined by monitoring the progression of end-point from the periphery towards the center of the wafer by the infrared camera. Thus, the infrared camera can be used for *in situ* determination of uniformity of etching.

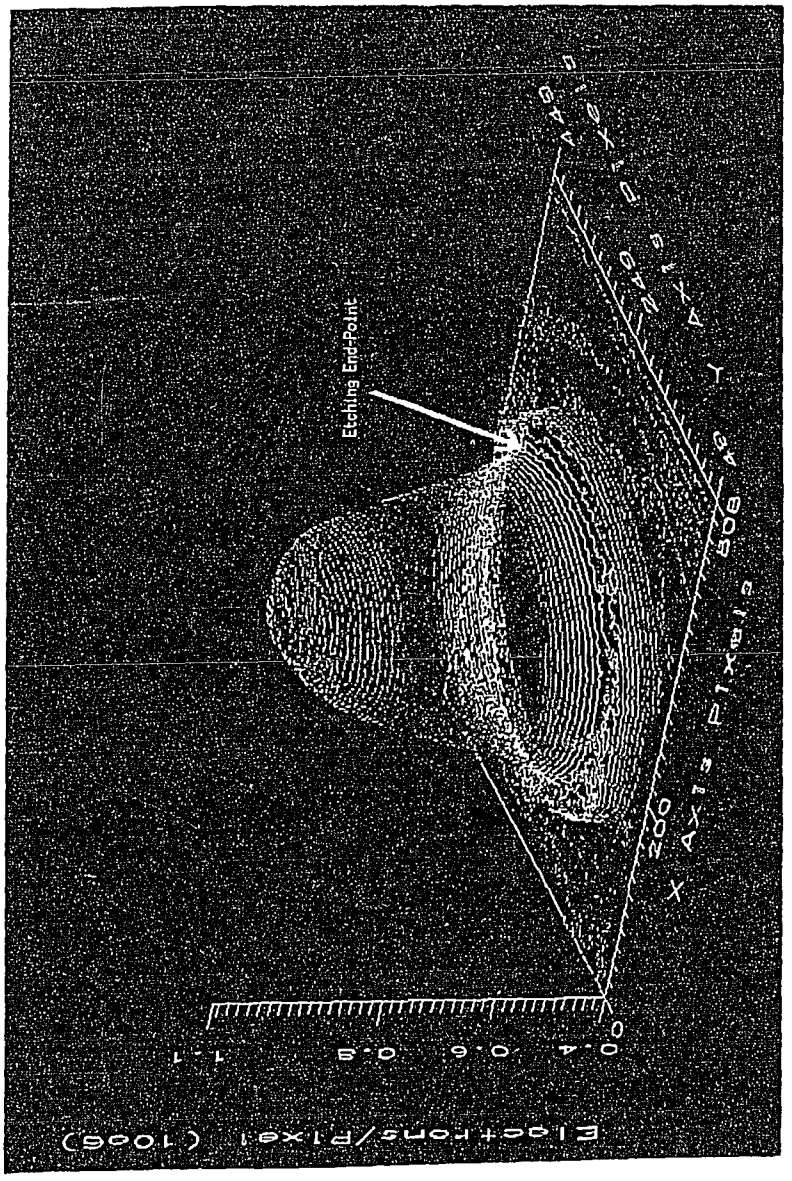

Figure 53 Detected infrared signal intensity variation across the wafer for an etch time instant of 120 second demonstrating spatial end-point detection capability.

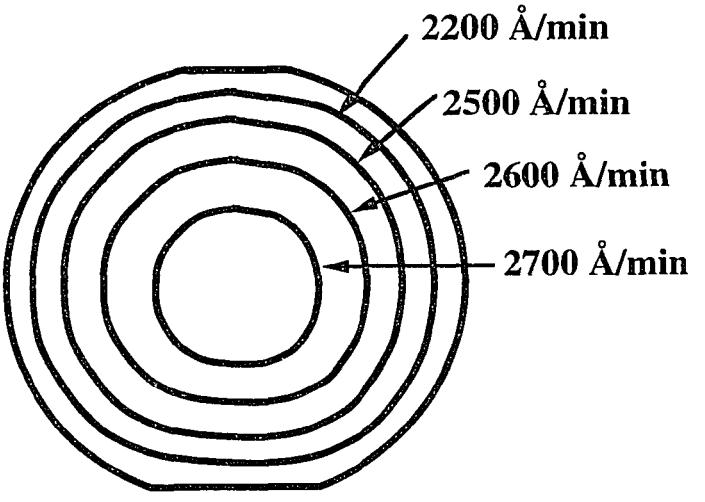

Figure 54 Average etch-rate counters determined by monitoring progression of end-point of etching.

5.3.6 End-point Detection for Silicide and Polyside Etching

Silicides and polysides are also extensively used as a gate material in VLSI and ULSI circuit fabrication due to their excellent electrical conductivity and high temperature stability.[96] Figure 55(a) shows the calculated emissivity of a $TaSi_2/SiO_2$(3000Å)/Si multilayer structure. The optical data used in emissivity calculations were obtained from the work published by A. Borghesi et. al.[97] A very pronounced peak followed by an abrupt drop in infrared signal was observed at $TaSi_2$/oxide interface. This is attributed to very high values of n and k for $TaSi_2$ in the infrared spectrum of interest. Figure 55(b) shows the experimental data of etching $TaSi_2/SiO_2$(3000Å)/Si multilayer in an SF_6 plasma. As can be seen from the figure that the experimental results compares well with the emissivity model in Figure 55(a).

In many integrated circuit fabrication procedures, the gate consists of a thin layer of silicide (~1000Å) deposited over a polysilicon layer (~4000-5000Å) to

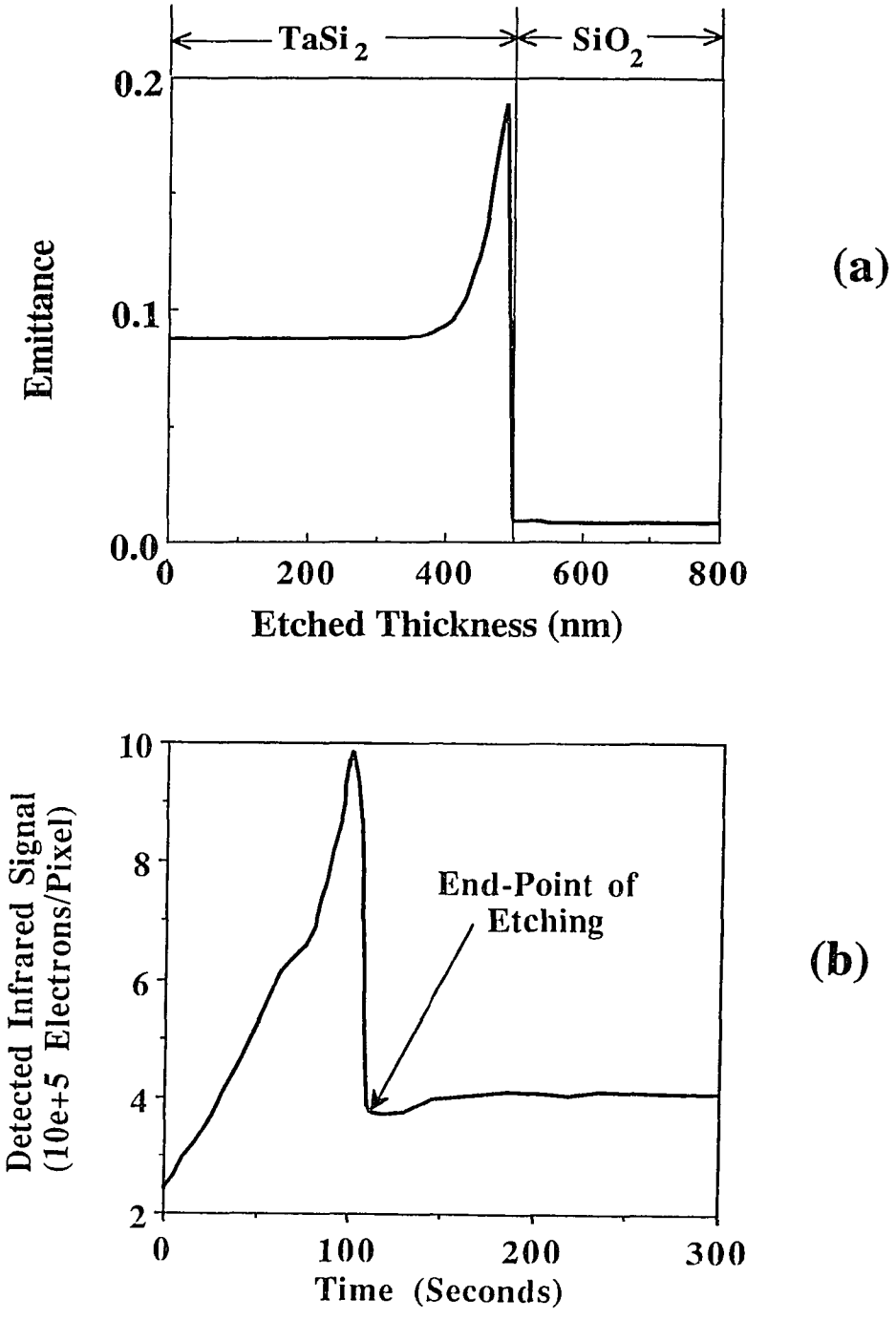

Figure 55 Calculated emissivity of a $TaSi_2/SiO_2$(3000Å)/Si multilayer structure as a function of film thickness in (a) and experimental data on end-point detection for the same structure in (b).

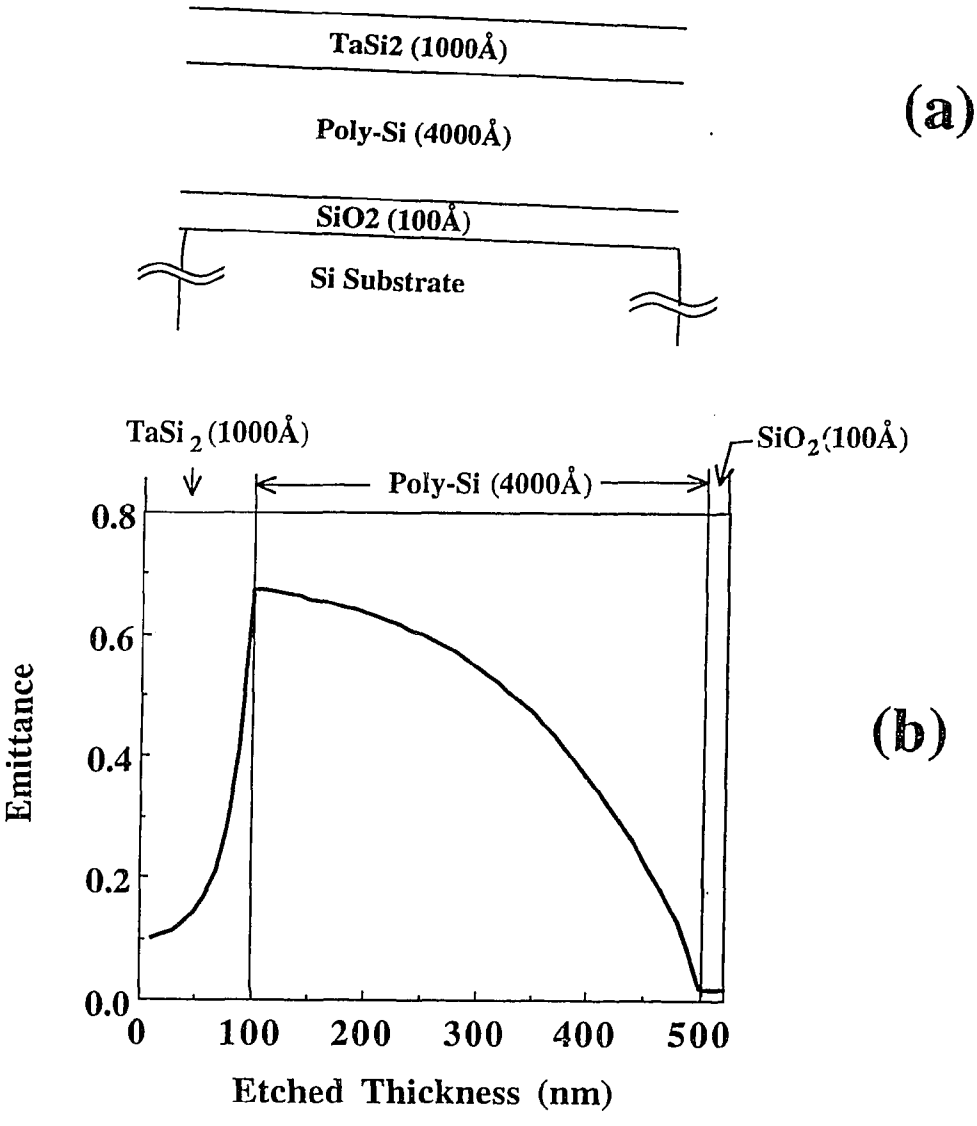

Figure 56 Calculated emissivity variation as a function of film thickness in (b) for a polyside multilayer structure shown in (a).

increase electrical conductivity of the gate and the combination of silicide and polysilicon is commonly known as polyside. Figure 56(b) shows the calculated emissivity variation as a function of film thickness for a polyside structure as shown in Figure 56(a). It can be seen from the figure that end-point of etching can be detected for both silicide and polysilicon layer.

5.3.7 Effect of Viewing Angle on End-point Detection

In modern parallel-plate etching tools, normal optical access to the wafer may not be possible. In order for this technique to be useful in production environment, it should be able to detect end-point at very high viewing angles. Figure 57(a) and 57(b) shows the calculated emissivity variation for various viewing angles(to normal) during etching of polysilicon on oxidized(1000Å) Si and etching of $TaSi_2$ on oxidized(3000Å) Si, respectively. It can be seen from the figure that this technique should be able to detect end-point at very high viewing angles. It is interesting to note that the directional (not normal) emissivity of the multilayer(unetched) is higher than the normal emissivity for a wide range of viewing angles. The emitted radiation from an unpatterned wafer is normally randomly polarized. The directional dependence of the s-polarized(plane perpendicular) component of the radiation causes the directional emissivity to be higher than the normal emissivity for absorbing material such as $TaSi_2$ and polysilicon.[98]

Figure 57 demonstrates the feasibility of using this technique for spatial end-point detection of $TaSi_2$ etching on production-type parallel plate triode reactor (See Figure 42(b)) with an oblique viewing angle of 80° to normal. With proper choice of optics for depth of focus, a rectangular window can be used to image the entire wafer in a parallel plate tool configurations where normal imaging is not possible. It is also interesting to note that the edges of the wafer have very high emissivity even after the $TaSi_2$ film is removed from the edge of the wafer. This is due to the fact that emissivity is a volumetric process. The emission from the edge of the wafer represents a large wafer thickness at very high viewing angles. Also, parallel surfaces of the wafer can act as a wave-guide to the internally generated radiation. The signal emitted from the edge of the wafer can also be utilized for temperature measurements.

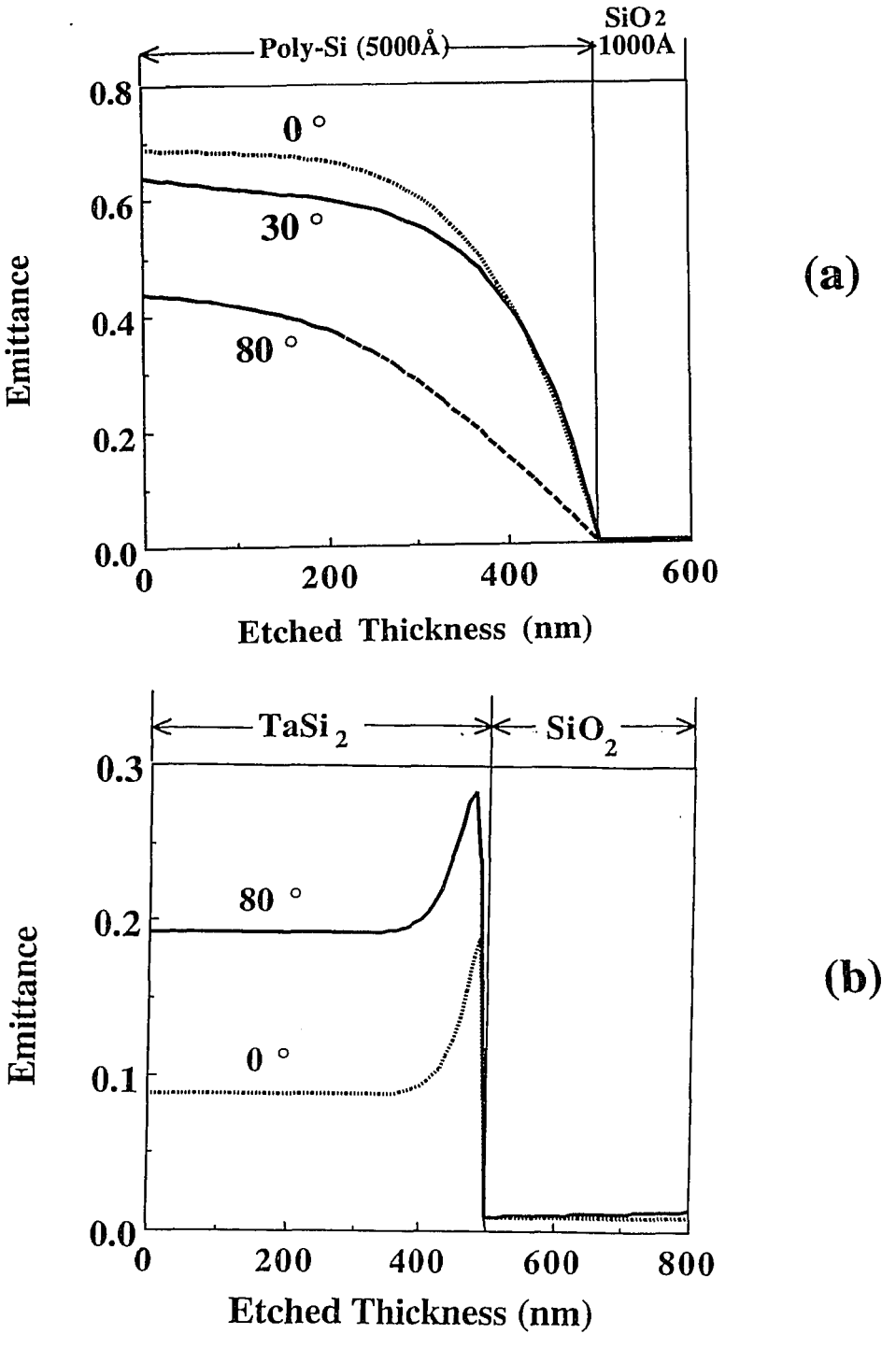

Figure 57 Calculated emissivity variation as a function of film thickness for various viewing angles for polysilicon on oxidized(1000Å) Si in (a) and $TaSi_2$ on oxidized(3000Å) Si in (b).

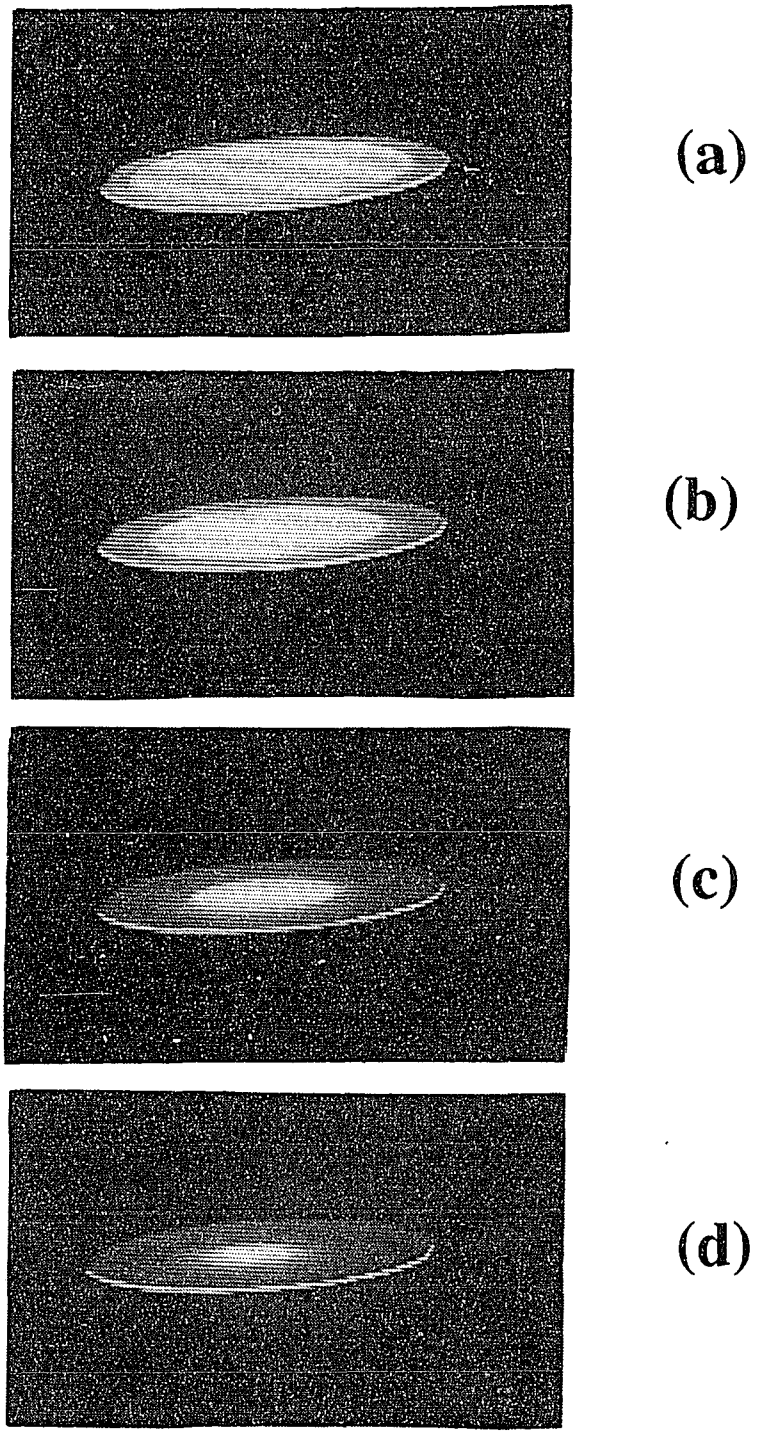

Figure 58 Spatial end-point detection of $TaSi_2$ etching with an viewing angle of 80° to normal in parallel-plate triode reactor at four different time instants (a) 250 seconds, (b) 265 seconds, (c) 275 seconds and (d) 280 seconds.

5.4 Temperature Measurements

5.4.1 Introduction

Accurate determination of substrate temperature by non-obtrusive means is important in many processing technologies for both process control and repeatability. In plasma etching, for example, the substrate temperature can critically effect the etch-rate and etch profile.[99,100,101] It is also well known that the wafer temperature can affect the integrity of the resist. Therefore, it is necessary to control the wafer temperature below the thermoplastic flow temperature where solvent loss and cross linking of the bulk can cause a contraction and hazing of the resist.[102,103]

Contact techniques such as thermocouples cannot be used due to the following reasons: (a) the impracticality of making thermal contact to substrates during etching; (b) thermal contact irreproducibility; (c) erroneous reading due to plasma induced rf interference; and (d) possibility of contamination of the wafer and the reactor ambient. Fluorescence based thermometry can measure substrate temperature accurately[104]. However, measurement using fluoro-optic probe is inherently intrusive since the probe must be thermally bonded to the wafer and the fiber must be coupled out through the plasma or from the back side of the wafer through the electrode. Several other techniques have been proposed to measure wafer temperature over the years which include- infrared-laser interferometric thermometry[105], projection moiré interferometry[106] and pulsed photoluminescence spectroscopy.[107] None of these techniques can be used for temperature monitoring and control in semiconductor manufacturing environment because the infrared-laser interferometric thermometry requires double-side polished wafer and a reference temperature, the projection moiré interferometry requires a grating structure on the wafer and the pulsed photoluminescence spectroscopy is suitable only for large quantum yield materials, such as II-V and II-VI semiconductors. Pyrometry, in general, suffers from unknown

emissivity related problems and conventional pyrometers are not sensitive in the temperature range of interest in plasma etching. Despite of these complications, it appears that the most suitable remote temperature sensing technique has to be based on the measurement of emitted radiation for process monitoring and control in production environment.

The infrared camera described in Section 5.2 is used to infer wafer temperature and to estimate wafer temperature gradients in the wafers during plasma etching. In principle, the infrared camera can be used to measure temperature of a radiating surface, if the spectral emissivity of the surface and spectral transmission of the optical components are known. Experimental results of remote temperature measurements of a black-body source using the IR camera system using various narrow-band transmission filters are shown in Figure 59 and are compared with the theoretical calculations (solid line) using Eq. 17. Inspection of Figure 59 shows that there is a good agreement between the theoretical and experimental data.

In plasma etching, however, the emissivity of the wafer is strongly dependent on the film thickness present on the wafer (which changes temporally and spatially across the wafer due to non-uniform etching) and is rarely known for realistic situations. It is extremely difficult to measure wafer temperature accurately using a single spectral-band radiometer during a realistic etching process where the silicon wafer can consist of multiple films and a patterned mask. However, measuring wafer temperatures during etching of unpatterned wafers can be very useful in elucidating some of the basic mechanisms and for estimation of wafer temperatures during a realistic process. Reflections from the electrode(chuck) surface on which the wafer rests and the roughness of the backside of the wafer make it difficult to measure spectral emissivity of the wafer during etching. An alternative to measuring wafer temperatures using emissivity is to calibrate the infrared camera signal with various

wafers at known temperature. A proper calibration technique is required to minimize the errors in temperature measurements.

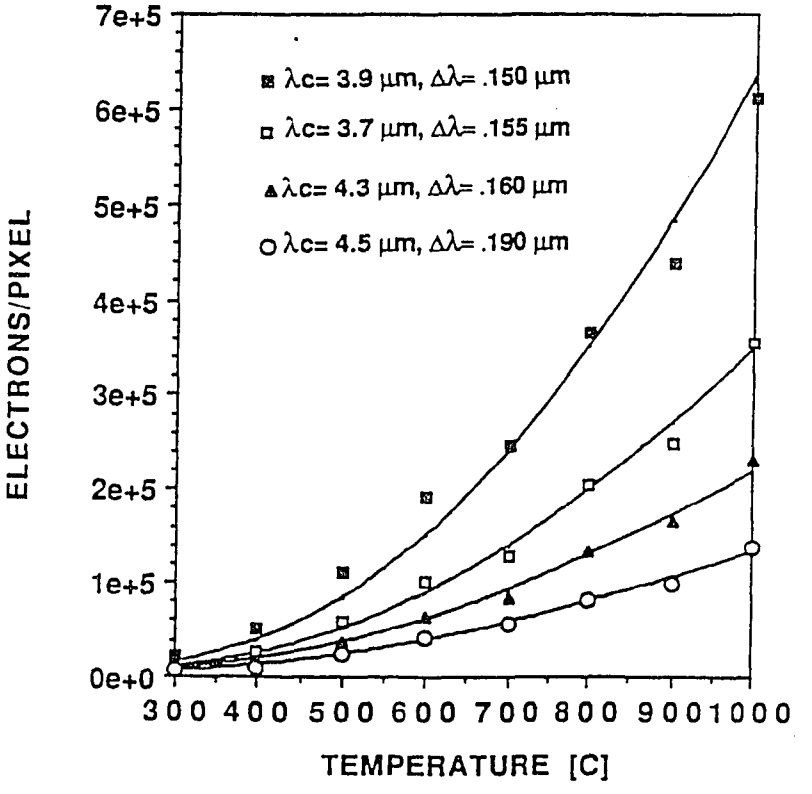

Figure 59 Calculated and measured signal of 320 X 244 IR-CCD imager using narrow-band filters.

5.4.2 Calibration Technique

A calibration technique is developed in which the infrared signal was measured as a function of temperature for various thermocouple attached wafers by heating them on a mirror-like hot-plate (hot plate emissivity < 0.02) under identical optical conditions used for etching experiments. The mirror-like hot plate serves two purposes: (1) it replicates the polished chuck surface; and (2) it has an emissivity of less than 0.02 in the spectral range of interest and thus does not contribute significantly to the total emitted infrared radiation.

Figure 60 shows the detected infrared signal for various film combinations on a Si substrate as a function of temperature using F/2.35 optics. In this figure, the signal emitted from a black painted wafer representing a blackbody surface is also platted so that the emission coefficients for various thin film combinations present on silicon wafer can be estimated. As can be seen from the figure, when the polysilicon layer is present on the front and/or back side of the wafer, the emission coefficients are very high as compared with that of a Si wafer without polysilicon layers. This is attributed to the free carrier absorption in the polysilicon layers due to high doping concentration($2X10^{20}$ cm^{-3}).

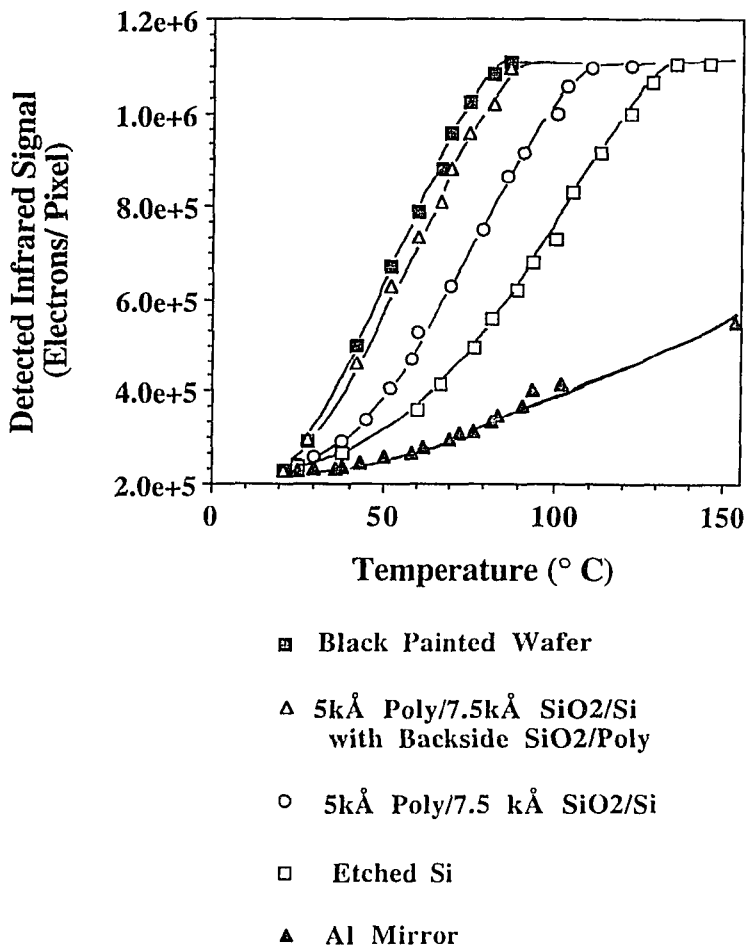

Figure 60 Calibration of the IR camera system for F/2.35 optics.

During plasma etching, wafers are generally placed on the water cooled powered electrode. The wafer temperature can rise significantly due to two reasons: (1) the energetic particle bombardment(mostly positive ions); and (2) exothermic etching reaction on the wafer surface. The wafer temperature was measured using infrared camera by converting the detected infrared radiation using the calibration data. The accuracy of measurement was tested using infrared laser interferometry and the error in the temperature measurements obtained by the calibration method were found to be less than 20%.

5.4.3 Effect of Process Parameters on Wafer Temperature

Steady-state substrate temperature was determined in a open-ended diode reactor configuration during plasma etching of a bare silicon wafer for various process parameters. The effect of pressure on steady-state temperature is shown in Figure 61 for Ar plasma. The steady-state temperature increases as the pressure decreases. This is due to two reasons. The induced bias and hence the energy of the ions striking to the wafer increases in a diode with decreasing pressure as described in Chapter 3. Also the heat transfer coefficient between the wafer and the water-cooled electrode decreases with the pressure (see Section 5.5.2).

Figure 62 compares the effect of power on steady state temperature of Si wafer in Ar and SF_6+20% O_2 plasma. The steady-state substrate temperature increases with the total applied power in both cases. An increase in power will increase the induced bias in a diode configuration causing steady state temperature to rise. For any etching process, it is desired to control the substrate temperature below the thermoplastic flow temperature of photoresist (which is typically in the vicinity of 200° C) for faithful pattern transfer. The substrate reach above 200° C for the applied power of nearly 200W and 400W power for Ar and SF_6+20%O_2 plasma, respectively.

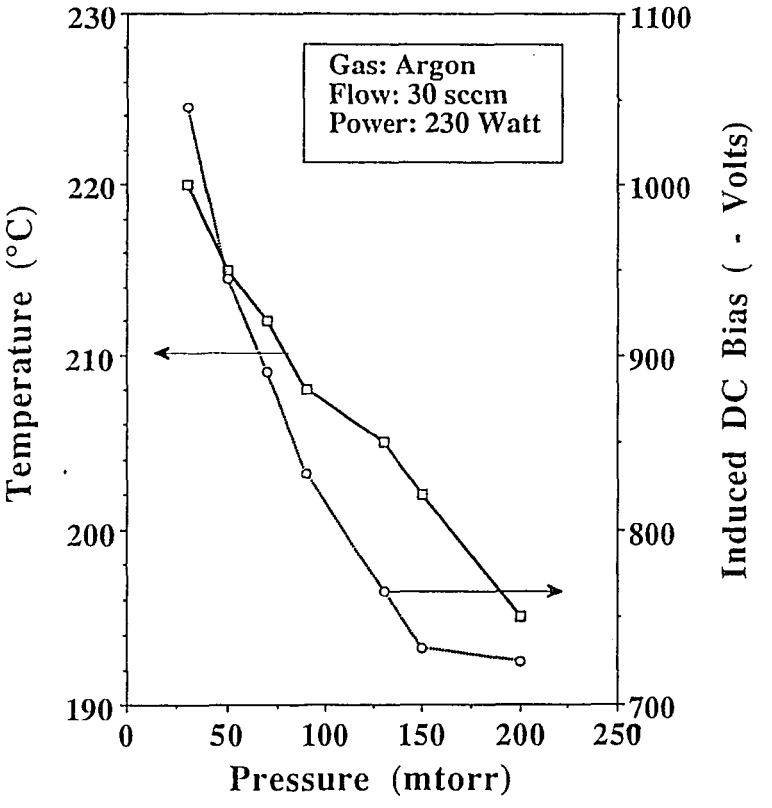

Figure 61 Effect of pressure on steady-state temperature in an Ar plasma.

Argon is an electropositive inert gas and the induced bias is higher in Ar plasma than the case of an highly electronegative SF_6+20%O_2 plasma for the same power level. Thus the wafer temperature in Ar plasma is expected to be higher. In SF_6 plasma, the substrate is being etched and the exothermic heat associated with the etching reaction can also be a significant heat source on the wafer. In diode etcher, the etch-rate also increases with the power. Even though the steady-state wafer temperature in SF_6+20%O_2 plasma is controlled by the combination of energy of the bombarding ions and the etch-rate, it was found to be much lower than that for Ar plasma for same power level.

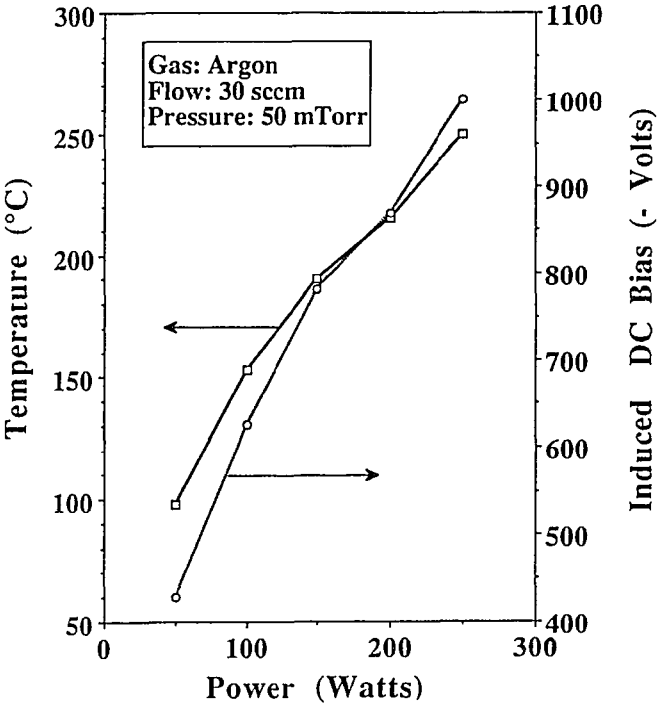

(a)

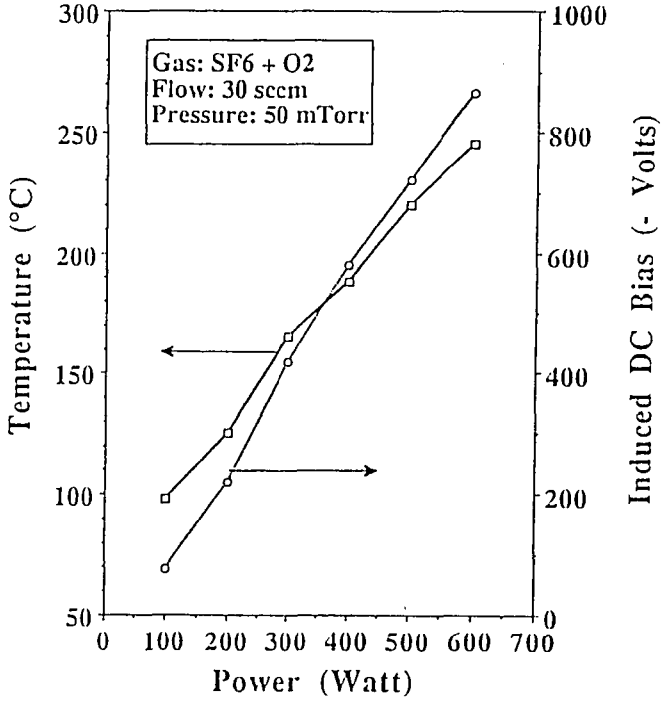

(b)

Figure 62 Effect of power on steady-state wafer temperature in a Ar plasma in (a) and an SF_6+20%O_2 plasma in (b).

Figure 63 compares the effect of flow-rate on the steady-state wafer temperature for SF_6+20%O_2 and Ar plasma. The temperature and the bias were found to be nearly constant in Ar plasma for the flow-rates in the range of 10 to 100 sccm commonly used in plasma processing. However, for the case of SF_6+20%O_2 plasma, they were found to be dependent on the flow rate. The etch-rate decreases even though the bias was found to be increased by nearly 100 V as the flow rate was decreased from 100 sccm to 10 sccm. The decrease in temperature is attributed to the "loading effect" commonly observed in plasma etching reactors. The etch-rates in the plasma reactors are generally flow-rate dependent due to depletion of reactive etchant species at low flow-rates. Thus, decrease in etch-rate and hence the exothermic heat caused the steady-state temperature to decrease at low flow-rate.

5.4.4 Heat of Reaction

Heat generated due to the exothermic etching reaction can be a major heat source on the wafer. Typical detected infrared signal during etching of polysilicon on oxidized Si wafer in a SF_6 plasma is shown in Figure 64(a). A selectivity of Si etching to oxide etching was approximately 8:1 in this case with Si etch-rate of ~7150Å/min and oxide etch rate of ~900Å/min. Inspection of Figure 64(a) shows an initial signal rise due to temperature rise during exothermic polysilicon etching and energetic ion bombardment followed by a sharp drop in signal at the end-point due to change in emissivity at the polysilicon/SiO_2 interface. The time required to reach a steady state condition is nearly 200 seconds for this case. During oxide etching, the signal (~39 °C) remained nearly constant and is followed by a rise in signal due to exothermic Si etching of Si substrate (75 °C). The detected infrared signal during etching using CF_4+ 10%O_2 plasma under identical pressure, power and flow condition used in Figure 64(a) is shown in Figure 64(b). The polysilicon and oxide etch-rates

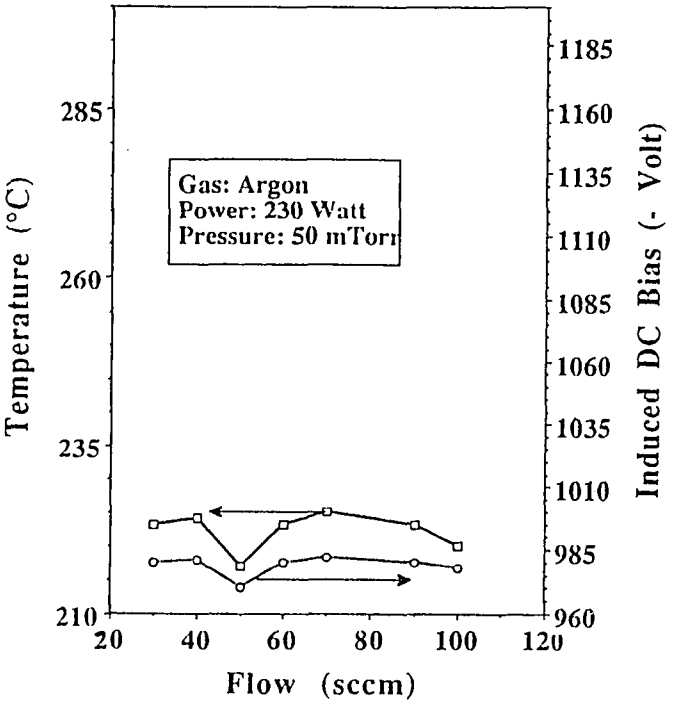

(a)

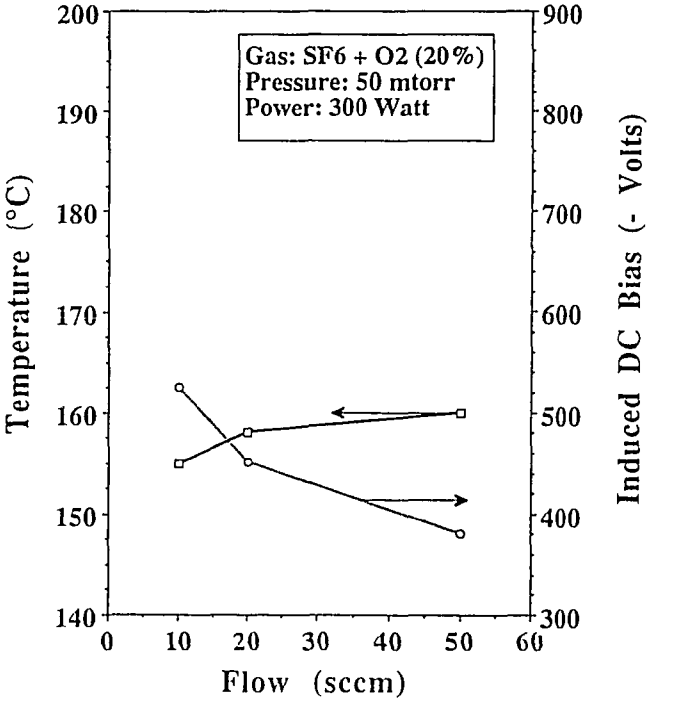

(b)

Figure 63 Effect of flow rate on steady-state temperature in a Ar plasma in (a) and in a SF_6+20%O_2 plasma in (b).

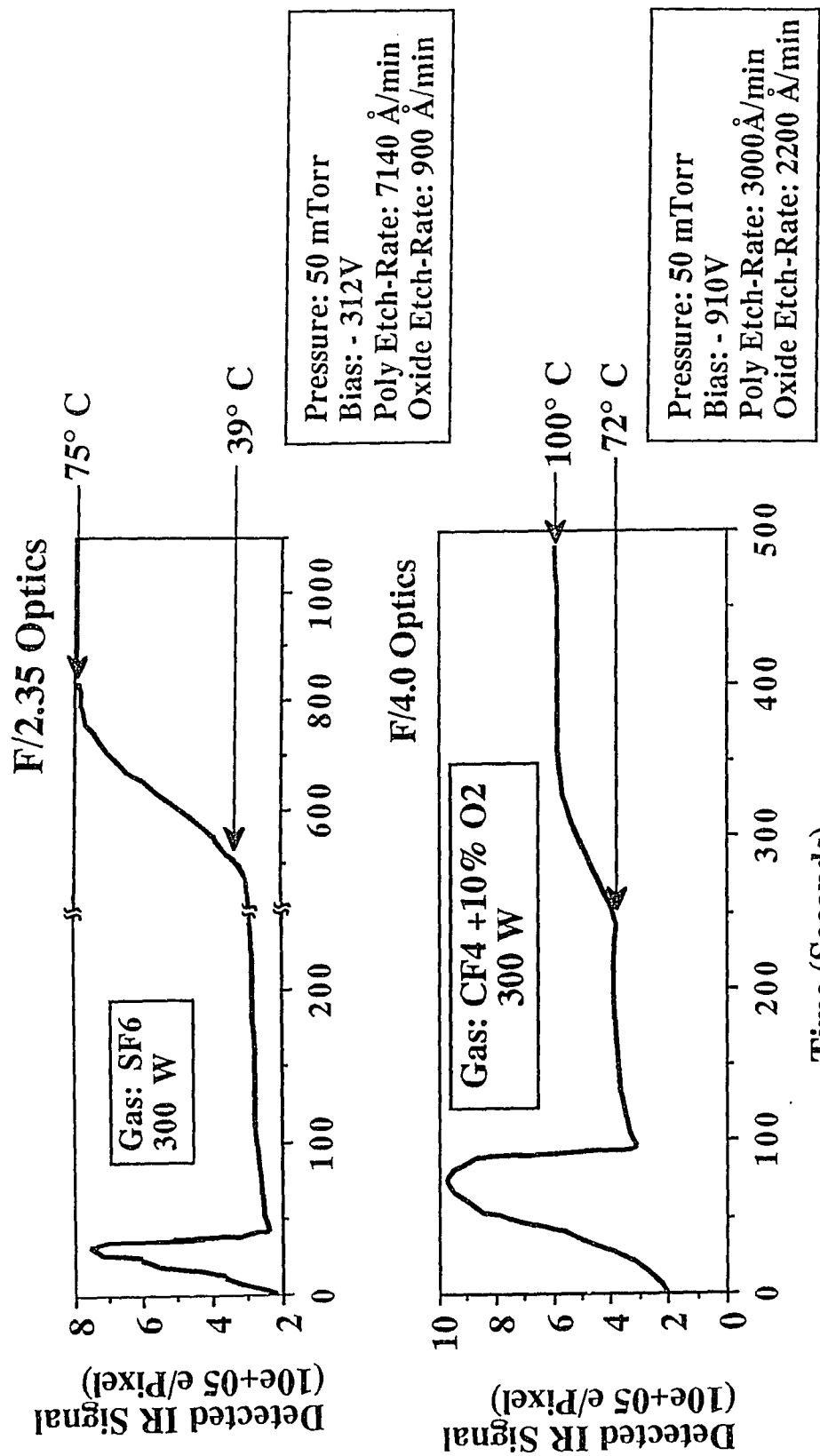

Figure 64 Illustration of heat load on the wafer due to etching reaction for SF_6 plasma in (a) and CF_4+10%O_2 plasma in (b).

were estimated to be 3000 Å/min and 2200 Å/min (selectivity of ~1.4:1), respectively, in this case. Inspection of Figure 64(b) shows that the steady state temperature during oxide etching is 72° C and is increased to 100° C during Si etching. Even though the Si etch-rate in this case is much lower than the case of SF_6 plasma, the steady state temperature is higher due to much higher value of induced bias. Comparison of Figures 64(a) and (b) suggests that for highly selective etching, the heat of reaction can contribute significantly to the total temperature rise. It should also be noted that the wafer temperature can be significantly different for the same gas chemistry depending upon the material and topography to be etched.

5.5 Heat Transfer Analysis

Temperature can be a critical parameter in determining reaction rates during plasma etching. It has been shown in recent publications that the temperature of the wafer being etched can significantly affect the etch-rate, selectivity and anisotropy.[108] The steady-state wafer temperature is determined by the heat transfer characteristics of the wafer-reactor geometry. In many plasma etching reactors, the wafer rests on a water-cooled electrode and no special provision is provided for improved heat transfer. In this case, the thermal transient time constants can be of the same order of magnitude of the total etching period and the wafer temperature is continuously changing during etching. A recent trend in the design of new generation of plasma etching reactor is to apply He gas on the back-side of the wafer to improve the heat transfer for achieving controllable and reproducible etching process.[109] Thus, developing fundamental understanding of heat transfer characteristics can lead to an improved reactor design for better wafer temperature control and etch-process reproducibility.[110]

5.5.1 Theoretical Model

The heat transfer characteristics of the silicon wafers during plasma etching can be modeled using a simple one-dimensional model[¥] as shown in Figure 65.

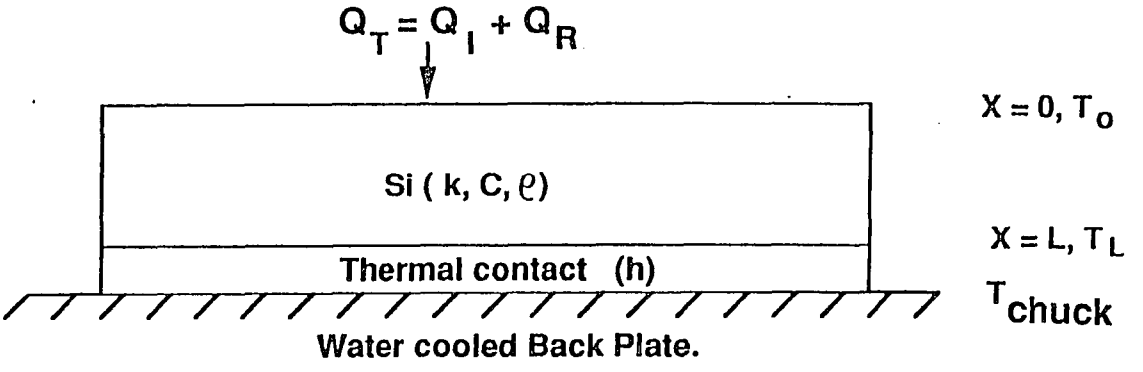

Figure 65 A simple model used for heat transfer analysis.

In this model, the total power input to the wafer during plasma etching is represented by $Q_T = Q_I$(ion bombardment) + Q_R(exothermic reaction), and is assumed to be uniformly distributed across the wafer. The thermal contact between the wafer and the water-cooled back plate can be defined by its heat transfer coefficient (*h* in J/m^2-s-K) and represents the major source for heat loss. The thickness of the silicon wafer is about 500μm, while that of polysilicon and oxide layer is 5000Å or less. Thus, heat transfer through these layers can be neglected. Since, it is desirable to control wafer temperature below 180°C, the radiation losses are expected to be negligible for this temperature range.

[¥] Contribution of Ayyagari Subramanyam in developing the one-dimensional heat transfer model is greatly appreciated.

The power dissipated to rise the gas temperature can also be neglected based on the following simple calculations

$$Power = F \cdot C_p \cdot (T_{out} - T_{in}) \tag{23}$$

where,

F- is the flow rate;

C_p-is the heat capacity of gas;

T_{out}- is the temperature of the outgoing gas; and

T_{in}- is the temperate of the incoming gas.

It is well known that in the process plasma, the ionization efficiency is very low and the neutral gas temperature is very close to room temperature. Only 0.43 W power is required for the temperate of CF_4 gas flowing at a flow rate of 20 sccm (8.12 $X10^{-4}$ moles/min) to be increased by 100 °C (which represents a worst case analysis) and heat loss due to this phenomenon can be neglected.

According to energy balance equation, the sum of the energy input and the energy generated internally should be equal to sum of the change in internal energy of the silicon and energy loss as given by

$$-kA\frac{\partial T}{\partial x}\Big|_x + \dot{q}Adx = \rho CA\frac{\partial T}{\partial t} - kA\frac{\partial T}{\partial x}\Big|_{x+dx} \tag{24}$$

where,

A- is the area of wafer;

ρ- is the density of Si;

C -is the heat capacity of Si; and

k- is the thermal conductivity of Si.

Since there is no internal generation of energy, after dividing both sides by $A\partial x$, Eq. 24 will reduce to

$$k\frac{\partial^2 T}{\partial^2 x}=\rho C\frac{\partial T}{\partial x} \tag{25}$$

Since the energy input is on the top surface of the wafer and energy loss is from the bottom surface of the wafer, the boundary conditions can be written as

$$-k\frac{\partial T}{\partial x}=Q_T \quad \text{at } x=0 \text{ ;and} \tag{26}$$
$$-k\frac{\partial T}{\partial x}=h[T-T_{chuck}] \quad \text{at } x=L.$$

where,

h-is the heat transfer coefficient of the intervening medium in J/m^2-S-K.

The solution for this typical heat transfer case is given by H. S. Carslaw and J. C. Jeager[125] as

$$T_x(t)-T_x(0)=\frac{Q_T}{h}\left[1+\frac{Lh}{k}\left(1-\frac{x}{L}\right)-\sum_{n=1}^{\infty}\frac{2\lambda\left(\alpha_n{}^2+\lambda^2\right)\cos\left(\frac{\alpha_n x}{L}\right)}{\alpha_n{}^2\left(\lambda+\lambda^2+\alpha_n{}^2\right)}\exp\left(-\frac{t}{\tau_n}\right)\right] \tag{27}$$

where,

$$\tau_n=\left[\frac{\rho CL^2}{\alpha_n{}^2 k}\right],\ \lambda=\frac{Lh}{k} \text{ and } \alpha_n \text{ are the positive roots to } \alpha\tan\alpha=\lambda.$$

The steady state temperature rise at the top surface ($x=0$) of the wafer is then given by

$$\Delta T=\frac{Q_T}{h}\left(1+\frac{Lh}{k}\right)=\frac{Q_T}{h}+\frac{Q_T}{\frac{k}{L}} \tag{28}$$

The first term in the right hand side of Eq. 28 defines the temperature drop across the intervening media while the second term defines the drop across the silicon thickness. It should be noted that $\frac{Lh}{k}<<1$ due to high thermal conductivity of silicon.

Only the first root α_1 is important in Eq. 27 and can be expresses as

$$\alpha_1 = \left(\frac{Lh}{k}\right)^{\frac{1}{2}} \tag{29}$$

Substituting Eq . 29 in Eq. 27 will yield the temperature transient characteristic at the top surface of the silicon wafer during temperature rise and can be expressed as

$$T_0(t) - T_0(0) = \frac{Q_T}{h}\left[1 - \exp\left(-\frac{t}{\tau}\right)\right] \tag{30}$$

where,

the thermal time constant τ is given as $\tau = \frac{\rho CL}{h}$.

When plasma is turned off, the wafer temperature will fall exponentially and can be expressed as

$$T_0(t) = T_0 \exp\left(-\frac{t}{\tau}\right) \tag{31}$$

where,

T_0 is the steady state temperature of the wafer.

The thermal time constants and the ratio of temperature drop across the silicon wafer to total temperature drop are plotted in Figure 66 as a function of the heat transfer coefficient (h) between the wafer and water cooled electrode. During plasma etching, the heat transfer coefficients can range from 8 to 100 J/m^2-s-K (see Sections 5.5.2). Thus, the temperature drop across the thickness of the wafer is always very small as compared with total temperature rise and a constant temperature across the thickness of silicon wafer can be assumed.

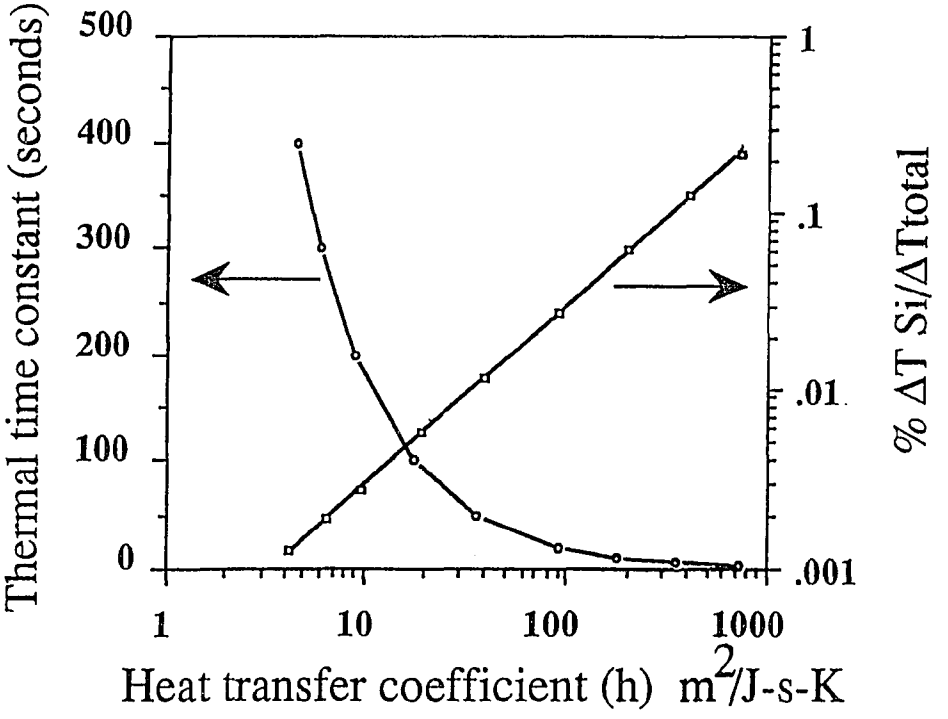

Figure 66 Thermal time constants and the ratio of temperature drop across the silicon wafer to total temperature drop as a function of the heat transfer coefficient (h) between the wafer and water cooled electrode.

5.5.2 Experimental Results and Discussion

Figure 67 shows typical waveforms of the infrared signal during plasma etching of a plain Si wafer in Ar plasma. After converting the detected signal into temperature, the thermal time constants can be measured and heat transfer coefficient can be calculated. In plasma etching situations, the gas pressure has a pronounced influence on the loss of heat and plays a major role in controlling the steady state wafer temperature. For the pressure range used in plasma etching, the heat transfer coefficients are strongly dependent on the gas pressure. Figure 68 shows the normalized waveforms of detected signal for various gas pressures during heating of an unclamped Si wafer in an Ar plasma and cooling after the plasma is turned off The estimated heat transfer coefficient was found to change from 8 to 20 J/m^2-s-K for the pressure range of 10 to

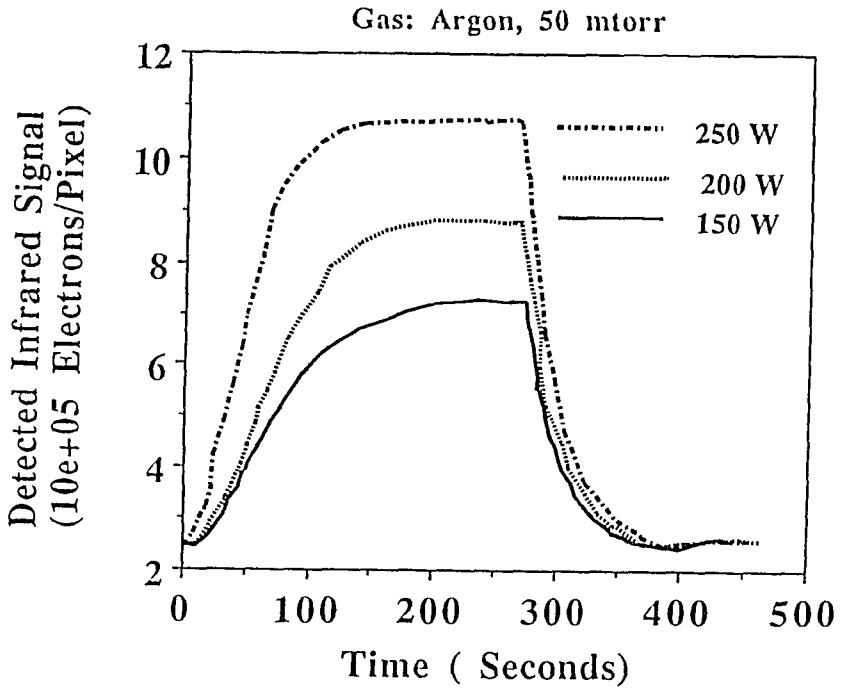

Figure 67 Typical waveforms of the infrared signal during plasma etching of a plain Si wafer in Ar plasma.

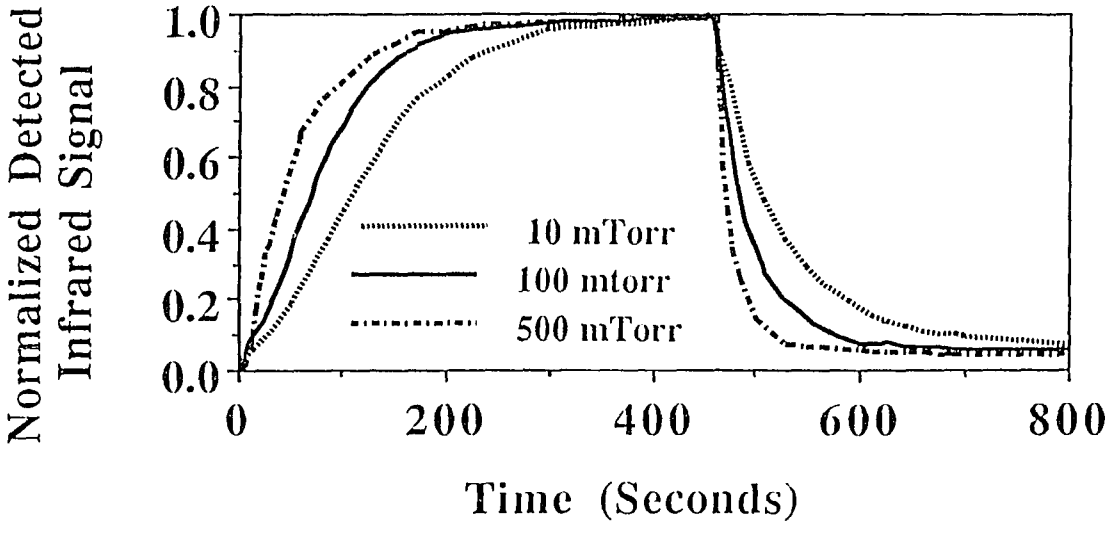

Figure 68 Effect of pressure on heat transfer characteristic for unclamped wafer.

500 mTorr. In plasma etching, the distance between the wafer and the chuck is much smaller than the mean free path of gas molecules. The heat transfer coefficient in this case can be given by:

$$h = a\Lambda_0 p, \tag{32}$$

where,

a -is the accommodation coefficient;

Λ_0 -is the conduction constant of the gas; and

p- is the gas pressure.

The accommodation coefficient and conduction constant only weakly depend on pressure[111] and the changing pressure will have a nearly linear effect on heat transfer coefficients if the radiation losses can be neglected.

Figure 69 illustrates the effect of flow-rate on heat transfer characteristics. It can be seen from the figure that changing the Ar flow-rate from 10 sccm to 100 sccm has almost no effect on the thermal time constants and the heat transfer is nearly independent of the flow rate. This result also supports the argument of neglecting the heat loss via gas heating used in the theoretical model.

5.5.3 Gas-Back-Cooled Chuck

As discussed in Section 5.5.2, the wafer temperature can rise above the photoresist thermoplastic flow temperature using moderate powers if there is no provision for good thermal contact between the wafer and the water-cooled electrode. A recent trend in the design of plasma etching reactor is to apply helium gas back-side cooling to the wafers for controlling the wafer temperature by increasing the value of heat transfer coefficient. Unfortunately, this approach complicates the design of reactors and adversely affects the throughput of the etcher. Characterization of He-backside cooling scheme is useful for gaining basic understanding leading to improved designs.

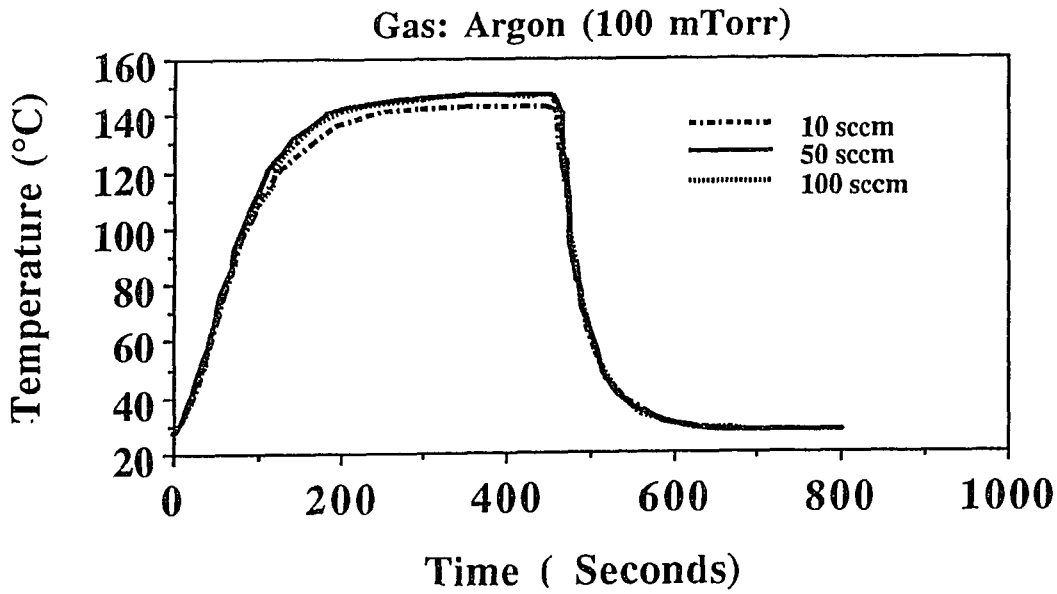

Figure 69 Effect of flow-rate on heat transfer characteristics.

A gas-back-cooled chuck was constructed to provide reproducible and controllable heat transfer. Figure 70(a) illustrates the construction of the chuck. Thermal imaging tests indicated uniform temperature across the wafer. Figure 49(b) shows typical waveforms of infrared signal emitted during the test. A total temperature rise of $\Delta T = 30$ °C was obtained for the case of wafer directly placed on water-cooled chuck and was reduced to $\Delta T = 5$ °C and $\Delta T = 3$ °C for the cases of N_2 and He back cooling (@ 10 Torr), respectively. Thus, He provides a better conductive medium than N_2 due to its high thermal conductivity. It is also interesting to note that two thermal time constants can be seen in Figure 70(b) for back-side gas cooling. The first very short time constant in the range of few seconds is due to the improved heat transfer between wafer and water cooled-chuck. The value of heat transfer characteristics for the He gas (10 Torr pressure) was estimated to be 100 J/m^2-s-K. The second very long time constant in the range of few minutes due to the heating of the ring clamp in the plasma. It was found that the design of the ring-clamp is also very important for achieving controllable and reproducible wafer temperature.

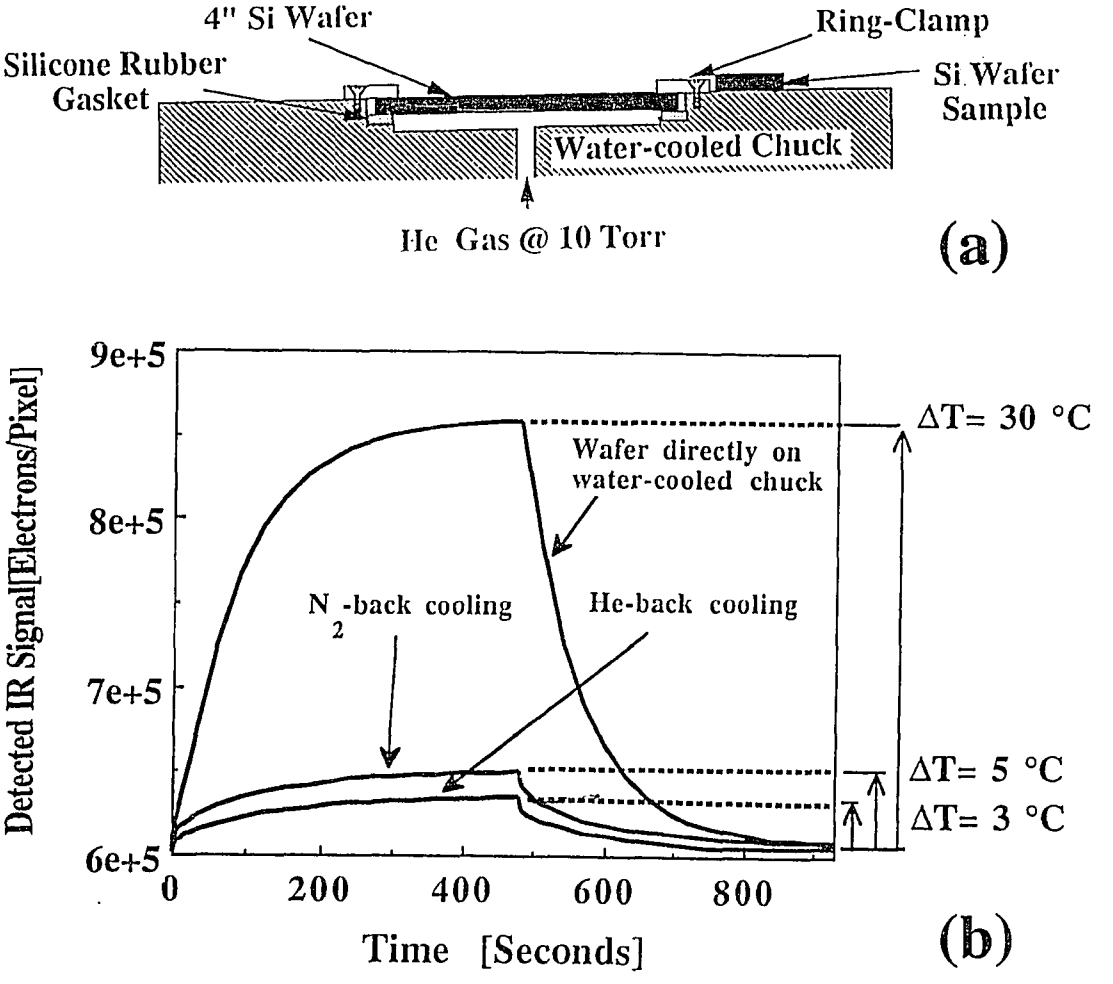

Figure 70 Gas-back-cooled chuck (a)construction and (b) typical infrared signal during the test.

5.5.4 3-D Heat Transfer Analysis

Due to very high conductivity of Si wafer, the temperature gradients across the wafer are expected to be much lower as compared to the total temperature rise. To obtain better understanding of the subject, temperature gradients across the wafer during plasma etching were estimated by simulating localized heating of 4-, 6- and 8- inch wafers using commercially available MSC-NASTRAN software (based on finite-

elements method)¥. Heat source was applied at the center or at the perimeter of the wafer to simulate the worst-case temperature profiles. The heat transfer coefficients used in this analysis were estimated from the experimental thermal imaging data.

Figure 71 shows calculated temperature profiles along the radius of the wafer at various time instants for the case in which a 10W heat input was applied in the

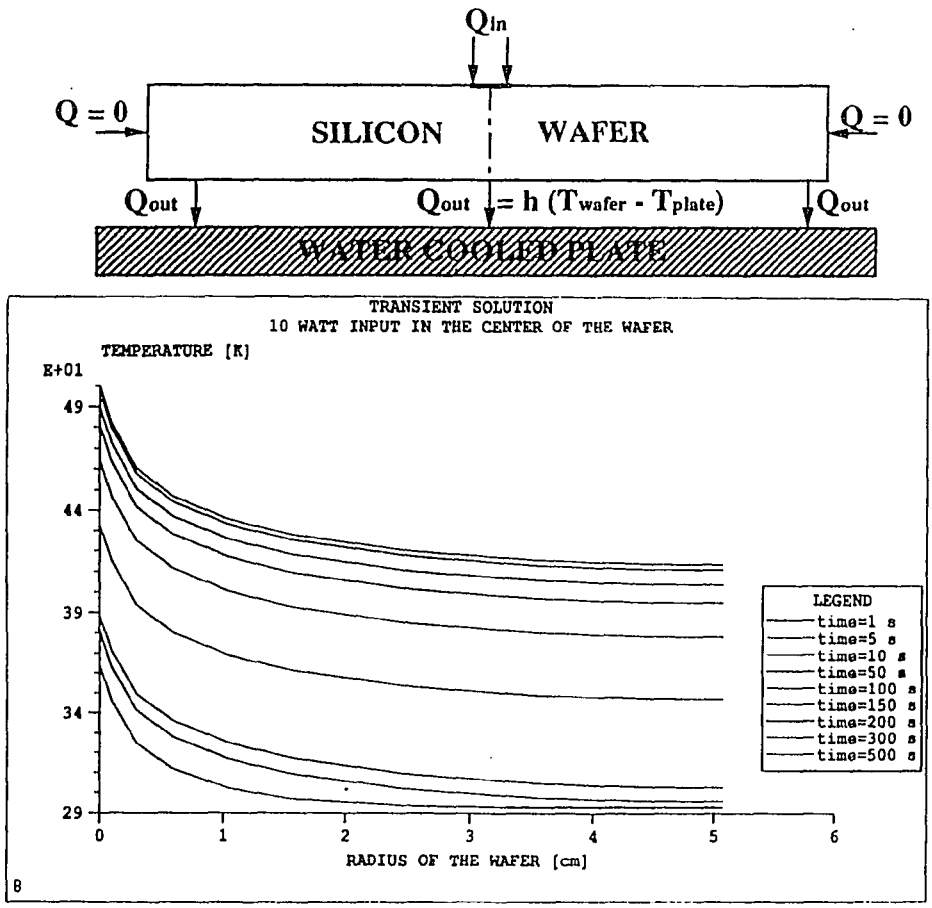

Figure 71 Calculated temperature profiles along the radius of a 4 inch wafer with a 10 W heat source applied in the center of the wafer.

¥Contributions of Helen Martinov and Michael Kaplinsky in performing 3-D heat transfer simulations are greatly appreciated.

center (2 mm in diameter) of a 4 inch wafer. In this case, heat transfer coefficient between the wafer and the water cooled plate was assumed to be h= 10J/s-m^2-K. As can be seen from the figure, the steady-state temperature profile in radial direction was reached in a very short time (<5 seconds). The wafer temperature continued to rise and reached steady-state after 300 seconds. Such a transient behavior is due to much higher value of thermal conduction coefficient of silicon than that of the heat transfer coefficient between the wafer and the water-cooled plate. The steady-state temperature difference between the center and the edge of the wafer was found to be 55°C as compared to the total temperature rise of 210° C in the center of the wafer. It should be noted here that this kind of extreme situations are very unlikely to occur during plasma etching and the wafer temperature gradients are expected to be much smaller during plasma etching conditions.

Temperature profiles in the wafer are expected to be strongly dependent on the value of the heat transfer coefficient, h. Figures 72(a) and 72(b) illustrate the simulated temperature profiles for various time instants for the case of h=10 J/s-m^2-K (representing the case of uncooled wafer) and h=100 J/s-m^2-K(representing the case of He back-side cooling), respectively. In this case, a 40W heat source was applied to the periphery of an 8-inch wafer. The analysis of these figures show that the increased value of h leads to higher temperature gradients in the radial direction of the wafer and lower steady state temperature. Due to larger area of the wafer in this case, the steady-state temperature profile in radial direction was reached in about 10 seconds.

In summary, the temperature profiles in the radial directions were found to be strongly dependent on the geometry of the heat source. The time constant for establishing a radial temperature gradient was found to be less than 4.0 seconds for both values of h. Time constants for reaching the final temperature was about 100 seconds and for h= 10 J/s-m^2-K and 10 seconds for h=100 J/s-m^2-K.

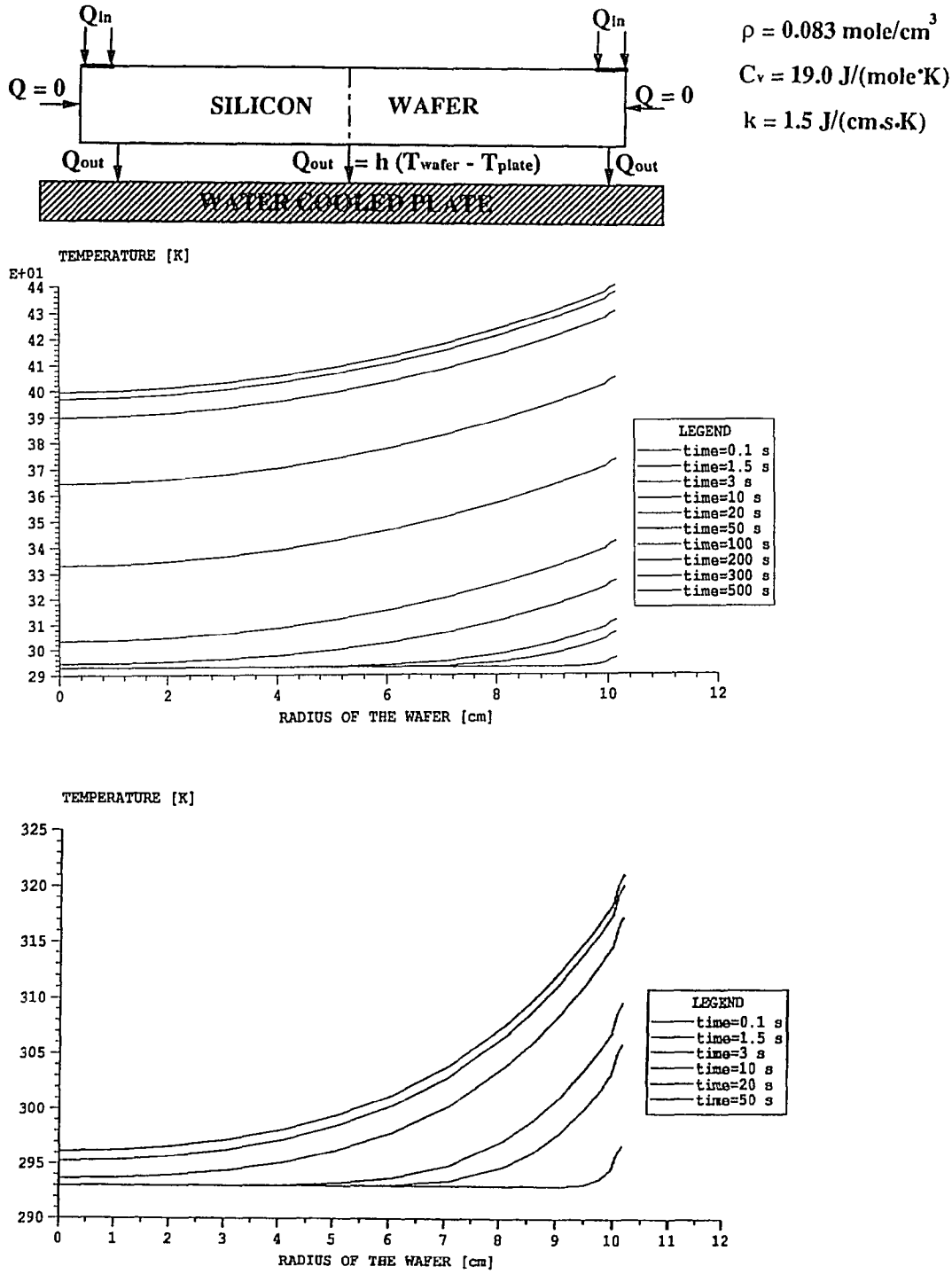

Figure 72 Calculated temperature profiles along the radius of an 8 inch wafer with a 40W heat source applied at the periphery of the wafer for h=10 J/s-m^2-K in (a) and h=100 J/s-m^2-K in (b).

5.6 Limitations for the Applicability of the Technique

A major limitation of the applicability of the thermal imaging technique into production is the present cost of the thermal imaging systems requiring cryogenic cooling. However, recent developments in the room-temperature monolithic thermopile technology[112] is expected to lower the cost of imagers in few years. Another limitation of this broad-band imaging technique is the accuracy of temperature measurements which can be overcome by using a multiple-wavelength monitoring approach.

5.7 Summary

Thermal imaging represents a very promising approach for providing real-time two-dimensional spatial information of the etch-process that can be used for monitoring as well as controlling the operation of advanced etch tools. In addition, thermal imaging was also found to be an effective diagnostic tool for studying some of the basic etching processes and for design and development of new reactors. This approach has a potential of being applied for process monitoring and control in CVD, RTP as well as sputtering systems.

CHAPTER 6
CONCLUSIONS AND RECOMMENDATIONS

6.1 Conclusions

Several useful contributions have been made in the area of plasma processing, ranging from research-oriented measurements of plasma properties for developing a fundamental understanding of plasma processes and various reactor geometries to application-oriented development of a diagnostic tool for process monitoring and control.

Extensive mapping of plasma region in various parallel-plate reactor configurations have shown that the plasma density distribution is dramatically different for dissociative molecular gases as compared to inert gases. The plasma properties were also found to be strongly affected by the electronegativity of the process gas. The triode configuration was found to have higher ionization efficiency as compared with the diode configuration for the same total power. In the triode mode, the relative phase between the RF voltage waveforms applied to the electrodes was found to determine both the magnitude and distribution of the plasma density. Higher etch-rates and better etch-uniformity are obtained for out-of-phase excitation (180°) as compared with the in-phase excitation(0°). The effect of phase was found to be more pronounced in highly electronegative gases.

A novel magnetic enhancement scheme resulted in enhanced low pressure operation of parallel-plate tools. The grounded magnetic multipole device can be added to the diode or triode to produce a high quality etching tool while maintaining all the advantages of magnetic enhancement and simplicity of parallel-plate geometry.

The thermal imaging technique represents a very promising approach for providing real-time two-dimensional spatial information of the etch-process that can

be used for monitoring as well as controlling the operation of advanced etch tools. Furthermore, thermal imaging is also useful for measuring wafer temperature and heat transfer characteristics.

6.2 Suggested Work

Several continuations and new directions are suggested by the present thesis. The fundamental understanding developed by the scanning tuned Langmuir probe is extremely useful for discharge modeling and is directly applicable to plasma enhanced CVD reactors. Similar experimental work might be carried out in electron cyclotron resonance or inductively coupled plasma reactors. Plasma uniformity is a major concern in these reactor configurations. The magnetic multipole enhancement scheme can be easily adopted to obtain dense, uniform plasma at low pressures in these configurations. There is also a need to establish scaling laws for the multipole enhancement.

In new generation radio frequency inductively coupled or helicon source based plasma reactors, 13.56 MHz excitation is used for both the source and wafer biasing. The relative phase between the voltage waveforms applied to the source and the wafer biasing chuck is expected to determine plasma characteristics. It is essential that the effect of phase in these reactors should be to be investigated.

The thermal imaging technique has potential applications for measurement and control of temperature uniformity in RTP and CVD reactors and these applications should be investigated with appropriate radiometric techniques such as multiple wavelength imaging.

APPENDIX A

LANGMUIR PROBE DIAGNOSTICS OF PLASMAS

A.1 Introduction

Electrical measurements using a Langmuir probe are a powerful and experimentally simple mean of determining key internal discharge parameters, such as charged particle concentrations, plasma potential and electron energy distribution function (EEDF). Since the pioneering work of Irving Langmuir over sixty years ago[113], numerous papers and excellent reviews of the subject have been published.[114,115] Basically, the Langmuir probe consists of one or more small metallic electrodes and it is inserted into the plasma. Various probe configurations such single, double, triple or emissive probes have been used with probe shapes ranging from spherical, cylindrical or planner to infer plasma characteristics. However, discussion here is limited only to the theory of single cylindrical probe.

In the single probe configuration, a single electrode(typically a thin metallic wire enclosed by a ceramic sleeve) is inserted into the plasma and is attached to a power supply which can be biased positive or negative relative to the plasma. The current collected by the probe is measured as a function of the applied potential. The I-V characteristic of the probe is then used to deduce important plasma parameters as discussed below.

A.2 Basic Theory of Langmuir Probe: The Case of Cylindrical Probe

The basic theory behind a single cylindrical Langmuir probe is reviewed here. Electric probe theory is complicated due to the fact that probes are the boundaries to the plasma. Near the boundary, the equations that govern the plasma behavior change. Charge

neutrality does not hold near the boundaries and a thin layer exists where charge neutrality does not hold. The layer, often called a Debye sheath, can sustain a large electric field and the area of the sheath-plasma boundary governs the current collection characteristics.

For simplicity, plasma is assumed to be excited by a DC source and only three species of plasma particles are considered: electrons; singly charged positive ions; and neutral atoms or molecules. The electrons and ions are assumed to have Maxwellian energy distribution. Figure A.1 shows a schematic plot of a single-probe characteristics together with cross-sectional drawing of the region perturbed by the probe. The mechanism of particle collection depends on the potential, V, applied to the probe with respect to the ground. According to the magnitude and sign of the probe current, Ip, the single probe characteristics can be divided into three distinct regions.

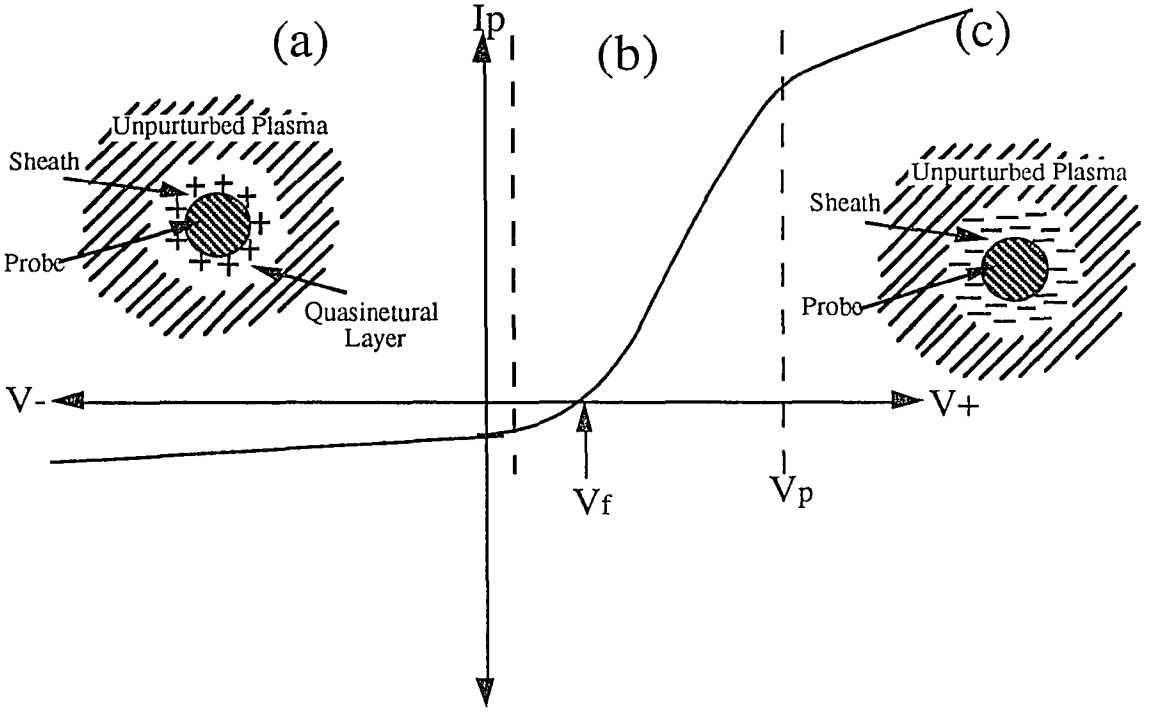

Figure A.1 Typical I-V characteristics of a single Langmuir probe.

I. Electron Retarding Region

For the purpose of quantitative description, it is easier to deal with the probe current in the transition region (region "b") in Figure A.1. The probe current in this region can be expressed as:

$$I = \frac{eN_e A}{4}\left(\frac{8kT_e}{\pi M_e}\right)^{\frac{1}{2}} \exp X \qquad \text{(A.1)}$$

where N_e is the electron density in the bulk plasma, A is the probe area, M_e is the mass of electron; and X is a dimension-less potential defined as

$$X = \frac{e(V - V_p)}{kT_e} \qquad \text{(A.2)}$$

where V is the potential applied to the probe, and V_p is the local plasma potential.

Thus, a plot of log I vs. V in this region is a straight line with slope inversely proportional to T_e.

II. Saturated Ion Current Region

For large value of negative probe potential $V<<V_p$, essentially all electrons in the vicinity of the probe are repelled and the electron current to the probe is negligible. The probe current in this region consists of only positive ion current I_i. Although I_i will, in general, continue to increase with $|V|$, this branch of the characteristics is called the ion saturation current, I_{is}, and is shown in region "a" of Figure A.1. The nature of this saturation will depend on many parameters such as, the Debye shielding length and the collisional or non-collisional nature of plasma and is difficult to describe quantitatively.

The typical low pressure plasma used in plasma etching (1 to 200 mTorr) can be considered to be collisionless, i.e., the mean free path for charged particle-neutral

collision is of the order of 0.1 cm and thus much larger than the Debye length λ_D which is of the order of 10^{-2} cm. Furthermore, the ions in the bulk plasma are close to room temperature (~0.1eV), whereas T_e is typically few eV. Laframboise[116] has done rigorous analysis of this kind of plasma and he represented the ion current as

$$I_i = eN_i A\left(\frac{kT_e}{2\pi M_i}\right)^{\frac{1}{2}} i_i \qquad \text{(A.3)}$$

where N_i is the ion density in the bulk plasma, M_i is the ion mass, and i_i a dimensionless current depending on r_p/λ_D and on the potential X, but only weakly on the ion temperature T_i . Moreover, from Laframboise's results, Steinbruchel[117] has shown that as long as $r_p/\lambda_D < 3$ and $T_i/T_e << 1$

$$i_i^2 = 1.27(-X) \qquad \text{(A.4)}$$

to within about 3%. Thus, $I_i{}^2$ is a linear function of the probe potential V with a slope determined by the ion density N_i as

$$\frac{-\Delta(I_i^2)}{\Delta V} = \frac{0.020e^3 N_i^2 A^2}{M_i} \qquad \text{(A.5)}$$

Also, the plasma potential can be determined by extrapolating $I_i{}^2$ to zero.

III. Electron Saturation Region

The region where $V>Vp$ is known as electron saturation region and is shown in region "c" of Figure A.1. When $V>Vp$, a space charge field is set up adjacent to the probe that accelerates electrons toward the probe and repels ions. Ion current to the probe will decrease very rapidly due to its heavy mass when V is increased above Vp. Increasing V

should also have relatively little effect on the electron current since it would be limited by the random flux entering the accelerating field of the probe. Unfortunately, changing potential applied to the probe will change the area of sheath-plasma boundary upon which random flux of electrons is incident. Also, driving the probe into electron saturation region may draw significant amount of electron current and cause significant perturbation of the properties of plasma in the vicinity of the probe. The detailed analysis of this region is very complicated and is not widely used to infer plasma properties.

The probe method has not been fully developed for diagnosis of plasmas containing negative ions. Interpretation of probe measurements for plasmas containing negative ions is more complex due to the fact that two(or more) negative species are present in the plasma and their masses are drastically different. Amemiya[118] has recently reviewed the present status of Langmuir probe theory applicable to plasmas with negative ions.

A.3 Langmuir Probe Measurements of RF Discharges

In 13.56 MHz frequency discharges commonly used in plasma etching, ions can not respond to the instantaneous field and only respond to a time-averaged field. However, electrons have small mass and they can respond to the instantaneous field. The plasma potential fluctuates with time in the RF discharge. The amplitude of these fluctuations can exceed T_e (eV). Thus, if a probe is maintained at a fixed DC bias, the fluctuating voltage across the probe-plasma sheath results in the collection of a time-varying current. Since the variation of the plasma potential with time is generally unknown, the instantaneous probe current can not be used to infer plasma parameters.

The basic theory of the probe characteristics in presence of RF interference is described by Paranjpe[42] and is reviewed here. The expression of the instantaneous probe current in the electron retardation regime can be written as

$$I(t) = I_e(t) - I_p - I_d(t), \tag{A.5}$$

where

I_e is the electron current;

I_i is the positive ion current; and

$I_d(t)$ is the displacement current due to probe-plasma capacitive sheath.

The displacement current $I_d(t)$ can be expressed as

$$I_d = A_p \varepsilon_o \frac{dE}{dt} + A_g \varepsilon_o \frac{dE}{dt}, \tag{A.6}$$

In the above expression, A_p and A_g are the plasma contact areas to the probe and the surrounding insulated sleeve supporting the probe, respectively; E is the electric field at the surface and ε_o is the permitivity of the space.

The instantaneous electron current $I_e(t)$ is dependent on the instantaneous sheath potential drop, while positive ions respond only to the time- averaged sheath potential. During most part of the cycle, the displacement current dominates the total probe current and thus very little useful information can be obtained by the instantaneous probe current. Instead the dependence of time averaged probe current will yield useful plasma parameters.

The time averaged total current can be expressed as

$$\bar{I} = \bar{I}_e - I_i - \bar{I}_d,$$

where

$$\bar{I}_e = \frac{eA_p N_e \bar{C}_e}{4T} \int_0^T \exp\left(\frac{V(t) - V_p(t)}{T_e}\right) dt, \tag{A.7}$$

$$\bar{I}_d = 0.$$

In the above expression, $\overline{C}_e$ is the electron mean thermal speed, T_e is the average electron temperature, T is the period of the cycle and $V(t)$ and $Vp(t)$ are the instantaneous probe and plasma potentials, respectively. The time-varying space potential is governed by the discharge operating conditions and is not perturbed provided the probe is operating in the electron retarding regime. The probe and plasma potentials can be expressed as

$$V(t) = V_{dc} + V_{ac}(t),$$
$$V_p(t) = V_{pdc} + V_{pac}(t). \tag{A.8}$$

The time averaged electron current in Eq. A.7 may also be expressed as

$$\bar{I}_e = \frac{reA_pN_e\overline{C}_e}{4}\exp\left(\frac{V_{dc} - V_{pdc}}{T_e}\right) \tag{A.9}$$

where

$$r = \frac{1}{T}\int_0^T \exp\left(\frac{V_{ac}(t) - V_{pac}(t)}{T_e}\right)dt \tag{A.10}$$

The time averaged sheath potential is given by the difference between the time averaged probe (V_{dc}) and plasma (V_{pdc}) potentials. The time averaged probe potential corresponding to the condition of zero time-averaged probe current is defined as the floating potential (V_f) of the plasma. Equating the expression for I to zero, the following relationship for V_f can be obtained:

$$V_f = V_{pdc} - T_e \ln\left(\frac{reA_pN_e\overline{C}_e / 4}{I_i}\right) \tag{A.11}$$

In general, $r>1$ and is equal to unity for the special case $V_{ac}(t)=V_{pac}(t)$. Thus, as the RF voltage across the sheath $[V_{ac}(t)-V_{pac}(t)]$ increases, r decreases and the apparent floating potential decreases. Since $r>1$ in presence of an RF voltage across the sheath, the inferred electron temperature is higher than its true value; whereas, the inferred electron number density is lower than its true value. As the RF voltage across the sheath increases, the apparent floating potential decreases. The probe may be driven from electron saturation to ion saturation during the cycle and no simple theory can account for the distortion of the probe characteristics due to the RF interference.

Several techniques have been developed to mitigate the problems of RF interference. Intuitively, the simplest approach consists of filtering the probe characteristics leading to a time averaged characteristics. The time-averaged characteristics does not correspond to the true characteristics because of the strong non-linearity of the characteristics. The floating double probes can be used to combat RF interference[119]. Conversely, it is often difficult to completely float the DC voltage supply and RF fields distort the probe characteristics.

Other schemes rely on minimizing the RF voltage across the sheath, either by driving the probe with an RF voltage or by increasing the impedance between the probe and ground so that the probe tip automatically follows the time-varying plasma potential. In the first approach, an RF signal matched in amplitude and phase to the local time varying plasma potential is applied to the probe so that only pure DC bias exists between the probe and the plasma.[120] However, any mismatch between the probe and plasma potential waveforms due to differences in harmonic contents can cause error. Also, the experimental arrangement is very complex because typically an attenuated signal from the powered electrode is passed through a variable phase shifter and variable gain amplifier before being applied to the probe. The phase and amplitude are adjusted so that the floating potential of the probe is maximized. In an another approach, two probes are

used. One probe acts as a Langmuir probe while the other functions as a high input impedance probe that is used to sample the instantaneous plasma potential which is fed to the first probe via a unity gain amplifier.

A more simple approach is minimize the RF voltage across the sheath by making the impedance between the probe and ground much larger than that of sheath. The tuned Langmuir probe technique, developed by Paranjpe[42], can achieve this using extremely simple hardware. A modified version of this technique is used to infer plasma parameters in this thesis and operational details of the modified tuning circuit are described below.

The equivalent circuit of the modified tuned probe configuration is shown in Figure A.2. The plasma can be represented by a DC voltage source in series with an RF voltage source. C_S and R_S are the capacitance and resistance associated with the plasma-probe sheath and are represented by a combined impedance Z_1. If the impedance represented by the capacitance between the probe and the chamber walls is smaller than

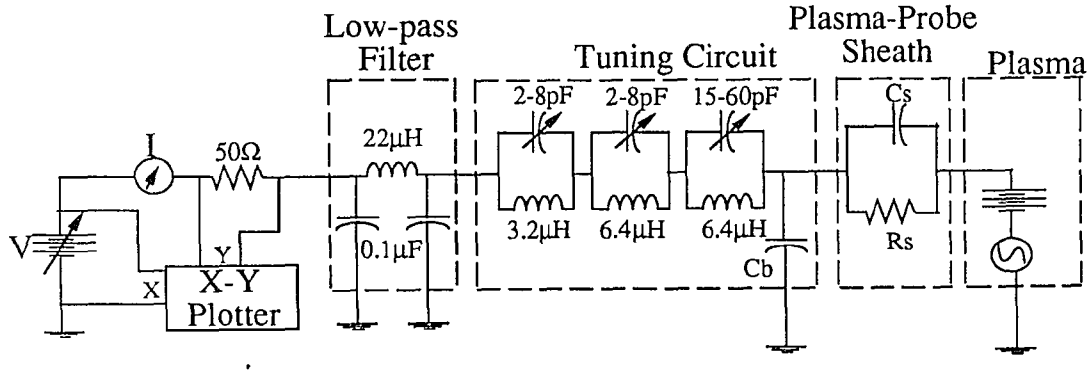

Figure A.2 Circuit diagram of the modified tuned Langmuir probe.

Z_1, most of the RF voltage will appear across the sheath and will perturb the probe characteristics. If a tuning network is added to the probe, it is possible to increase the impedance Z_2 representing the combined impedance of the probe-chamber wall capacitance, C_b, and the tuning network by forming a parallel-resonant circuit. Z_2 can be increased by the Q factor of the resonant circuit by tuning the inductor or capacitor. Now $Z_1 << Z_2$ and most of the RF will appear across the impedance Z_2. It was found that the second and third harmonic of the fundamental RF frequency plasma can also distort the probe characteristics significantly. Thus, the tuning network circuit was modified and can simultaneously be tuned to generate resonance at the fundamental as well as second and third harmonics of the fundamental 13.56 MHz frequency. The design of the circuit along with the component values are also shown in Figure A.2. A low-pass filter circuit is added to the tuning circuit to reduce RF pick-up noise.

The resonance in presence of RF discharge is detected by tuning the capacitors to maximize the floating point potential. Once the probe is tuned for particular plasma condition, data were taken.

APPENDIX B

PLASMA ETCHING END-POINT DETERMINATION BY PLASMA IMPEDANCE MONITORING

B.1 Introduction

As increasing accuracy of etching is required, it is necessary to have an *in situ* tool that automatically determines an accurate end-point for the etch. The change in plasma impedance at the end-point of etching can be utilized to develope an end-point detection scheme. The plasma impedance monitoring technique eliminates the need for optical windows or extensive system modification and can be easily adopted for automation. However, little work has been reported in the area of plasma impedance monitoring for end-point detection[121,122] All of these studies were performed on basic diode reactor and were limited to monitoring peak-to peak voltage, absolute impedance or change in reflected power. Also, experimental arrangement for these measurements were not described in detail.

In this Appendix, a new end-point detection technique based on monitoring the change in plasma impedance associated with the change in plasma composition is described. It was found that end-point conditions are clearly indicated by any of the electrical parameters (induced bias, RF current, RF voltage and phase) as measured at the powered electrode(s). The application of this technique is demonstrated for polycrystalline silicon (polysilicon) and Si_3N_4 etching in an SF_6 plasma and photoresist stripping in an O_2 plasma in the diode, triode and magnetically enhanced triode reactor configurations.

B.2 Experimental Setup

The reactor stand configuration and the electrical block diagram of power connections to each electrode are shown in Figure B.1. The pressure in the process chamber is controlled by an MKS automatic throttle valve and is monitored by a Baratron capacitance manometer. In the triode configuration, the electrodes are powered by two dependent 1 KW RF (13.56 MHz) power supplies. The RF power amplifiers are linked to each other and are powered by a common crystal oscillator. A time delay network is placed in series with the upper electrode amplifier input. The electrical phase of one electrode relative to the other at the operating frequency of 13.56 MHz can be adjusted over 360 degrees. The system was operated in a parallel-plate diode mode by grounding the upper electrode. The matching networks consist of an "L" configuration, having a shunt capacitor for loading and a fixed coil inductor and a series capacitor for tuning. The power to each electrode is measured using Bird wattmeters in the 50-ohm feed lines to the matching networks. The system is capable of being configured in a diode (by grounding one electrode), triode (two powered electrodes with the chamber wall as the grounded electrode) or magnetic multipole enhanced triode configurations. A detailed description of the magnetic multipole enhanced triode reactor configuration is given in Chapter 4.

Two 8" diameter water-cooled RF electrodes are mounted on the upper and lower plates. The distance between the plates is adjusted to 2.6 inches for this experiment. Identical RF matching networks are mounted on the upper and lower plates of the vacuum chamber and are coupled directly to the two electrodes. The RF voltage(V_{p-p}) on each electrode is measured by a high voltage probe (Tektronix P6015 ;1000X) connected to the RF feed-through line very close to the electrode to minimize the stray impedance effects. The RF current (I) is measured by an RF high frequency toroidal current probe (IPC CM-10-MG) connected in the similar manner. The RF

current, RF voltage and phase angle(θ)between them is monitored on a Hewlett-Packard Vector Voltmeter (Model 5405A). The DC voltage signals proportional to the above quantities from the output of the vector voltmeter are fed to a strip chart recorder to provide a visual record of the etch cycle. A He-Ne laser (6326 Å) based reflection interferometer is also installed for measuring film-thickness as a function of time and is used as the standard for end-point detection in the above described experiments.

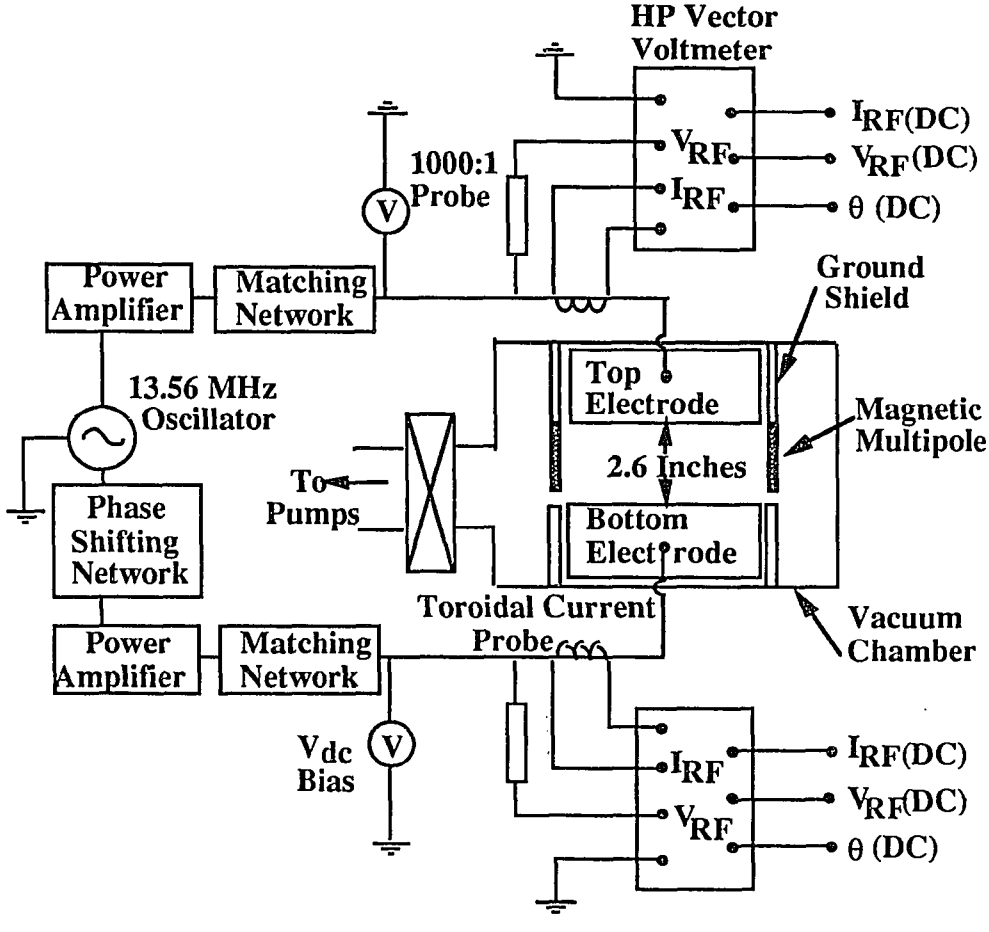

Figure B.1 A schematic diagram of the test consisting electrical block diagram of the power supplies and connection to each electrode.

B.3 Results and Discussion

After a discharge is initiated, the matching network is tuned for maximum power transfer to the plasma load. The tuning procedure compensates the electrically reactive components in the plasma and sets a fixed phase angle between the RF voltage and current supplied to the electrode(s) and load. After tuning, any changes in the steady-state plasma due to changes in etching chemistry will cause θ and the magnitude of I and V_{p-p} to vary. Due to capacitive coupling to the plasma, the induced DC bias, V_{dc}, on both of the electrodes will also vary with the etching chemical changes.

Figure B.2 illustrates end-point detection by plasma impedance (V_{p-p}, I, V_{dc} and θ) monitoring during Si_3N_4 etching on Si in a diode configuration. The measurements

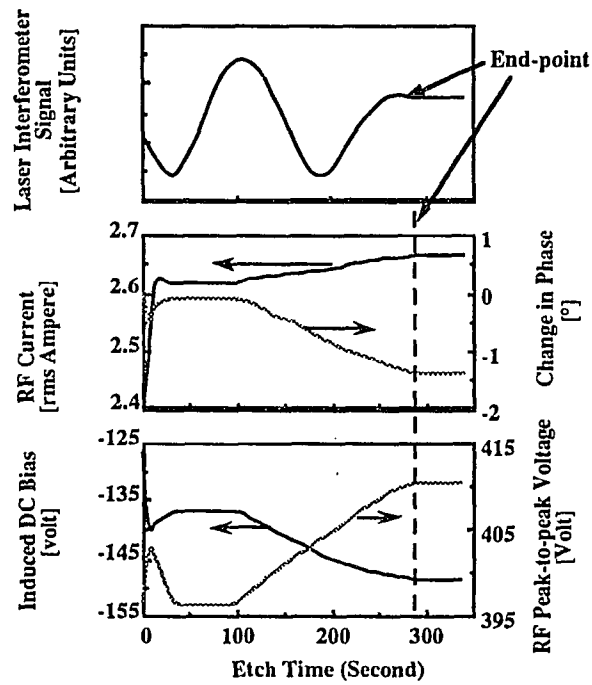

Figure B.2 End-point detection of etching Si_3N_4 on Si in a diode configuration in an SF_6 plasma.

are made on the lower electrode and the upper electrode of this system is grounded. The power to the lower electrode is set at 100W to produce plasma at 15 mtorr. The initial variation in the measured electrical parameters is due to the time required to reach a steady-state discharge condition. The plasma species concentration will change at the completion of etching of Si_3N_4 layer forcing the electrical parameters to change. As shown in Figure B.2, all the measured electrical parameters reflect these changes. The transition time to reach the next steady-state condition is a qualitative measure of the areal non-uniformity in the etching. The laser interferometer detects the end-point prior to the detection of it by the plasma impedance monitoring technique due to this non-uniformity, that is, the laser interferometer provides information from only a small area of the wafer limited by the laser beam diameter. Note that the electrical parameter changes correlate well with the interface or end-point as determined by the laser interferometer measurements.

Figures B.3 and B.4 demonstrate the end-point detection for plasma etching of polysilicon on an oxidized Si wafer in an SF_6 plasma using the triode configuration and photoresist stripping on aluminum coated Si wafer in an O_2 plasma using a magnetically enhanced triode configuration, respectively. The power to each electrode is set at 100W/electrode to produce plasma at 15 mtorr pressure. The excitation voltage phase difference between the upper and the lower electrode was set to $\phi = 180°$. The measurements of $V_{p\text{-}p}$, I, V_{dc} and θ were made on the upper electrode. Again, these parameters correlate well with the end-point as determined from the laser interferometer measurements. These electrical parameters vary in a similar fashion on the lower electrode. End-point was successfully detected by monitoring the electrical parameters on the lower electrode for the same reactor configurations.

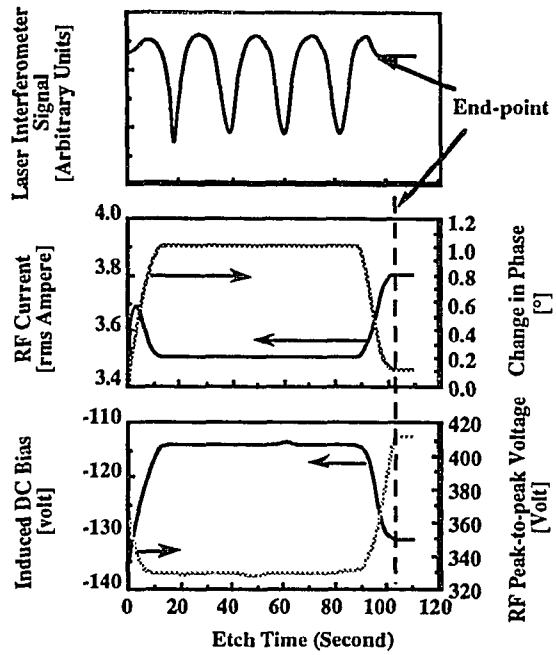

Figure B.3 End-point detection of etching polysilicon on oxidized Si in a triode configuration in an SF_6 plasma.

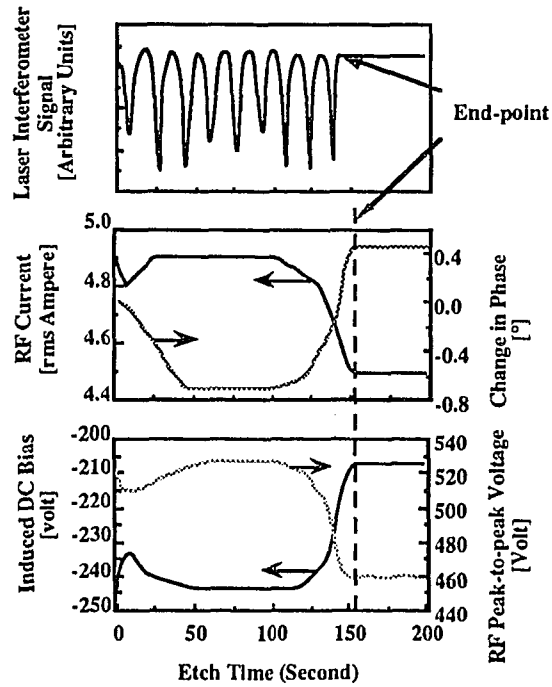

Figure B.4 End-point detection of stripping photoresist on aluminum coated Si in a magnetically enhanced triode reactor in an O_2 plasma.

A number of studies have reported techniques to measure true plasma impedance[123,124] but they are very difficult to implement in real-time. It is not necessary to quantitatively measure the plasma impedance to use these parameters for the purpose of end-point detection. However, the overall sensitivity of this technique does depend on stray losses associated with the construction of the electrodes, ground shields and chamber. The signal to noise ratio can be increased by using standard offset and gain enhancement. Since the end-point detection is based on a transition from one steady state plasma condition to another, the sensitivity of the detection can be further enhanced by measuring the first derivative of the signal(s).

B.4 Summary

In summary, $V_{p\text{-}p}$, I, V_{dc} and θ monitoring of an etching plasma discharge can serve as an accurate, simple and inexpensive end-point detector. This method has been successfully tested on different reactor configurations and material systems. It negates the need for optical ports and is easily adaptable to automation.

REFERENCES

1 E. Fisher and P. B. Armentrout, "Kinetic Energy Dependence of the Reactions of O^+ and O_2^+ with CF_4 and C_2F_6," *J. Phys. Chem.*, **95**, pp. 6118-6124 (1991).

2 A. T. Hell, "Spatial Distribution of Electron Density and Electric Field Strength in a High-Frequency Discharge," *Ind. Chem. Eng. Fundam.*, **9**, pp. 160-166 (1970).

3 M. J. Kushner, "Mechanisms for Power Deposition in Ar/SiH_4 Capacitively Coupled RF Discharges," *IEEE Trans. on Plasma Sci.*, **PS-14**, pp. 188-196 (1986).

4 Smirnov B. M., *Physics of Weakly Ionized Gases* (Mir, Moscow, 1981).

5 H. S. Butler and G. S. Kino, "Plasma Sheath Formation by Radio-Frequency Fields," *Phys. Fluids*, **6**, pp. 1346-1355 (1963).

6 K. Riemann, "Theoretical Analysis of the Electrode Sheath in RF Discharges," *J. Appl. Phys.*, **65**, pp. 999-1004 (1989).

7 M. A. Liberman, "Dynamics of a Collisional, Capacitive RF Sheath," *IEEE Trans. on Plasma Sci.*, **PS-17**, pp. 338-341 (1989).

8 D. Vender and R. Boswell, "Electron-Sheath Interaction in Capacitive Radio-Frequency Plasmas," *J. Vac. Sci. Technol. A*, **10**(4), pp. 1131-1138 (1992).

9 P. M. Vallinga, P. M. Meijer and F. J. de Hoog, "Sheath Properties of RF Plasmas in a Parallel Plate Etch Reactor; the High Frequency Regime," *J. Phys. D: Appl. Phys.*, **22**, pp. 1650-1657 (1989).

10 G. R. Misium, A. J. Lichtenberg and M. Liberman, "Macroscopic Modeling of Radio Frequency Plasma Discharges," *J. Vac. Sci. Technol. A*, **7**(3), pp. 1007-1013 (1989).

11 D. E. Bohm, "Minimum Ionic Kinetic Energy for a Stable Sheath," in *The Characteristics of Electrical Discharges in Magnetic Fields*, edited by A. Guthrie and R. K. Walkerling (McGraw-Hill, 1949).

12 F. F. Chen, *Introduction to Plasma Physics and Controlled Fusion*, Vol. 1, 2nd Ed. (Plenum Press, New York, 1984).

13 J. Meichsner, H. U. Poll and K. H. Wixkleder, "Negative Ions in a Glow Discharge of Tetrafluoromethane," *Contrib. Plasma Phys.*, **25**(5), pp. 503-512 (1985).

14 N. St. J. Braithwaite and J. E. Allen, "Boundaries and Probes in Electronegative Plasmas," *J. Phys. D: Appl. Phys.*, **21**, pp. 1733-1737 (1988).

15 R. Gottscho, "Glow-discharge Sheath Electric Fields: Negative-ion, Power, and Frequency Effects," *Phys. Review A*, **36**(5), pp. 2233-2240 (1987).

16 B. Chapman, *Glow Discharge Processes*, Chapters 4 and 5 (John Wiley & Sons, New York, 1980).

17 H. R. Koenig and L. I. Maissel, "Application of RF Discharges to Sputtering," *IBM J. Res. Develop.*, **14**, pp. 168-171 (1970).

18 J. Maher (GS-DRYTEK), private communication.

19 C. M. Horwitz, "RF Sputtering-Voltage Division Between Two Electrodes," *J. Vac. Sci. Technol. A*, **1**, pp. 60-68 (1983).

20 G. Smolinsky and M. Vasile, "Ionic and Neutral Products of an RF Discharge in Methane," *Int. J. Mass Spectrom. Ion Phys.*, **16**, pp. 137-142 (1975).

21 M. A. Liberman and S. E. Savas, "Bias Voltage in Finite Length, Cylindrical and Coaxial Radio Frequency Discharges," *J. Vac. Sci. Technol. A*, **8**, pp. 1632-1641 (1989).

22 Y. P. Song, D. Field and D. Klemperer, "Electrical Potentials in RF Discharges," *J. Phys. D: Appl. Physics.*, **23**, pp. 673-681 (1990).

23 G. Rogoff, "Ambipolar Diffusion Coefficients for Discharges in Attaching Gases," *J. Phys. D: Appl. Phys.*, **18**, pp. 1533-1545 (1985).

24 D. Flamm, V. M. Donnelly and J. Mucha, "Reaction of Fluorine Atoms With Silicon," *J. Appl. Phys.*, **52**, pp. 3633-3640 (1981).

25 J. W. Coburn and H. F. Winters, "Ion and Electron Assisted Gas Surface Chemistry- An Important Effect in Plasma Processing," *J. Appl. Phys.*, **50**, pp. 3189-3194 (1979).

26 E. Kay, J. Coburn and A. Dilks, "Plasma Chemistry of Fluorocarbons as Related to Plasma Etching and Plasma Polymerization," *Topics Current Chem.*, **94**, pp. 1-9 (1980).

27 R. d'Agostino, F. Cramarossa, S. DeBenedictis and G. Ferraro, "Spectroscopic Diagnosis of CF_4-O_2 Plasmas During Si and SiO_2 Etching Processes," *J. Appl. Phys.*, **52**, pp. 1259-1265 (1981).

28 L. Ephrath, "Dry-Etching for VLSI- A Review," *J. Electrochem. Soc.*, **129**, pp. 2282-2287 (1982).

29 V. Donnelly and D. Flamm, "Effects of Frequency on Optical Emission, Electrical, Ion, and Etching Characteristics of a Radio Frequency Chlorine Plasma," *J. Appl. Phys.*, **58** (6), pp. 2135-2144 (1985).

30 G. J. Gorin, U. S. Patent No. 4,464,223 (August, 1984).

31 D. Flamm and G. Herb in "*Plasma Etching: An Introduction*," edited by D. Mannos and D. Flamm, Ch. 1, pp. 37 (Academic Press, Inc, San Diego, 1989).

32 S. M. Sze, "*Semiconductor Devices, Physics and Technology*," Chapter 8, pp. 336 (John Wiley & Sons,, New York, 1985).

33 E. Gogolides, J. Nicolai and H. Sawin, "Comparison of Experimental Measurements and Model Predictions for Radio-Frequency Ar and SF_6 Discharges," *J. Vac. Sci. Technol. A*, **7**(3), pp. 1001-1006 (1989).

34 J. Boeuf, "Numerical Model for RF Glow Discharges," *Phys. Rev. A*, **36**(6), pp. 2782-2792 (1987).

35 E. Bogle-Rohwer, D. Gates, L. Hayler, H. Kurasaki and B. Richardson, "Wall Profile Control in a Triode Etcher," *Solid State Technol.*, **28**(4), pp. 251-254 (1985).

36 H. Goto, H. Lowe and T. Ohmi, "Independent Control of Ion Density and Ion Bombardment Energy in a Dual RF Excitation Plasma," *IEEE Transaction on Semiconductor Manufacturing*, **6**(1), pp. 58-64 (1993).

37 J. H. Thomas II and B. Singh, "Effect of the Radio-Frequency Voltage Phase in a Balanced Triode Plasma Etching Reactor," *J. Vac. Sci. Technol. A*, **10**(5), pp. 3070-3075 (1992).

38 H. C. Sun, E. A. Whittaker, Y. W. Bae, C. K. Ng, V. Patel, W. H. Tam, S. McGuire, B. Singh and B. Gallois, "Combined Wavelength and Frequency Modulation Spectroscopy: A Novel Diagnostic Tool for Material Processing," *Applied Optics*, **32**(6), pp. 885-893 (1993).

39 B. Singh, V. Patel, H.C. Sun and J. H. Thomas,III, "The Effect of RF Phase on the Plasma Density and Distribution for Electronegative Gases in a Triode Etching Reactor," Presented at the 39th *American Vacuum Society National Symposium,* Chicago, IL(November-1992).

40 V. Patel, H. C. Sun, B. Singh and B. Brycki, "A Parametric Study of Low Pressure Diode Reactor using Scanning Langmuir Probes" and "Effect of RF Phase on Discharge Characteristics in a Triode Reactor," To be submitted to the *Journal of Vacuum Science and Technology.*

41 V. Patel, H. C. Sun, B. Singh and B. Brycki, "Spatial Mapping of Plasma Density Distribution in Parallel-Plate Diode and Triode Etching Reactors," To be presented at *40th American Vacuum Society National Symposium,* Orlando, FL(November-1993).

42 A. Paranjpe, J. P. McVittie and S. Self, "A Tuned Langmuir Probe for Measurements in RF Glow Discharges," *J. Appl. Phys.*, **67**(11), pp. 6718-6727 (1990).

43 M. Meyyappan, "A Continuum Model for Low Pressure Radio Frequency Discharges," *J. Appl. Phys.*, **69**(12), pp. 8047-8051 (1991).

44 K. Kohler, D. Horne and J. Coburn, "Frequency Dependence of Ion Bombardment of Grounded Surfaces in RF Argon Glow Discharges in a Planer System," *J. Appl. Phys.*, **58**(9), pp. 3350-3355 (1985).

45 Bisschops T. J., Ph.D. Thesis, Eindhoven University of Technology, The Netherlands (1987).

46 R. Doyle, M. Hopkins and J. Scanlan, " Plasma Parameters in Low Pressure RF Plasmas," Presented at the *45th Gaseous Electronic Conference*, Boston, MA (Nov. 1992).

47 H. Sabadil, S. Klagge and M. Kammeyer, "Langmuir Probe Measurements of Axial Variation of Plasma Parameters in 27.1 MHz RF Oxygen Planar Discharges," *Plasma Chemistry and Plasma Processing*, **8**(4), pp. 425-444 (1988).

48 Ch. Steinbruchel, B. Curtis, H. Lehmann and R. Widmer, "Diagnostics of Low-Pressure Oxygen RF Plasmas and the Mechanism for Polymer Etching: A Comparison of Reactive Sputter Etching and Magnetron Sputter Etching," *IEEE Trans. Plasma Science*, **PS-14** (2), pp. 137-144 (1986).

49 M. Haverlag, A. Kono, D. Passchier, G. Koresen, W. J. Goedheer and F. J. de Hoog, "Measurements of Negative Ion Densities in 13.56 MHz RF Plasmas of CF_4, C_2F_6, CHF_3 and C_3F_8 using Microwave Resonance and the Photodetachment Effect," *J. Appl. Phys.*, **70**(7), pp. 3742-3780 (1991).

50 P. Blentzinger, "Experimental Characteristics of RF Parallel-Plate Discharges: Influence of Attaching Gases," *J. Appl. Phys.*, **67**(1), pp. 130-138 (1990).

51 A. Picard, G. Turban and B. Grolleau, "Plasma Diagnostics of a SF_6 RF Discharge used for the Etching of Silicon," *J. Phys. D: Appl. Phys.*, **19**, pp. 991-1005 (1986).

52 J. W. Coburn, *Plasma Etching and Reactive Ion Etching* (American Vacuum Society, New York, 1982), and references therein.

53 C. M. Melliar-Smith and C. J. Mogab in *Thin Film Processes*, ed. by J. L. Vossen and W. Kern (Academic Press, New York, 1979).

54 D. L. Flamm and G. K. Herb in *Plasma Etching*, ed. by D. M. Mannos and D. L. Flamm (Academic Press, San Diego, 1989).

55 J. Nulty (GS-DRYTEK), Private Communication.

56 S. J. Fonash, "Advances in Dry Etching Processes- A Review," *Solid State Technol.*, **29**(1), pp. 150-158 (1985).

57 F. F. Chen, *Introduction to Plasma Physics* (Plenum Press, New York, 1974).

58 B. Singh and P. R. Denton, "The Magnetron: Many Gains and More to Come," *Optical Spectra*, **15**(10), pp. 77-81(1981).

59 R. Waits, "Planar Magnetron Sputtering," *J. Vac. Sci. Technol.*, **15**(2), pp. 179-187 (1978).

60 J. Thornton, "Magnetron Sputtering: Basic Physics and Application to Cylindrical Magnetrons, *J. Vac. Sci. Technol.*, **15**(2), pp. 171- 177 (1978).

61 J. Vossen and W. Kerns, *Thin Film Processes* (Academic Press, NY, 1978).

62 H. Kinoshita, T. Ishida and S. Ohno, "Highly Uniform Magnetron Etching System Using an Annular Permanent Magnet, " *Appl. Phys. Lett.*, **50**(25), pp. 1838-1841 (1987).

63 H. Okano, T. Yamazaki and Y. Horiike "High Rate Reactive Ion Etching Using a Magnetron Discharge," *Solid State Technol.*, **25**(4), pp. 166-170 (1982).

64 S. Fang and J. McVittie, "A Model and Experiments for Thin Oxide Damage From Wafer Charging in Magnetron Plasmas," Semiconductor Research Corporation Technical Report No. C92325 (1992).

65 S. Fang and J. McVittie, "A Model for Thin Oxide Damage in Nonuniform Discharges: Magnetron Ashing," Semiconductor Research Corporation Technical Report No. C92505 (1992).

66 P. Laporte, Y. Melaku and M. Goethals, "Magnetically Confined Dry Etching for Silylated Resist Development," *Solid State Technol.*, **34**(4), pp. 69-73, (1991).

67 H. Kinoshita and O. Matsumoto, "A New Supermagnetron Plasma Etcher Remarkably Suited for High Performance Etching," *J. Vac. Sci. Technol. B*, **9**(2), pp. 325-333(1991).

68 J. M. Cook, D. Ibbotson, P. Foo and D. Flamm," Etching Results and Comparison of Low Pressure electron Cyclotron Resonance and Radio Frequency Discharge Sources," *J. Vac. Sci. Technol. A*, **8**(3), pp. 1820-1824 (1990).

69 B. Chapman, N. Benjamin, C. F. A. Vanos, R. Boswell and A. Perry, "Plasma Dry Processing in the Helicon Reactor," in *Proc. Symp. on Dry Processes*, Tokyo, pp. 39-42 (Oct.-1991).

70 A. Perry and R. Boswell, "Fast Anisotropic Etching of Silicon in an Inductively Coupled Plasma Reactor," *Appl. Phys. Lett.*, **55**(2), pp. 148-150 (1989).

71 B. Singh, J. H. Thomas,III and V. Patel, "Magnetic Multipole Based Reactive Ion Etching Reactor," *Appl. Phys. Lett.*, **60**(19), pp. 2335-2337 (1992).

72 A. P. H. Goede, T. S. Green and B. Singh, "Measurement of Electron Energy Distribution in a Magnetic Multipole Ion Source," *J. App. Phys.*, **51**, pp. 1896-1899 (1980).

73 B. Singh, Ph.D. Thesis, "Investigation of Some of the Physical Processes Occurring in High Current Ion Sources," University of Aston, Birmingham, UK(1978).

74 K. Leung, N. Hershkowitz and K. McKenzie, "Plasma Confinement by Localized Cusps," *Phys. Fluids*, **19**, pp. 1045-1051 (1976).

75 M. Jenkins, M. Mocella, K. Allen and H. Sawin, "The Modeling of Plasma Etching Processes Using Response Surface Methodology," *Solid State Technol.*, **29**(4), pp. 175-182 (1986).

76 V. Patel, H. C. Sun, B. Singh and B. Brycki, "Polysilicon Etching in Magnetic-Multipole Enhanced Triode Reactor," To be submitted to the *Journal of Vacuum Science and Technology.*

77 V. Patel, W. F. Kosonocky, B. Singh, H. C. Sun and N. McCaffrey, "End Point Monitoring of Patterned Wafers During Reactive Ion Etching using a High Resolution Infrared Camera," Presented at the 39th *American Vacuum Society National Symposium,* Chicago, IL(November-1992).

78 V. Patel, M. Patel, S. Ayyagari, D. Misra, W.F. Kosonocky and B. Singh, "Wafer Temperature Measurements and End-point Detection During plasma Etching by Thermal Imaging," *Appl. Phys. Lett.*, **59**(11), pp. 1299-1301(1991).

79 V. Patel, W.F. Kosonocky, S. Ayyagari, M. Patel and B. Singh, "Application of Thermal Imaging Methodology for Plasma Etching Diagnosis," *Proceedings of SPIE's Technical Symposium on Process Module Metrology, Control and Clustering*, **1594,** pp. 204-208 (1991).

80 M. Kaplinsky, "Application of Imaging Pyrometry for Remote Temperature Measurements," MS Thesis, NJIT (1992).

81 Khan M. A., C. Allemad and T. Eagar, "Non-contact Temperature Measurement: Interpolation Based Techniques," *Rev. Sci. Instrum.*, **62**, pp. 393-403 (1991) and Khan M. A., C. Allemad and T. Eagar, "Non-contact Temperature Measurement: Least Squares Based Techniques," *Rev. Sci. Instrum.*, **62** , pp. 403-409 (1991).

82 T. Villani, W. Kosonocky, F. Shallcross, J. Groppe, G. Meray, J. O'Neill, and B. Esposito, " Construction and Performance of a 320X244-Element IR-CCD Imager With PtSi SBDs," Proc. *SPIE,* **1107,** pp. 249-256 (1989).

83 H. Busta, R. E. Lajos and D. Kiewit, "Plasma Etch Monitoring With Laser Interferometry," *Solid State Technol.*, **22**(2),pp. 62-65 (1979).

84 M. Sternheim, W van Gelder and A. Hartman, "A laser Interferometer System to Monitor Dry Etching of Patterned Silicon," *J. Electrochem. Soc.: Solid-State Science and Technology*, **130**(3), pp. 655-658 (1983).

85 G. Bunyard and B. Raby, "Plasma Process Development and Monitoring via Mass Spectrometry," *Solid State Technol.*, **20**(12), pp. 53-57 (1977).

86 W. Harshbarger, R. porter, T. Miller and P. Nortan, "A Study of the Optical Emission from an RF Plasma During Semiconductor Etching," *Applied Spectroscopy*, **31**(3), pp. 201-205 (1977).

87 S. Henck, "In Process Thin Film Thickness Measurement and Control," Proceedings of the *SPIE Symposium on Process Module Metrology, Control and Clustering* , **1594,** pp. 216-221(1991).

88 K. Ukai and K. Hanazawa, "End-point Determination of Aluminum Reactive Ion Etching by Discharge Impedance Monitoring," *J. Vac. Sci. Technol.*, **16**(2), pp. 385-387 (1979).

89 H.C. Sun, V. Patel, E. Whittaker and B. Singh (unpublished results).

90 D. Economou, E. Aydil and G. Barna, "*In Situ* Monitoring of Etching Uniformity in Plasma Reactors," *Solid State Technol.*, **34**(4), pp. 107-111 (1991).

91 H. McMahon, "Thermal radiation from Partially Transparent Bodies," *Journal of Optical Society of America*, **40**, 376 (1950).

92 R. E. Gorden, "The Emissivity of Transparent Materials," *J. Am. Ceram. Soc.*, **39**(8), pp. 278-287 (1956).

93 H. A. Macleod, *Thin-Film Optical Filters* (McGraw-Hill Publishing Co., New York, NY, 1989).

94 J. Lavine, F. Lo, F. Moser, B. Burkey and F. Smith, "The Determination of Doped Polysilicon Carrier Concentration by Infrared Spectrophotometry," *Proceedings of the Symposia on Electronic and Optical Properties of Polycrystalline or Impure Semiconductors and Novel Silicon Growth Methods*, Edited by K. V. Ravi and B. O'Mora, The Electrochemical Soc., Inc., pp. 96-105(1980).

95 P. Hesketh, J. Zemel and B. Gebhart, "Polarized Spectral Emittance From Micromachined Surfaces; I-Doped Silicon: The Normal Direction," *Physical Review B*, **37**(18), pp. 10795-10802 (1988) and P. Hesketh, J. Zemel and B. Gebhart, "Polarized Spectral Emittance From Micromachined Surfaces; II-Doped Silicon: Angular Variation," *Physical Review B*, **37**(18), pp. 10803-10813(1988).

96 A. Borghesi, A. Piaggi, G. Guizzetti, F. Levy, M. Tanaka and H. Fukutani, "Optical Properties of Single-Crystal Titanium Disilicide," *Physical Review B*, **40**(3), pp. 1161-1168 (1989).

97 A. Borghsi, L. Nosenzo, A. Piaggi, G. Guizzetti, C Nobili, and G. Ottaviani, "Optical Properties of Tantalum Disilicide Films," *Physical Review B*, **38** (15), pp 10937-10940(1988).

98 D. P. DeWitt and J. C. Richmond in *Theory and Practice of Radiation Thermometry*, Edited by D. P. DeWitt and G. Nutter, Chapter 2, pp. 107-121, (John Wiley & Sons, Inc. , New York, 1989).

99 Y. Liu and M. Flowers, "Kinetics of Triode Mode Reactive ion Etching of Si(100) Wafers by Chlorine Plasmas: Temperature and DC Self-bias Effects," *Vacuum*, **42**(18), pp. 1213-1217 (1991).

100 S. Tachi, K. Tsujimoto, S. Arai and T. Kure, "Low-Temperature Dry Etching," *J. Vac. Sci. Technol. A*, **9**(3), pp. 796-803).

101 A. Watts and W. Varhue, "Low Temperature Etching of Silicon Trenches With SF_6 in an Electron Cyclotron Resonance Reactor," *J. Vac. Sci. Technol. A*, **10**(4), pp. 1313-1330(1992).

102 G. Luckman, "Measurement of Wafer Temperature Variations Using Photoresist Reticulation Thresholds," *J. Vac. Sci. Technol. B*, **11**(1), pp 99-107(1993).

103 D. Vogal and F. Wong, "Measurement and Control of Wafer Temperature in a Plasma Etching Reactor," Presented at the *SPIE Symposium on Microlithography*, Santa Carla, CA, March 1-6 (1987).

104 R. Conotolini and L. D'Asaro, "High Rate Masked Etching of GaAs by Magnetron Ion Etching," *J. Vac. Sci. Technol B*, **4**(3), pp. 706-713 (1986).

105 V. Donnelly and J. McCaully, "Infrared Laser Interferometric Thermometry: A Non-intrusive Technique for Measuring Semiconductor Wafer Temperatures," *J. Vac. Sci. Technol A*, **8**(1),pp. 84-92 (1990).

106 S. Zaidi, S. Brueck and J. McNeil, "Non-contact, 1°C Resolution Temperature by Projection Moiré Interferometry," *J. Vac. Sci. Technol B*, **10**(1), pp. 166-169(1992).

107 A. Mitchell and R. Gottscho, "Plasma Power Dissipation at Wafer Surfaces Measured Using Pulsed Photoluminescence Spectroscopy," *J. Vac. Sci. Technol A*, **8**(3),pp. 1712-1715 (1990).

108 R. Carlile, V. Liang and M. Smadi, "High Quality Trench Etches in Silicon," *Solid State Technol.*, **32**(4), pp. 119-123 (1989).

109 D. Wright, D. Hartman, U. Sridharan, M. Kent, T. Jasinski and S. Kang, "Low Temperature Etch Chuck: Modeling and Experimental Results of Heat Transfer and Wafer Temperature," *J. Vac. Sci. Technol. A*, **10**(4), pp. 1065-1070 (1992).

110 V. Patel, M. Kaplinsky, W. F. Kosonocky, S. Ayyagari and B. Singh, "Heat Transfer Analysis of Silicon Wafers During Reactive Ion Etching," *39th American Vacuum Society National Symposium,* Chicago, IL(November-1992).

111 R. Visser, "Determination of the Power and Current Densities in Argon and Oxygen Plasmas by *In Situ* Temperature Measurements," *J. Vac. Sci. Technol. A*, *7*(2), pp.-189-205 (1989).

112 W. G. Bear, T. Hull, K. D. wise, K. Najafi and K. D. Wise, "A Multiplexed Silicon Infrared Thermal Imager," *Digest Int. Conf. on Solid-State Sensors and Actuators,* San Francisco, pp. 2-7, June 1991.

113 I. Langmuir and H. Mott-Smith, *Collected Works of Irving Langmuir,* Vol. 4, pp 99-132 (Pergamon Press, Long Island City, NY, 1961)

114 P. Chung, L. Talbot and K. Touryan" Electrical Probes in Stationary and Flowing Plasma: Part 1, Collisional and Transitional Probes; Part 2, Continuum Probes," *AIAA Journal, 12*(2),pp 133-154(1974)

115 B. E. Cherrington, "The Use of Electrostatic Probes for Plasma Diagnostics-A Review," *Plasma chemistry and Plasma Processing*, **2**(2), pp. 113-140(1982) and references therein.

116 J. G. Laframboise, Univ. of Toronto Inst. Aerospace Studies Report No. 100 (1966).

117 Ch· Stienbruchel, "Langmuir Probe Measurements on CHF_3 and CF_4 Plasmas: The Role of Ions in Reactive Sputter Etching of SiO_2 and Si," *J. Electrochem. Soc: Solid-State Science and Technol.*, **130**(3), pp. 648-655 (1983).

118 H. Amemiya, "Plasmas With Negative Ions-Probe Measurements and Charge Equilibruim," *J. Phys. D: Appl. Phys.*, **23**, pp. 999-1014 (1990).

119 J. D. Swift and M. Schwar, *Electrical Probes for Plasma Diagnostics*, (Elsevier, New York, 1971).

120 D. Maundrill, J. Slatter, A. Spiers and C. Welch, "Electrical Measurements of RF Generated Plasmas Using a Driven Electrostatic Probe Technique," *J. Phys. D: Appl. Phys.*, **20**, pp 815-819 (1987).

121 G. Fortunato, "End-point Determination by Reflected Power Monitoring," *J. Phys. E: Sci. Instrum.*, **20**, pp. 1051-1053 (1987).

122 A. Tretola, "Impedance Mismatch End-Point Detection Method for Plasma Etching" *Proceedings of the Symposium on Plasma Etching and Deposition*, The Electrochemical Society Proceedings, **81-1**, pp. 295-299 (1981).

123 S. E. Savas, D. E. Horn and R. Sadowski, "Dummy Load Technique for Power Estimation in RF Efficiency Discharges," *Rev. Sci. Instrum.*, **57**(7), pp. 1248-1253 (1986).

124 J. W. Butterbaugh, L. D. Baston and H. H. Sawin, "Measurement and Analysis of Radio Frequency Glow Discharge Electrical Impedance and Network Power Loss," *J. Vac. Sci. Technol.* A, **8** (2), pp. 916-923 (1990).

125 H. S. Carslaw and J. C. Jaeger, *Conduction of Heat in Solids*, Ch. 3 (Oxford University Press, Oxford, UK, 1986).